Coherent Heteronuclear Spin Dynamics in an Ultracold Spinor Mixture
超冷旋量混合物中的異核間相干自旋動力學

LI, Xiaoke
李小科

A Thesis Submitted in Partial Fulfilment
of the Requirements for the Degree of
Doctor of Philosophy
in
Physics

The Chinese University of Hong Kong
August 2015

Thesis Assessment Committee

Professor LIU, Renbao (Chair)
Professor WANG, Dajun (Thesis Supervisor)
Professor LAW, Chi Kwong (Committee Member)
Professor CHEN, Shuai (External Examiner)

Abstract

After more than 30 years development, ultracold atoms have become a versatile platform with a wide range of applications, from studying very fundamental physics such as basic properties of BEC, to making practical devices such as atomic clock. Among these applications, the spinor quantum gas, a quantum gas with spin degree of freedom, has attracted a lot of attentions, both experimentally and theoretically. Whereas all previous studies focus on spinor gases of single atomic species, in this thesis we present the first experimental studies of coherent spin-mixing dynamics in a spinor mixture of ^{87}Rb and ^{23}Na.

We produce an ultracold mixture of ^{87}Rb and ^{23}Na atoms with laser cooling and evaporative cooling in magnetic and optical traps. A special spin state is prepared such that each species is in a superposition of the Zeeman sublevels in their $F = 1$ hyperfine ground-state manifolds. Interspecies spin-changing collisions cause the oscillation between the spin populations. We observe that the magnetization of each species oscillates while the total magnetization is conserved. We also study the effect of external magnetic field and find a resonance behavior of the dynamics. Furthermore, this resonance is found to be controllable by changing the polarization of the optical trapping light, due to the small vector light shift. The observed phenomena are in good agreement with theory developed based on the mean field Gross-Pitaevskii equation for condensate and Boltzmann equation for thermal gas.

We also study the thermal Rb spinor gas with spin either $F = 1$ and $F = 2$. Although there are differences between BEC and thermal gas in essence, the observed long-lasting coherent dynamics shows that they can be treated by unified formalism. The prediction of a factor of two in the interaction term is verified by measuring the dynamics at different atomic density.

摘要

經過三十多年的發展，超冷原子已經成為一個研究前沿物理的多用平臺，其應用包括基礎物理研究如玻色－愛因斯坦凝聚的基本性質，到研製實用的設備如原子鐘。在這些研究之中，具有內稟自由度的量子氣體（被稱之為旋量氣體）受到實驗和理論上的廣泛關注。已有的實驗研究均集中在單種原子的旋量氣體，而本論文闡述了在此領域中對 ^{87}Rb 和 ^{23}Na 旋量氣體混合物中的自選相干混合動力學的首次實驗研究。

我們在磁阱和光阱中利用激光冷卻和蒸發冷卻的方法製備出 ^{87}Rb 和 ^{23}Na 的超冷混合物，並製備一特殊的自旋初態，使每種原子都處於其超 $F = 1$ 精細基態中各塞曼子能級的疊加態。我們觀察到異核間的自旋交換碰撞引起自旋態上原子數分佈隨時間的週期性變化，而每種原子的相對磁化強度亦隨時間作週期變化，但系統的總相對磁化強度守恆。我們研究了外加磁場的影響並發現了共振現象，並且由於向量光能移的原因，此共振的位置能用囚禁光的偏振態來調控。我們觀察到的現象與用 Gross-Pitaevski 方程和 Boltzmann 方程建立起來的理論模型結果一致。

我們也研究了自旋為 1 和 2 的 ^{87}Rb 熱原子旋量氣體。儘管凝聚體和熱原子的旋量氣體有很大區別，但我們觀察到持續了長時間的相干動力學表明它們可以遵守同樣形式的運動方程，並且亦以實驗證實其不同之處為自旋相互作用數值上相差兩倍。

ACKNOWLEDGMENTS

At the end of the four years doing research on cold atoms in the Chinese University of Hong Kong, I feel grateful to many people I have met and worked with. First of all, I would like to express my deepest thanks to my supervisor Prof. Dajun Wang for giving me the chance to work here and guiding me into the field of cold atoms. His enthusiasm to science, rich experience in experimental physics, and intuition in solving problems make us grow and keep our group energetic. I want to thank Prof. Chi Kwong Law, Prof. Ren Bao Liu, Prof. Qi Zhou and Prof. Quan Li for teaching me the excellent physics courses, and I learn a lot from their insights to physics. I would also like to thank Prof. Ming Chung Chu for his endless friendly care. I am happy to have chance to work with all the members in our group: Fudong Wang is an always reliable friend and colleague who has the ability to keep things going well. Bing Zhu has wide interests and open eyes in physics, and I must thank him for his realizing the effect of vector light shift in the spinor mixture experiment which solves the puzzles in early days. Jun Chen works hard and is always ready to help others. Mingyang Guo is diligent and persevere in solving problems. Xin Ye is energetic and willing to learn everything. I benefit a great deal from them during the past years. I appreciate the great helps from postdoc Bo Lu both in academics and in life, and he is always friendly and patient in answering all my questions. Our former postdocs Xiaodong He and Dezhi Xiong taught me much knowledge and I greatly appreciate working with them. Thank Prof. Shizhong Zhang and Prof. Zhifang Xu for the collaborations on the work described in this thesis and many beneficial discussions. I also want to thank Shihong Liao and Naijing Deng for discussing physics and dealing with all affairs in life. I express my appreciation to the administrative staff of physics department and the technical staff who provide much help to my research. Finally, I cannot express myself in words how thankful I am to my parents, sisters and brother, who give me warm and strong support at all times.

Contents

List of Figures

Chapter 1

Introduction

Twenty years ago in 1995, the first Bose-Einstein condensation (BEC) were observed experimentally in ^{87}Rb and ^{23}Na atomic gases [1–3], which makes Einstein's prediction [4] in 1925 come true and marks the beginning of a new and continuously growing research field of ultracold quantum gases. The success owes largely to the development of cooling and trapping techniques of neutral atoms. When the spin degree of freedom is liberated in optical trap, the resulting spinor gases exhibit even richer properties. In this chapter, we give a brief introduction to the developments and achievements in this young and fascinating field.

1.1 From laser cooling and trapping to Bose-Einstein condensation

The theoretical prediction of BEC was made by Einstein in 1925 who generalize the statistics of photons, put forward by Bose [5], to noninteractive massive bosons, and found that below a critical temperature, a macroscopic fraction of the particles will occupy the lowest energy state [4]. It was realized by Fritz London that superfluid ^{4}He would be a kind of BEC in 1938 [6]. However, the strong interaction between He atoms conceal many key properties of BEC, since the condensate fraction can only reach 10% [7]. Thus it is desired to find an "ideal" system which remain gaseous at temperature as low as the transition temperature so that the interaction is weak. It was proposed by Hecht in 1959 that spin-polarized Hydrogen is such an weakly interacting Bose gas [8], and confirmed by Stwalley [9] in 1976 through detailed study of the interaction between H atoms. Their work motivated the search of BEC in dilute atomic gases.

Another candidate is the alkaline atomic gases, which become attractive due to the success of laser cooling and trapping. The idea of trapping neutral atoms by light dates back to Askar'yan, Letokhov [10] and Ashkin [11], but the great breakthroughs in experiment were made by Chu, who realized the first optical dipole trap in 1986 [12] and magneto-optical trap in 1987 [13]. With later progresses both in experiment and theory [14], alkaline atoms can be trapped and laser cooled from room temperature to microKelvin regime and laser cooling is still the starting stage of all experiments studying ultracold gases today. Combined with magnetic traps proposed by Pritchard [15], the first BECs were achieved by evaporative cooling in 1995 by the MIT group and JILA group, in atomic species of ^{23}Na and ^{87}Rb respectively.

The birth of BEC attracted great interests and extensive studies in the atomic, molecular and optical (AMO) physics and condensed matter physics societies. On the one hand, a BEC can be viewed as a coherent matter wave, whose coherent properties are widely investigated in new research fields such as atom optics, and exploited in many high precision measurements. On the other hand, the BEC as well as ultracold thermal gas provides an isolated, clean and tunable system to study fundamental physics. Traditional "difficult" problems such as superconductivity can also be investigated, especially combined with optical lattice which may enable quantum simulation.

A great advantage of BEC in atomic gases is that it is well described by a wavefunction governed by the Gross-Pitaevski equation (GPE) in the mean-field level, which is studied theoretically by Gross [16, 17] and Pitaevski [18] in 1960s in order to describe vortices in superfluid. GPE has been found highly successful in explaining a series of properties of atomic BEC, such as the density profile in trap [19], elementary excitations [20–23], solitons [24, 25], vortices [26–30] and multicomponent BECs [31, 32]. Today, many topics and new results are still being investigated under the guidance of GPE [33]. Meanwhile, under some conditions, the atomic BEC can go beyond the mean field theory in which cases quantum fluctuations or the interaction between condensate and thermal component must be taken into account, hence it also provides a tool to test the many-body theory.

1.2 Spinor Gases

Among many research directions utilizing ultracold atoms, spinor gas draw much attention as it appears as a new quantum fluid that exhibits both superfluid and magnetic properties. The subject originated from 1998, when the BEC of ^{23}Na [34] was successfully produced in optical traps. In contrast with magnetic trap in which only special spin states can be trapped, the optical dipole trap (ODT) potential can be spin-independent hence the spin degree of freedom is liberated. The interaction becomes spin-dependent. Ho [35], Ohmi and Machida [36] first considered the problem and studied the interaction in the spin-exchange form. The ground state and elementary excitations are calculated and it is predicted that the $F = 1$ ^{87}Rb BEC has a ferromagnetic ground state while that for ^{23}Na is polar, which are confirmed in later experiments.

Triggered by the pioneering theoretical and experimental work in 1998 [37–39], a lot of intriguing properties of the spinor gases related to the spinor wavefunction and spin-dependent interaction are proposed and studied. A first important problem is the identification and classification of the various ground state phases in $F = 1$, 2 and 3 spinor BEC. The phase transition between some of them are observed. Like the case in magnetic materials, spin domain can form inside the spinor BEC after holding in the trap [34] or through a rapid quench of the magnetic field [40]. In contrast to scalar BEC where only mass current exists when the condensate phase has spatial variation, in spinor BEC both mass current and spin current, which is called spin textures, can be produced due to spatial variation of spin. They include a variety of topological excitations such as monopoles [41, 42], skyrmions [43, 44], vortices [45, 46], and knots [47].

In virtue of the detecting technique for spinor gases, which include the absorption imaging after Stern-Gerlach separation during time-of-flight, and the non-destructive magnetization imaging [48], nonequilibrium dynamics can be examined in spinor gases by preparing the system far from equilibrium and probing the spin evolution. An important and early studied one is the spin mixing dynamics, in which the spin exchange interaction lead to the spin-mixing processs, and the population of each spin state shows macroscopic oscillations. It also accounts for the formation of spin domains and spin textures. The spin-mixing dynamics between two atomic species and in a non-condensed cloud are the subjects of this thesis. A brief review of the development is given in Sec. 5.1. Besides spin-mixing dynamics, currently interesting topics include spin squeezing [49, 50], parametric amplification [51, 52], quench dynamics [40], relaxation and thermalization [53], and dynamics caused by dipolar interaction [54].

In the theoretical aspect, the spinor gases provide a two-body interaction which is more complicated than the simplest scaler contact interaction. The difference from the traditional quantum fluid with internal degree of freedom such as superfluid ^{3}He, p-wave and d-wave superconductor and neutron star is that the system parameters are highly controllable. Hence the consequence of the interaction is ready to be examined experimentally, and the clear microscopic picture make a direct comparison between several theoretical models and experiments possible. Currently the mean-field GPE is often used to describe the spin mixing dynamics, while other theories such as Bogoliubov theory [55], Beliaev theory [56] and exact many-body theory [57] for spin degree of freedom are investigated, but the experimental observation of the different effects are still underway.

1.3 Thesis Outline

This thesis describes the experimental investigation of the heteronuclear spin-mixing dynamics between spin-1 ^{87}Rb and ^{23}Na spinor gases [58], and dynamics in thermal gases of spin-1 and spin-2 ^{87}Rb [59], as well as the necessary theoretical background and experimental setups. We have given an overview of the research field of cold atom and spinor gases in this chapter.

In chapter 2, the basic knowledge of light-atom interaction and its application in cooling and trapping neutral atoms, and the effects of magnetic field are described, which are crucial in designing the atom traps. The principles of cooling and trapping are reviewed and a brief introduction of BEC and GPE is given.

In chapter 3 we try to give a theoretical background which treat the spinor gases from the first principle and derive the experimental observable quantities. The main result for the ground state and dynamics of spin-1 BEC are presented. We also discuss the mean-field approximation and single-mode approximation, as well as some behavior beyond these approximations. The theory for spinor mixutre is presented.

In chapter 4 we come to the experimental part, and all components in the apparatus carrying out the experiment are described in detail. We also explain how to probe and characterize the atomic cloud in the setup. Previous results including producing the two species ultracold mixture and BEC, studying Feshbach resoances and creating Feshbach molecules are summarized.

In chapter 5 we describe the experiment on the spin-mixing dynamics between ^{87}Rb and ^{23}Na in detail. We specify the state preparation, the experimental sequences and the observations of the dynamics as well as the control of resonance by tuning the polarization of light. Necessary calculation and illustration to understand the experiment are given.

In chapter 6 the experiment on spin-mixing dynamics in thermal ^{87}Rb is present, both in $F = 1$ and $F = 2$ cases. We detail the description for non-condensed gas and compare the dynamics between BEC and thermal gas.

Finally we give a summary in chapter 7.

Chapter 2

Theoretical Background: Trapping and Cooling Atoms

2.1 Atom-light Interaction and Mechanical Effect

Atom-light interaction is a fundamental topic in atomic physics and quantum optics. It is the starting point for investigating and manipulating many of the properties of atomic gases. In experiments trapping and cooling atoms and the studies of quantum gases, the topic arises in many scenes. For example, in magneto-optical trap, atoms undergo cycling transition in the presence of red-detuned near resonant light; optical dipole trap utilizes AC stark effect of light on atoms to generate dipole force; even microwave driving the transitions between hyperfine levels can be viewed as a kind of light-atom interaction. Thus understanding how light interacts with atoms has long been an important and interesting problem.

The topic can date back to Lorentz 100 years ago, who considered the atom to be an harmonic oscillator and the light act as an AC electric field driving the oscillator. The model successfully describes a variety of phenomena such as index of refraction, the conductivity of metal even the normal Zeeman effect. It is still useful in deriving practical formula in laser cooling and trapping. However, we will start from the two-level system in semiclassical description, where two quantum states and classical field is considered.

The general form of the Hamiltonian of a two-level system in matrix form is

$$H = \hbar \begin{pmatrix} -\Delta & \Omega/2 \\ \Omega/2 & 0 \end{pmatrix}, \tag{2.1}$$

where the energy of the ground state and excited state without coupling is 0 and $-\Delta$, the Rabi frequency Ω represent the coupling strength. The form applies to many systems, for example, a two-level atom interacting with the monochromatic light under rotating-wave approximation in the rotating frame, a spin interacting with AC magnetic field and even two interacting spins constituting effective two level system. In the first case, $\Delta = \omega - \omega_0$ is the detuning of light frequency relative to atomic transition frequency, and $\Omega = \langle g| e\mathbf{r} |e\rangle \cdot \mathbf{E}/\hbar$ for oscillating electric field $\mathbf{E}\cos\omega t$. The detuning and coupling can have different meanings in different systems, but the behaviour is similar. Since the the eigenenergies can be easily calculated

$$E_{\pm} = -\frac{\hbar\Delta}{2} \pm \frac{\hbar\tilde{\Omega}}{2}, \tag{2.2}$$

corresponding to eigenstates

$$\begin{aligned} |+\rangle &= \sin\theta\,|g\rangle + \cos\theta\,|e\rangle\,, \\ |-\rangle &= \cos\theta\,|g\rangle - \sin\theta\,|e\rangle\,, \end{aligned} \tag{2.3}$$

where

$$\tan 2\theta = -\frac{\Omega}{\Delta}\left(0 \le \theta \le \frac{\pi}{2}\right). \tag{2.4}$$

Therefore a general state at time t evolves according to

$$|\psi(t)\rangle = \langle + \mid \psi(0)\rangle \,|+\rangle\, e^{-iE_+t/\hbar} + \langle - \mid \psi(0)\rangle \,|-\rangle\, e^{-iE_-t/\hbar}. \tag{2.5}$$

A common situation is that the atom is initially prepared in the ground state and the resonant coupling is turned on at $t = 0$, i.e., $|\psi(0)\rangle = |g\rangle = (|+\rangle + |-\rangle)/\sqrt{2}$, and the state at time t is given by

$$|\psi(t)\rangle = \frac{1}{\sqrt{2}}\left(|+\rangle\, e^{-i\Omega t/2} + |-\rangle\, e^{i\Omega t/2}\right). \tag{2.6}$$

At the special time $\Omega t = \pi$,

$$|\psi(t = 2\pi/\Omega)\rangle = \frac{e^{-i\pi/2}}{\sqrt{2}}\left(|+\rangle + |-\rangle\, e^{i\pi}\right) = e^{-i\pi/2}\,|e\rangle\,, \tag{2.7}$$

and at time $\Omega t = 2\pi$,

$$|\psi(t = \pi/\Omega)\rangle = \frac{e^{-i\pi}}{\sqrt{2}}\left(|+\rangle + |-\rangle\, e^{i2\pi}\right) = e^{-i\pi}\,|g\rangle\,. \tag{2.8}$$

The two pulses transfer the total population to the excited state and back to ground state again. We can calculate the population in the excited state at time t is given by

$$\rho_e = |\langle e \mid \psi(t)\rangle|^2 = \sin^2\left(\frac{\Omega t}{2}\right). \tag{2.9}$$

From this expression we can see that the population of both state oscillates sinusoidally, which is referred to as Rabi oscillation. At $t = \pi/2\Omega, \pi/\Omega, 2\pi/\Omega$, the population of excited state is $\rho_e = 1, 0.5, 0$, and they are called $\pi/2$-pulse, π-pulse and 2π-pulse, respectively.

In the presence of detuning δ, one can find that the population in excited state becomes

$$\rho_e = \frac{\Omega^2}{\tilde{\Omega}^2}\sin^2\left(\frac{\tilde{\Omega} t}{2}\right), \tag{2.10}$$

where

$$\tilde{\Omega} = \sqrt{\Omega^2 + \Delta^2}. \tag{2.11}$$

These results are particulary useful in spin state preparation by microwave and RF pulses. By irradiating the pulse for a certain time and intensity, the population of the atoms can be transferred to the desired states. Another method for transferring the population is adiabatic rapid passage (ARP). From Eq. 2.3 and 2.4 we can see that the eigenstates in the presence of coupling is neither $|g\rangle$ nor $|e\rangle$ but $|+\rangle$ and $|-\rangle$, however, $|-\rangle$ is asymptotically equal to $|g\rangle$ when $\Delta \lll -\Omega$, and asymptotically equal to $|e\rangle$ when $\Delta \ggg \Omega$, and the eigenenergies has an avoided crossing in the transition between these two extreme cases. According to the adiabatic principle of quantum mechanics, the system remains in the instantaneous eigenstate if the Hamiltonian changes in time slowly enough. Hence the state will change from initial $|g\rangle$ to $|e\rangle$ if we turn on the coupling at time $t = 0$ with $\Delta \lll -\Omega$ and adiabatically vary it to $\Delta \ggg \Omega$ then turn off. In fact, for imperfect adiabatic passage, the fraction that remains in the ground state due to finite changing rate of Δ is given by [60]

$$P = \exp\left(-\frac{\pi\Omega^2}{2\left|d\Delta/dt\right|}\right). \tag{2.12}$$

The above two methods for preparing initial spin states are widely used in our experiments searching for the Feshbach resonances and spinor dynamics.

Mechanical Effects

In the discussion above we only consider the internal states of an atom. However atoms always have motional degree of freedom in real space, and the interaction of light and atom manifests as potentials or forces exerted on the atoms. There are two kinds of forces: dipole force originated from the gradient of field amplitude and radiation-pressure force due to absorption of photons. Though they can be treated in a uniform framwork [61], it is instructive to discuss them separately from different approaches.

Dipole force - From the eigenenergies 2.2 the energy of the atoms is shifted by the light, which is the well-studied AC stark effect. For far and red detuned light ($\Delta \ll -\Omega < 0$), most of the atoms are in the ground state and the energy shift is given by

$$U = -\frac{\hbar\Delta}{2} - \frac{\hbar\tilde{\Omega}}{2} = -\frac{\hbar\Delta}{2} + \frac{\hbar\Delta}{2}\sqrt{1 + \frac{|\Omega|^2}{\Delta^2}} \approx \frac{\hbar|\Omega|^2}{4\Delta}. \tag{2.13}$$

If the light field amplitude has spatial dependence so that the Rabi frequency is $\Omega(\mathbf{r})$, the force is proportional to the gradient of the potential

$$F(\mathbf{r}) = -\nabla U(\mathbf{r}). \tag{2.14}$$

The dipole force is utilized in far-off-resonant trap or ODT. The trapping potential is proportional to the intensity of the light hence an usual Gaussian beam provide a 3D trap which potential minimum is at the beam waist position. For a real atom with multi energy levels, the Rabi frequencies are related to the natural linewidth of the transitions, and a practical calculation of the trapping potential are given in Sec. 2.2.

Radiation-pressure force - Though can be explained in terms of momentum carried by electromagnetic waves, the radiation-pressure force is more lucid in view of photons suffering absorption and emission by atoms. Both events change the energy and momentum of the atom due to conservation laws, and the force can be calculated from the time average of these events which usually has large number in a short time. In the above discussion we do not consider the spontaneous decay of the atom in the excited state, which can be ignored only in microwave and RF problems. This is well-explained by assuming additional terms accounting for spontaneous decay in the optical Bloch equations in terms of density matrices

$$\begin{aligned}
\dot{\rho}_{gg} &= \frac{i\Omega}{2}\left(\rho_{ge} - \rho_{eg}\right) + \Gamma\rho_{ee} \\
\dot{\rho}_{ee} &= -\frac{i\Omega}{2}\left(\rho_{ge} - \rho_{eg}\right) - \Gamma\rho_{ee} \\
\dot{\rho}_{ge} &= -\left(\frac{\Gamma}{2} + i\Delta\right)\rho_{ge} - \frac{i\Omega}{2}\left(\rho_{ee} - \rho_{gg}\right)
\end{aligned} \quad , \tag{2.15}$$

where ρ_{ij} is the matrix elements of the density operator $\rho = |\psi\rangle\langle\psi|$, Γ is the natural decay rate of the excited state which is the reciprocal of the lifetime τ. The steady state solution of the excited state population is found to be

$$\rho_{ee}\left(t \to \infty\right) = \frac{(\Omega/\Gamma)^2}{1 + 4(\Delta/\Gamma)^2 + 2(\Omega/\Gamma)^2}. \tag{2.16}$$

In view of photons, the number of photons scattered by an atom in unit time is given by

$$\begin{aligned}
R &= \Gamma\rho_{ee}\left(t \to \infty\right) \\
&= \Gamma\frac{(\Omega/\Gamma)^2}{1 + 4(\Delta/\Gamma)^2 + 2(\Omega/\Gamma)^2} \\
&= \frac{\Gamma}{2}\frac{I/I_s}{1 + 4(\Delta/\Gamma)^2 + I/I_s},
\end{aligned} \tag{2.17}$$

where the saturated intensity is defined such that $I/I_s = 2(\Omega/\Gamma)^2$.

In this view an atom stimulatedly absorbs and spontaneously emits $R\Delta t$ photons in a short time Δt, during which the absorbed photons are all come from one direction while the emitted photons go out in all directions. The net momentum obtained by the atom is therefore $p_r R\Delta t$, where $p_r = \hbar k$ is the recoil momentum obtained by the atom in a single event. The average force is therefore

$$F_{\text{rad}} = \frac{p_r R\Delta t}{\Delta t} = \hbar k\frac{\Gamma}{2}\frac{I/I_s}{1 + 4(\Delta/\Gamma)^2 + I/I_s}. \tag{2.18}$$

The radiation force plays the major role in laser cooling and trapping. The idea for cooling (hence slowing the motion of an atom) is straightforward: consider an atom placed inside two counterpropagating red detuned laser beams with the same frequencies, if the atom has a velocity to the right, then the laser beam pointing to the left gives a larger force due to smaller Δ in Eq. 2.18 caused by Doppler effect, while the laser beam pointing to the right gives a smaller force. Hence an atom moving to the right experience a net force pointing to the left, and vice versa. Furthermore, the larger velocity corresponds to larger force, hence the atoms are slow down until the forces are balanced. This is the basic principle of the so-called optical molasses and can be viewed as the trapping of atoms in momentum space. By combining with magnetic gradient fields, a spatial dependent restoring force can be generated. The working principle of magneto-optical trap is described in Sec. 2.2.3.

2.2 Atom Traps

2.2.1 Zeeman Effect and Magnetic Trap

Magnetic trapping of neutral atoms makes use of Zeeman effect. In the absence of external magnetic field, the angular momentum state of an atom is described by the Hamiltonian with the hyperfine interaction

$$H_{hf} = A\mathbf{I} \cdot \mathbf{J} \tag{2.19}$$

where A is the hyperfine splitting constant, $\mathbf{I}$ is the nuclear angular momentum and $\mathbf{J}$ is the electronic total angular momentum. The eigenstates are those of the total angular momentum $\mathbf{F} = \mathbf{I} + \mathbf{J}$, denoted by $|F, m_F\rangle$, and the corresponding eigenenergies are

$$E_{hf}\left(F, m_F\right) = \frac{1}{2}\left[F\left(F+1\right) - I\left(I+1\right) - J\left(J+1\right)\right] \tag{2.20}$$

The static magnetic field introduces an interaction energy of $\boldsymbol{\mu} \cdot \mathbf{B}$, in terms of angular momentum, the Hamiltonian is given by [62]

$$H = A\mathbf{I} \cdot \mathbf{J} + (g_I \mu_B \mathbf{I} + g_J \mu_B \mathbf{J}) \cdot \mathbf{B}. \tag{2.21}$$

Now $|F, m_F\rangle$ are no longer the eigenstates and in the limit of $\mu_B B \gg A$, the eigenstates are $|m_I, m_J\rangle$. However, the general eigenstates have one-to-one connections with each $|F, m_F\rangle$ when $B \to 0$, and $|m_I, m_J\rangle$ when $B \to \infty$. Hence they are still denoted conveniently by $|F, m_F\rangle$ in usual range of magnetic field. For alkaline metal atoms in the ground state, $J = 1/2$, and the eigenenergies have an analytical expression referred to as Breit-Rabi formula

$$E\left(F = I \pm \frac{1}{2}, m_F\right) = -\frac{\Delta E_{\text{hfs}}}{2\left(2I+1\right)} - m_F g_I \mu_B B \pm \frac{\Delta E_{\text{hfs}}}{2}\sqrt{1 + \frac{4m_F}{2I+1}x + x^2}, \tag{2.22}$$

where

$$x = \frac{\left(g_J \mu_B - g_J \mu_B\right) B}{\Delta E_{\text{hfs}}}. \tag{2.23}$$

The Zeeman shift for each hyperfine states in ground state ^{87}Rb are shown in Fig. 2.1. For atoms with $J > 1/2$, e.g., in the excited state with $J = 3/2$, there is no unified analytical expression, but the solution can be found by diagonalizing the Hamiltonian 2.21 in the direct product space of $\mathbf{I}$ and $\mathbf{J}$, which is in the $(2I + 1)(2J + 1)$ by $(2I + 1)(2J + 1)$ matrix form. This problem has significance in studying the shift of optical transitions in high magnetic field. A calculation using Mathematica with the add-on “Quantum” [63] is shown in Fig. 2.2.

According to Maxwell’s equations, only magnetic field minimum can be generated in current-free region in space while maximum cannot exist. Hence only states with positive magnetic can have potential minimum and be trapped. From Eq. 2.22, these low-field seeking states are $|1, -1\rangle$, $|2, 1\rangle$ and $|2, 2\rangle$ for Rb and Na ($I = 3/2$).

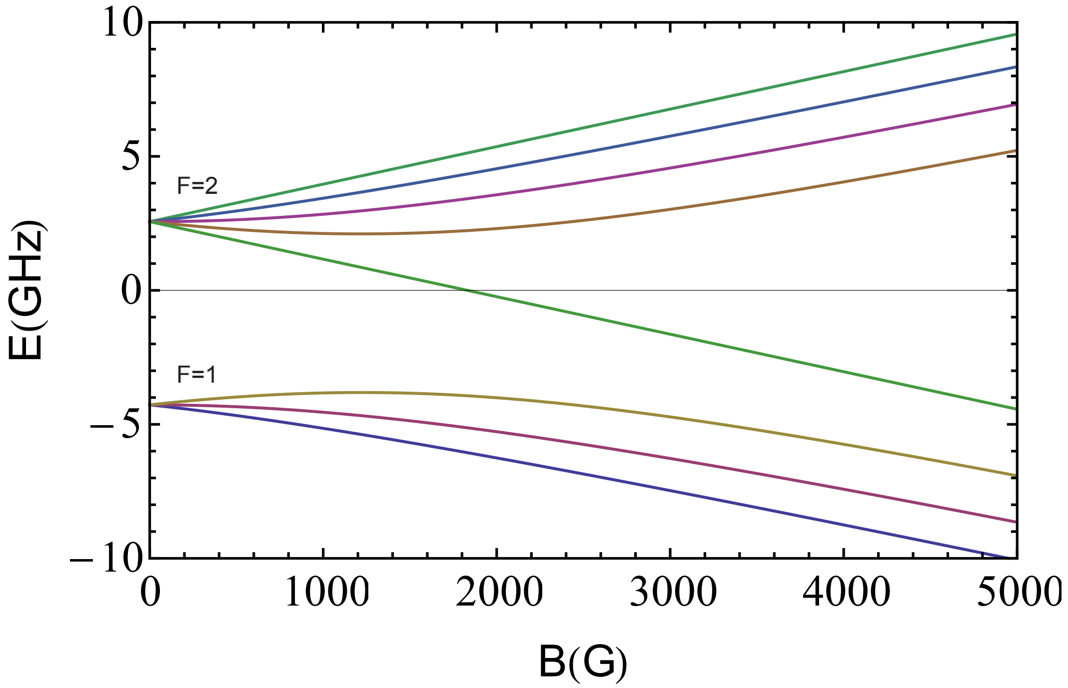

Figure 2.1: ^{87}Rb $5^2S_{1/2}$ hyperfine structure and Zeeman shift in external magnetic field, according the the Breit-Rabi formula 2.22. The labels denote the asymptotic hyperfine state for each level when $B \to 0$.

The simplest magnetic trap is quadrupole trap (QT), which is generated by a pair of anti-Helmholtz coil, with the currents running in the same direction. According to $\nabla \cdot \mathbf{B} = 0$ and the axial symmetry, the magnetic field near the center of the coil pair must have the form

$$\mathbf{B} = B' \left(x, y, -2z\right), \tag{2.24}$$

where B' is the magnetic field gradient along x and y direction, hence the magnitude of the magnetic field is given by

$$\begin{aligned} B &= B'\sqrt{x^2+y^2+4z^2} \\ &= B'r\sqrt{\frac{5+3\cos 2\theta}{2}}, \quad \text{(in spherical coordinate)} \end{aligned} \tag{2.25}$$

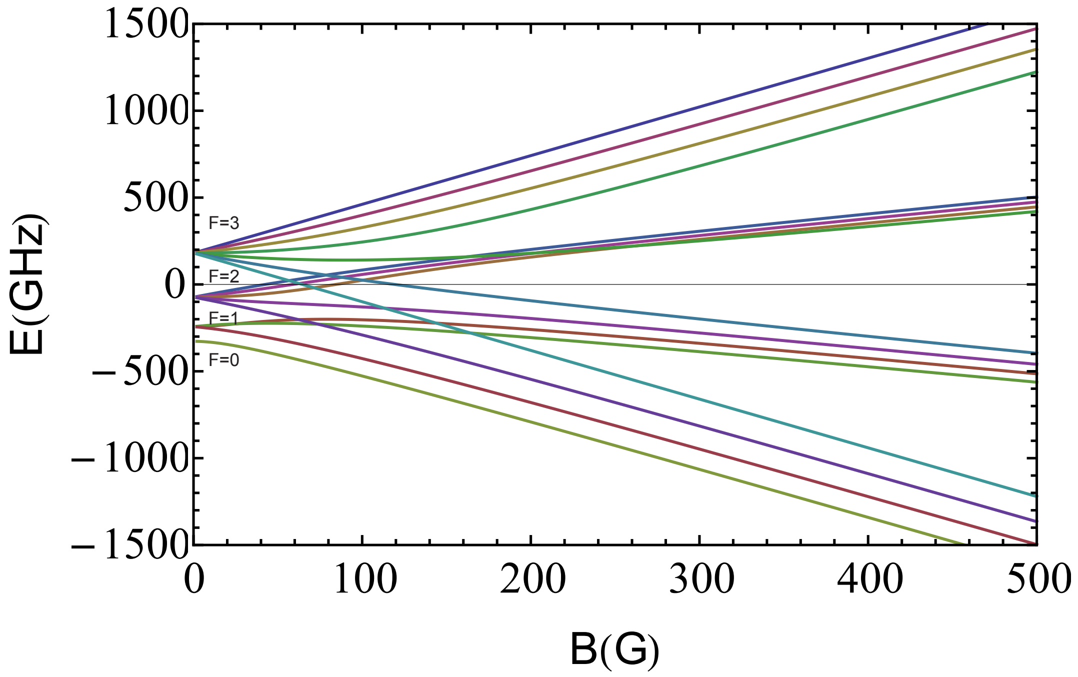

Figure 2.2: ^{87}Rb $5^2P_{3/2}$ hyperfine structure and Zeeman shift in external magnetic field. The labels denote the asymptotic hyperfine state for each level when $B \to 0$. The result are obtained by numerically diagonalized the Hamiltonian 2.21, for $I = 3/2$ and $J = 3/2$.

Hence the potential is linear along any direction, and the gradient along axial direction is two times that along the radial direction.

QT provides strong confinement and good optical access as well as high evaporative cooling efficiency. However the drawback is the the presence of zero magnetic field point in the center, which causes Majorana loss of a ultracold atomic cloud and limit the lowest achieved temperature. This is because the magnetic field direction has an sudden change across the zero point, and the atoms can not follow the magnetic field and retain the local spin state. Once the spin state is changed the atom is no longer trapped. The Majorana loss rate for an atomic cloud at temperature T can be estimated

$$\Gamma = \chi \frac{\hbar}{m} \left(\frac{0.5 \mu_B B'}{k_B T} \right)^2, \tag{2.26}$$

where χ is a proportional constant. The loss and heating become significant before the cloud is cooling to quantum degeneracy. In order to overcome this difficulty, several kinds of traps have been designed to eliminate the zero field point such as Ioffe-Pritchard trap and time orbiting potential trap, or displace the trap center away from the zero field point such as the the hybrid trap consist of QT and displaced ODT Sec. 4.4.

2.2.2 Optical Dipole Trap

Optical dipole trap provides another kind of trap for neutral atoms utilizing the dipole force. The important advantage of ODT is that all spin states can be trapped in contrast to magnetic traps, hence release the spin degree of freedom and enable the study of a new field, namely spinor gases.

In a two-level system, the AC stark shift is given by Eq. 2.13. The Rabi frequency Ω is related to the light intensity $I = c\varepsilon_0 \mathbf{E}^2/2$ and field amplitude by

$$\Omega = \frac{\langle g| e\mathbf{r} |e\rangle \cdot \mathbf{E}}{\hbar}, \tag{2.27}$$

and the transition dipole moment is related to the spontaneous decay rate by

$$\Gamma = \frac{\omega_0^3}{3\pi\varepsilon_0 \hbar c^3} |\langle g| e\mathbf{r} |e\rangle|^2. \tag{2.28}$$

Combining above equations, the trapping potential is given by

$$U(\mathbf{r}) = \frac{3\pi c^2}{2\omega_0^3} \frac{\Gamma}{\Delta} I(\mathbf{r}). \tag{2.29}$$

This is usually accurate enough to describe a far-off-resonant trap (e.g., 1070nm ODT for ^{87}Rb with 780nm and 795nm transitions). In a real atom with multi energy levels, perturbation calculation up to second order considering all energy levels gives a more general expression

$$U_i\left(\mathbf{r}\right)=-\sum_j\frac{1}{c\varepsilon_0}\left(\frac{1}{\omega_{ji}-\omega}+\frac{1}{\omega_{ji}+\omega}\right)\frac{\left|\left\langle i\right|\hat{\varepsilon}\cdot e\mathbf{r}\left|j\right\rangle\right|^2}{\hbar}I\left(\mathbf{r}\right). \tag{2.30}$$

The accuracy is increased by considering the fine structure and hyperfine structure successively and substituting corresponding transition dipole moments. Here $\hat{\varepsilon}$ is the polarization vector for the light field. If the polarization has circular component, there small different in the shifts for differen m_F Zeeman sublevels. This vector light shift is found to have dramatic effect on the heteronuclear spinor dynamics in a spinor mixture.

According to Eq. 2.29, the ODT can be achieved by generating a light intensity field that have maximum in space. This is realized by a usual Gaussian beam with beamwaist w_0 and power P propagating along z direction, which intensity can be expressed as

$$\begin{aligned} I\left(x,y,z\right)&=\frac{2P}{\pi w(z)^2}\exp\left[-\frac{2\left(x^2+y^2\right)}{w(z)^2}\right]\\ w\left(z\right)&=w_0\sqrt{1+\left(\frac{z}{z_r}\right)^2}. \end{aligned} \tag{2.31}$$

where $z_r=\pi w_0^2/\lambda$ is the Rayleigh length. Hence the trap depth is given by

$$U_0=-\frac{3\pi c^2}{2\omega_0^3}\frac{\Gamma}{\Delta}\frac{2P}{\pi w_0^2}. \tag{2.32}$$

Near the trap center, the ODT can be approximated by harmonic trap

$$\begin{aligned} U\left(\mathbf{r}\right)&=-U_0\frac{w_0^2}{w(z)^2}\exp\left[-\frac{2\left(x^2+y^2\right)}{w(z)^2}\right]\\ &\approx-U_0+\frac{2U_0}{w_0^2}x^2+\frac{2U_0}{w_0^2}y^2+\frac{U_0}{z_r^2}z^2\\ &=-U_0+\frac{1}{2}m\omega_x^2x^2+\frac{1}{2}m\omega_y^2y^2+\frac{1}{2}m\omega_z^2z^2. \end{aligned} \tag{2.33}$$

with trap frequencies

$$\omega_x = \sqrt{\frac{4U_0}{mw_0^2}}, \omega_y = \sqrt{\frac{4U_0}{mw_0^2}}, \omega_z = \sqrt{\frac{2U_0}{mz_r^2}}. \tag{2.34}$$

The single beam ODT has a weak confinement in z direction and strong confinement in x and y dirction, so the atom cloud in this trap is cigar shape. To form a near isotropic 3D trap, we can superimpose two Gaussian beams with certain intersection angle.

2.2.3 Magneto Optical Trap

As described in Sec. 2.1, radiation-pressure force can be used to cooling atoms by by three pair of counterpropagating red detuned beams. Making use of Zeeman effect, a pair of anti-Helmholtz coil combined with the six laser beam can be used to trap atoms in real space. This ingenious idea can be illustrated in one dimensional case, as depicted in Fig. 2.2.3. The magnetic gradient field indicates that for $z > 0$, $B(z) > 0$ (point to right); for $z < 0$, $B(z) < 0$ (point to left); $B(0) = 0$. The red detuned counterpropagating beams have both clockwise circular polarization with respect to their propagating directions, but it should be cautioned that the polarization are denoted as σ^+ and σ^- with respect to the z axis. The Zeeman shift of the energy levels given by Eq. 2.22 can be approximated by linear shift at low magnetic field:

$$\Delta E = g_F m_F \mu_B B. \tag{2.35}$$

Consider an atom placed at $z > 0$, the local magnetic field is point to right, hence the σ^+ drive $m_F = 0 \to +1$ transition, and σ^- drive $m_F = 0 \to -1$ transition. However, due to the Zeeman shift, the σ^--light is more near resonant to $m_F = 0 \to -1$ transition and gives larger force according to Eq. 2.18. Hence the total force points to the left. Opposite force obtained when the atom is placed at $z < 0$

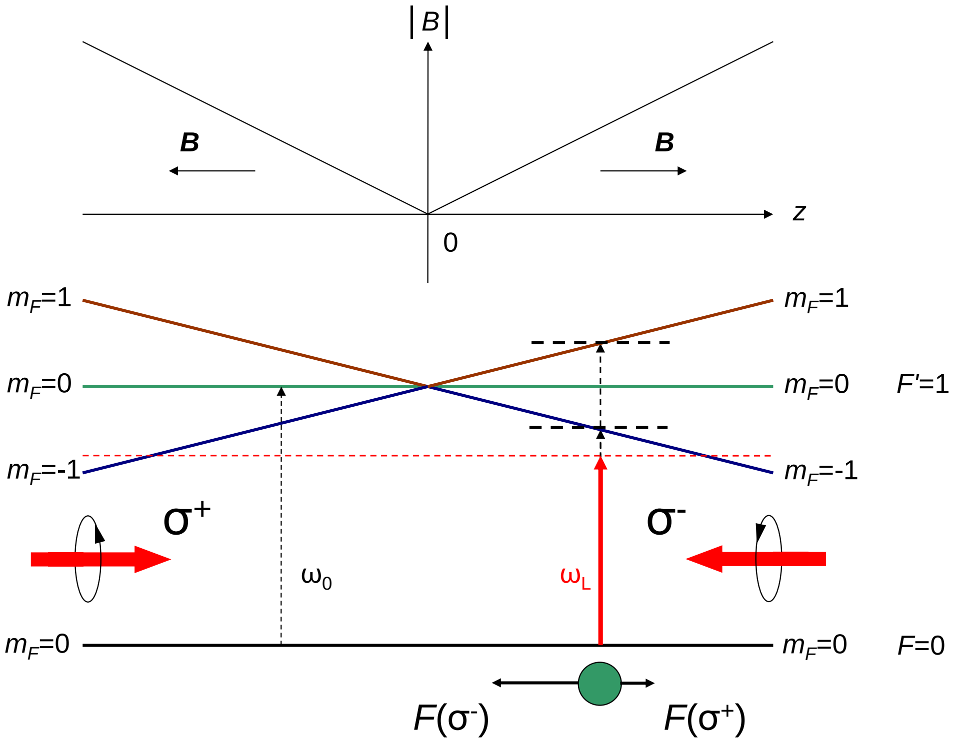

Figure 2.3: Principle of MOT illustrated in one dimension. The magnitude and direction of the magnetic field is shown in the upper curve. The energy levels for $F = 0$ and $F' = 1$ split in the magnetic field gradient as shown in the lower part. An atom placed in the indicated position experience a larger force from the σ^--light and smaller force from σ^+-light, due to corresponding shifts in the atomic transitions, as explained in the text.

where the local field point to left. A detailed calculation give the restoring force in one dimension

$$F_{\text{MOT}} = -\alpha v - \beta z, \tag{2.36}$$

where

$$\begin{aligned} \alpha &= 2k\frac{\partial F_{\text{rad}}}{\partial \omega} \\ \beta &= 2g_F\mu_B B'\frac{\partial F_{\text{rad}}}{\partial \omega}. \end{aligned} \tag{2.37}$$

The 3D MOT is composed of a 3D gradient field and six counterpropagating beams in three orthogonal directions, which configuration is shown in Fig. 2.4.

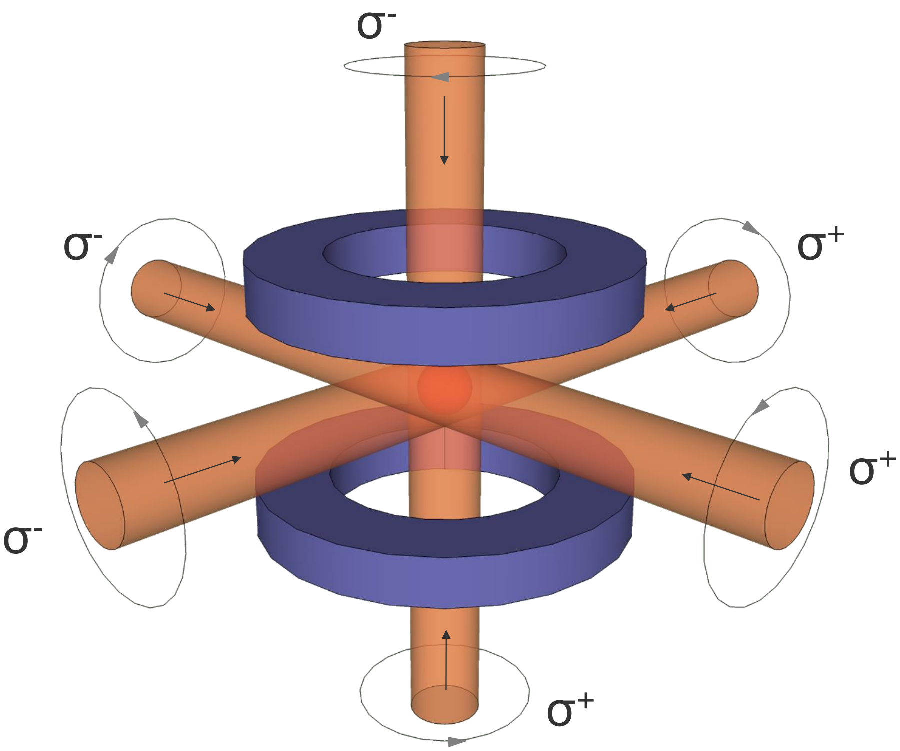

Figure 2.4: Configuration of a 3D MOT. Six counterpropagating beams in three orthogonal directions are crossed in the center of the antiHelmholtz coil producing the magnetic gradient field. All propagation directions and polarizations are indicated. The polarizations are defined with respected to the positive direction in each directions.

The above argument assume an $F = 0 \rightarrow F' = 1$ transition, but the basic principle applies to other $F \rightarrow F' = F + 1$ transitions. In real atoms, atoms have a little probability to be pumped to $F' = F$ state and decay to $F - 1$ hyperfine state in the ground state, hence a repumping light driving $F - 1 \rightarrow F' - 1$ is needed to complete the MOT cycle.

2.3 Trapping and Cooling of Atoms

2.3.1 CMOT and Molasses

MOT is the workhorse in current experiment trapping neutral atoms, because it provides strong confinement and direct cooling for atoms from room temperature to about hundreds of microKelvin. However, the cooling mechanism based on Doppler effect has a limiting temperature called Doppler limit

$$T_D = \frac{\hbar\Gamma}{2k_B}. \tag{2.38}$$

The Doppler limit is due to the random and discrete spontaneous decay events balancing the Doppler cooling process. For Rb and Na, the Doppler limit is 144μK and 235μK respectively, which is still far from quantum degeneracy. To reach high phase-space density, two procedures are widely adopted before loading to magnetic trap or ODT for further evaporative cooling, namely the CMOT and molasses. Here we briefly describe their working principles.

In MOT, the achieved density is major limited by the collisions between atoms. The increase of the magnetic field gradient is proposed after the MOT stage, in order to compress the MOT and increase the density of the atomic cloud. Meanwhile it is found that increasing the laser detuning can reduce the reradiatin force, hence larger detuning is favored in the CMOT stage.

The CMOT is followed by the molasses stage for cooling to below Doppler temperature, which strictly speaking is polarization gradient cooling, since the word molasses is initilly used to decribe Doppler cooling. The magnetic gradient field is turned off, and along each direction, the counterpropagating σ^+-σ^- beams form a standing wave pattern, in which the electric field is linear everywhere, but the direction rotation with periodicity of λ. For steady state of atoms in local linear field, the populated distribution in m_F Zeeman sublevels are symmetric and mostly in $m_F = 0$. If the atom moves along one beam, it experiences a rotation of the quantization axis, and the population distribution cannot adiabatically follows. It is shown in [64] that atoms moving to σ^+ beam lead to population shift to $m_F = +1$ state, thus causing a imbalance of the radiation-pressure forces exerted by the two beam with opposite polarizations. The imbalanced by this mechanism is much more sensitive to that in Doppler cooling, and hence produces a stronger damping. The theoretical achieved temperature is the recoil limit

$$T_{\text{rec}} = \frac{\hbar^2 k^2}{2mk_B}. \tag{2.39}$$

which can below 1μK. The laser detuning and intensity are also investigated in [64] and it is found that increasing detuning and decreasing intensity are flavored.

2.3.2 Evaporative Cooling

The usually achieved temperature in laser cooling is about several to several tens of microKelvins, limiting by the photon scattering in the presence of resonant laser lights. Thus the quantum degenerate gases are obtained by evaporative cooling in magnetic traps and ODTs [65].

The principle of evaporative cooling is rather comprehensible. A thermal cloud in equilibrium has a Maxwellian momentum distribution. If we are able to remove the hot atoms in the high energy tail in the distribution, the remaining atoms will reach a lower temperature after equilibrium through elastic collisions. This is just like the cooling of a cup of water through evaporation, but usually the atomic gas undergoes forced evaporation continuously.

The realization of evaporative cooling in magnetic trap and ODT is to lower the trap depth from top to bottom, since the atoms with high energy are more likely to appear at the outer part of the trap. The implementation in magnetic trap is through microwave or RF evaporation, where the frequency is continuously scanned corresponding to the spin state resonant transitions from outer part to the inner part of the trap. The atoms undergo transitions will change to high field seeking state and is ejected from the magnetic trap. This method is often referred to as a microwave or rf "knife" which cut the atoms with energy higher than the corresponding transition frequency.

The evaporative cooling in ODT is more straightforward. Since the trap usually has Gaussian shape and a finite trap depth, which is proportional to the light intensity, lowering the trap depth is realized by continuously decreasing the power of the ODT. The two kinds of evaporative cooling in schematically illustrated in Fig. 2.5.

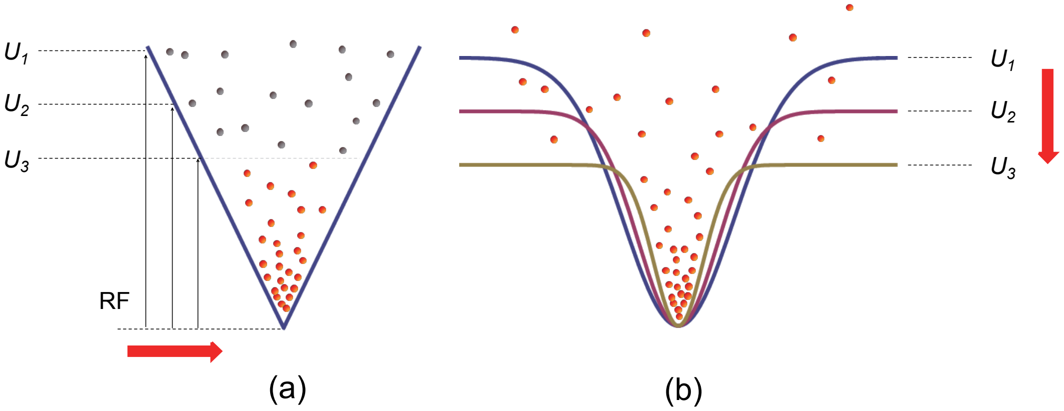

Figure 2.5: Diagrammatic illustrations of the evaporative cooling in (a) quadrupole trap and (b) optical dipole trap. Both trap depths are lowered from U_1 to U_3. In QT, this is achieved by the RF or microwave frequency sweep, while in ODT, the power which proportional to the trap depth is ramped down.

The efficiency of evaporative cooling depends critically on the collisional properties of the atoms. The elastic collisions should be fast enough to keep thermalization during the cooling process, while inelastic collisions lead to atom loss and is against evaporative cooling. Hence the it is necessary to have a reasonable ratio of elastic to inelastic collisions. The rate for the former is proportional to the elastic collision cross section which is determined by the s-wave scattering length by $\sigma_{el} = 8\pi a^2$, while the situation is much more complex for inelastic collisions which includes background collisions, two-body and three-body collisions. Usually the efficiency is quite high for ^{87}Rb which has a moderate scattering length $a = 103a_0$, while the severe two-body loss makes the evaporative cooling for ^{85}Rb and ^{133}Cs (both with $a > 2000a_0$) difficult. Also, evaporative cooling is not applicable for Fermionic species such ^{40}K in which the s-wave scattering is forbidden. Thus sympathetic cooling is needed in studying these atomic species.

2.3.3 Sympathetic Cooling

As mentioned above, sympathetic cooling is a useful scheme for some atomic species [66–80]. The method is to use an atomic species which has good evaporative cooling efficiency to be a coolant, meanwhile keep the target species overlap with the coolant in the trap. Interspecies elastic collisions lead to thermalization between the two species, and the temperature of the target species is lowered during the evaporative cooling process. Similar to the thermalization process in single species, the efficiency of sympathetic cooling depends largely on the interspecies s-wave scattering length. In addition, the spatial overlap of the two clouds is also an important factor. The collision rate is given by $\Gamma_{\text{in}} = \sigma_{\text{in}}\bar{v}\bar{n}$, where σ_{in} is the interspecies elastic cross section determined by the s-wave scattering length a_{in}, $\bar{v} = \sqrt{(8k_B/\pi)\left(T_1/m_1 + T_2/m_2\right)}$ is the mean thermal relative velocity, $\bar{n} = (1/N_1 + 1/N_2)\int n_1(\mathbf{r})\, n_2(\mathbf{r})\, d^3\mathbf{r}$ is the overlap density of the two cloud. Then the temperature difference between the two species evolves according to

$$\frac{d}{dt}(\Delta T) = -\gamma\Delta T, \tag{2.40}$$

where the thermalization rate $\gamma = \Gamma\xi/2.7$, with $\xi = 4m_1m_2(m_1+m_2)^{-2}$, as it is found that about $2.7/\xi$ collisions is needed for crossspecies thermalization. The sympathetic cooling scheme is found to work well in atomic mixtures with appropriate scattering length and overlap such as ^{87}Rb -^{85}Rb, ^{87}Rb -^{40}K, ^{87}Rb

-^{7}Li, while not so efficient for ^{87}Rb -^{6}Li due to small scattering length.

In our case, both ^{87}Rb and ^{23}Na have good evaporative cooling efficiency. However, since ^{23}Na number is two orders of magnitude smaller than ^{87}Rb in MOT, it is reasonable to adopt the sympathetic cooling scheme using ^{87}Rb as coolant in the evaporative cooling in magnetic trap. In contrast, since the trap depth of ^{23}Na is much shallower than ^{87}Rb in ODT, the former serves as coolant in evaporative cooling in this stage. Due to moderate interspecies scattering length ($a_{\text{in}} = 73a_0$), the sympathetic cooling is found to be very efficient and plays an important role in our preparation of the ultracold mixture [81].

2.4 BEC and GP Equation

From the view of statistical mechanics, the origin of BEC is that a cloud of bosons obey Bose-Einstein statistics instead of Maxwell-Boltzmann statistics. Specifically the distribution function has the form of Bose distribution

$$f(\varepsilon_\nu) = \frac{1}{e^{-\frac{\mu-\varepsilon_\nu}{kT}} - 1}, \tag{2.41}$$

where $f(\varepsilon_\nu)$ is the mean occupation number of the single-particle state ν; ε_ν is the energy associated with state ν; μ is the chemical potential, T is the temperature. From this expression, for lower temperature, the states with lower energy become more populated. BEC occurs when the lowest energy state is macroscopically occupied. The number of condensate fraction below the transition temperature is found to be

$$\frac{N_0}{N} = 1 - \left(\frac{T}{T_c}\right)^3. \tag{2.42}$$

It is this condensate fraction that caused great interests and intensive studies in the past several decades, since it forms a new material with most of its constituent particles in a single quantum state.

We do not take into account the interaction of particles when demonstrating the origin of BEC, but studying the weakly interacting Bose gas has practical significance as interactions always exist in currently available ultracold gases. In order to model the problem in the simplest zero temperature case, we start from the most general form of the Hamiltonian for a many-body system with two-body interaction for every two particles [82]

$$H = \sum_{rs} a_r^\dagger \langle r|T|s\rangle a_s + \frac{1}{2}\sum_{rstu} a_r^\dagger a_s^\dagger \langle rs|V|tu\rangle a_u a_t, \tag{2.43}$$

where $\langle r|T|s\rangle$ is the matrix element of one-body operator T (kinetic energy, external potential, ...), $\langle rs|V|tu\rangle$ is the matrix element of two-body interaction operator V coupling the states in which particle 1 is at r, t and particle 2 at s, u. When only spatial degree of freedom is involved, working in the continuous coordinate representation, $a_s = a_{\mathbf{x}} = \psi(\mathbf{x})$, $\sum\limits_{rs} = \iint d\mathbf{x}d\mathbf{x}'$, noticing $\langle r|T|s\rangle = \langle \mathbf{x}|T|\mathbf{x}'\rangle = \delta\left(\mathbf{x}-\mathbf{x}'\right)T(\mathbf{x})$ and $\langle rs|V|tu\rangle = \langle \mathbf{x}\mathbf{x}'|V|\mathbf{y}\mathbf{y}'\rangle = \delta\left(\mathbf{x}-\mathbf{y}\right)\delta\left(\mathbf{x}'-\mathbf{y}'\right)\langle \mathbf{x}\mathbf{x}'|V|\mathbf{x}\mathbf{x}'\rangle = \delta\left(\mathbf{x}-\mathbf{y}\right)\delta\left(\mathbf{x}'-\mathbf{y}'\right)V(\mathbf{x},\mathbf{x}')$, we have

$$H = \int d\mathbf{x}\psi^\dagger(\mathbf{x})T(\mathbf{x})\psi(\mathbf{x}) + \frac{1}{2}\iint d\mathbf{x}d\mathbf{x}'\psi^\dagger(\mathbf{x})\psi^\dagger(\mathbf{x}')V(\mathbf{x},\mathbf{x}')\psi(\mathbf{x}')\psi(\mathbf{x}). \tag{2.44}$$

In Heisenberg picture, the dynamical equation for the field operator is given by the Heisenberg equation,

$$i\hbar\frac{\partial}{\partial t}\psi\left(\mathbf{x},t\right) = \left[\psi\left(\mathbf{x},t\right), H\right], \tag{2.45}$$

or

$$\frac{\partial}{\partial t}\psi\left(\mathbf{x},t\right) = \frac{1}{i\hbar}\left[-\frac{\hbar^2}{2m}\nabla^2 + U\left(\mathbf{x}\right) + \int d\mathbf{x}'\psi^\dagger\left(\mathbf{x}',t\right)V\left(\mathbf{x},\mathbf{x}'\right)\psi\left(\mathbf{x}',t\right)\right]\psi\left(\mathbf{x},t\right). \tag{2.46}$$

Now we assume the two-body interaction has the form of contact interaction

$$V\left(\mathbf{x},\mathbf{x}'\right)=g\delta\left(\mathbf{x}-\mathbf{x}'\right), \tag{2.47}$$

where $g=4\pi\hbar^2 a/m$ with a being the s-wave scattering length, and make the mean-field approximation, that is, replace the field operator by its mean value $\psi\left(\mathbf{x},t\right)\rightarrow\left\langle\psi\left(\mathbf{x},t\right)\right\rangle\equiv\phi\left(\mathbf{x},t\right)$, the above equation is turned into the time-dependent Gross-Pitaevski equation

$$\frac{\partial}{\partial t}\phi\left(\mathbf{x},t\right)=\left[-\frac{\hbar^2}{2m}\nabla^2+U\left(\mathbf{x}\right)+g\left|\phi\left(\mathbf{x},t\right)\right|^2\right]\phi\left(\mathbf{x},t\right). \tag{2.48}$$

By substituting $\phi\left(\mathbf{x},t\right)=\phi\left(\mathbf{x}\right)\exp\left(-i\mu t/\hbar\right)$, we get the time-independent GPE.

$$\left[-\frac{\hbar^2}{2m}\nabla^2+U\left(\mathbf{x}\right)+g\left|\phi\left(\mathbf{x},t\right)\right|^2\right]\phi\left(\mathbf{x},t\right)=\mu\phi\left(\mathbf{x},t\right). \tag{2.49}$$

These two equations are powerful in the sense that they are the fundamental equations for describing a wide range of properties of a BEC in the mean field level, which is accurate enough under most circumstances in an atom trap. For example, one can find the ground state by solving Eq. 2.49 for particular trap potential; by introducing a density fluctuation term from the ground state $n\left(\mathbf{x},t\right)=n_0\left(\mathbf{x}\right)+\tilde{n}\left(\mathbf{x},t\right)$ and solving Eq. 2.48, one can find the elementary excitations; by introducing additional rotation terms, vortices in the condensate can be investigated.

The GPE can be generalized to multicomponent system, which contains BEC of two or more atomic species, or BEC of different internal state in a single spcies. For a two-species BEC, the system is describe by coupled GPE

$$\begin{aligned} i\hbar\frac{\partial\phi_1}{\partial t} &= \left(-\frac{\hbar^2\nabla^2}{2m_1}+U_1+N_1g_{11}\left|\phi_1\right|^2+N_2g_{12}\left|\phi_2\right|^2\right)\phi_1 \\ i\hbar\frac{\partial\phi_2}{\partial t} &= \left(-\frac{\hbar^2\nabla^2}{2m_2}+U_2+N_2g_{22}\left|\phi_1\right|^2+N_1g_{12}\left|\phi_1\right|^2\right)\phi_2, \end{aligned} \tag{2.50}$$

where $g_{ij} = \frac{2\pi\hbar^2 a_{ij}}{m_{ij}}, m_{11} = m_1/2, m_{22} = m_2/2, m_{12} = \frac{m_1 m_2}{m_1+m_2}$, a_{11} and a_{22} are the single species scattering lengths and $a_{12} = a_{21}$ is the interspecies scattering length. The solutions to the coupled GPE are discussed in many theoretical works. An interesting finding is that when $g_{12}^2/g_{11}g_{22} > 1$, the strong interspecies repulsive interaction lead to immiscibility of the two BECs [32, 83–85], which menifest as a “ball and shell” density profile. The prediction is nicely verified in many experiments studying the mixture of BECs, which provide a tool for further comparison between experiment and mean field theory.

Chapter 3

Theoretical Background: Spinor Gases

In this chapter the necessary theoretical background of spinor gases will be given. We start by introducing the spin degree of freedom in single particle picture, demonstrating how the spin behave under DC and AC magnetic field in section 3.1. Then we consider the many-body spin-1 system in the presence of two-body interaction in section 3.2. Starting from the second quantization formalism, we adopt the mean-field approximation and single-mode approximation and calculate the ground state and coherent dynamics. The behaviors beyond these two approximations are also discussed briefly. In section 3.3 we generalize the theoretical description of single species spinor gas to two species case. A simple two level picture is discussed followed by a mean-field calculation, and a thorough treatment considering the thermal nature of one of the species is given in terms of Boltzmann equation.

3.1 Single Particle Description

3.47

3.1.1 Linear and Quadratic Zeeman shift

In Sec. 2.2 we have shown that an atom with nuclear angular momentum **I** and electronic total angular momentum **J** in a static magnetic field **B** is described by the Hamiltonian 2.21, and the Zeeman shift is given by the Breit-Rabi formula 2.22. Let $I = 3/2$ and expand the energy in power series of B to second order, for $F = 1$ we have

$$\begin{aligned} E\left(m_F\right) &= -\frac{5\Delta E_{\text{hfs}}}{8} - \left(\frac{g_J - 5g_I}{4}\right) m_F \mu_B B - \frac{\left(g_J - g_I\right)^2}{4\Delta E_{\text{hfs}}}\left(1 - \frac{m_F^2}{4}\right)\mu_B^2 B^2 \\ &= E_0 - p m_F + q m_F^2, \end{aligned} \tag{3.1}$$

where

$$\begin{aligned} E_0 &= -\frac{5\Delta E_{\text{hfs}}}{8} - \frac{\left(g_J - g_I\right)^2 \mu_B^2 B^2}{4\Delta E_{\text{hfs}}} \\ p &= \left(\frac{g_J - 5g_I}{4}\right)\mu_B B \\ q &= \frac{\left(g_J - g_I\right)^2}{16\Delta E_{\text{hfs}}}\mu_B^2 B^2. \end{aligned} \tag{3.2}$$

Now the Hamiltonian for a spin-1 atom can be effectively written as (dropping the spin-independent part) the sum of linear and quadratic Zeeman shift

$$H_Z = -\hbar p F_z + \hbar q F_z^2. \tag{3.3}$$

Here F_z is the z-component of the angular momentum matrix divided by $\hbar$ for spin $F = 1$,

$$F_x = \frac{1}{\sqrt{2}}\begin{pmatrix} 0 & 1 & 0 \\ 1 & 0 & 1 \\ 0 & 1 & 0 \end{pmatrix}, F_y = \frac{i}{\sqrt{2}}\begin{pmatrix} 0 & -1 & 0 \\ 1 & 0 & -1 \\ 0 & 1 & 0 \end{pmatrix}, F_z = \begin{pmatrix} 1 & 0 & 0 \\ 0 & 0 & 0 \\ 0 & 0 & -1 \end{pmatrix} \tag{3.4}$$

Similarly results hold for $F = 2$, except the linear and quadratic shift become

$$\begin{aligned} p &= -\left(\frac{g_J - 3g_I}{4}\right)\mu_B B \\ q &= -\frac{\left(g_J - g_I\right)^2}{16\Delta E_{\text{hfs}}}\mu_B^2 B^2, \end{aligned} \tag{3.5}$$

and the angular momentum matrices become

$$\begin{aligned} F_x &= \begin{pmatrix} 0 & 1 & 0 & 0 & 0 \\ 1 & 0 & \sqrt{\frac{3}{2}} & 0 & 0 \\ 0 & \sqrt{\frac{3}{2}} & 0 & \sqrt{\frac{3}{2}} & 0 \\ 0 & 0 & \sqrt{\frac{3}{2}} & 0 & 1 \\ 0 & 0 & 0 & 1 & 0 \end{pmatrix}, F_y = \begin{pmatrix} 0 & -i & 0 & 0 & 0 \\ i & 0 & -i\sqrt{\frac{3}{2}} & 0 & 0 \\ 0 & i\sqrt{\frac{3}{2}} & 0 & -i\sqrt{\frac{3}{2}} & 0 \\ 0 & 0 & i\sqrt{\frac{3}{2}} & 0 & -i \\ 0 & 0 & 0 & i & 0 \end{pmatrix} \\ F_z &= \begin{pmatrix} 2 & 0 & 0 & 0 & 0 \\ 0 & 1 & 0 & 0 & 0 \\ 0 & 0 & 0 & 0 & 0 \\ 0 & 0 & 0 & -1 & 0 \\ 0 & 0 & 0 & 0 & -2 \end{pmatrix} \end{aligned} \tag{3.6}$$

3.1.2 AC magnetic field

In the presence of static magnetic field, the evolution of the spin state is simply Larmor precession, and the populations of each component does not change. If an oscillating magnetic field along the transverse direction is applied, different components are coupled and show Rabi oscillations. This can be used to prepare certain initial states in experiments. In such situations, the system is described by the Hamilonian

$$H = -\hbar p F_z + \hbar q F_z^2 + 2\hbar\Omega\cos\left(\omega t\right) F_y$$

assuming that the AC magnetic field is along y-axis, with frequency ω and Rabi frequency Ω.

Working in the rotating frame, i.e., under a unitary transformation $T = e^{-i\omega t F_z}$, a quantum state $|\psi(t)\rangle$ is transformed to

$$\left|\tilde{\psi}(t)\right\rangle = T\left|\psi(t)\right\rangle$$

to ensure the validity of Schrodinger equation, the Hamiltonian must have the form after rotating-wave approximation [60]

$$\tilde{H} = THT^{-1} + i\hbar\dot{T}T^{-1} = -\hbar(p-\omega)F_z + \hbar q F_z^2 + \hbar\Omega F_y$$

The time evolution of the initial state can be calculated using the time-evolution operator.

$$\tilde{U}(t) = e^{-i\tilde{H}t/\hbar}$$

For example, if the initial state is in $|-1\rangle$, in matrix form we can write

$$\left|\tilde{\psi}(0)\right\rangle = \begin{pmatrix} 0 \\ 0 \\ 1 \end{pmatrix} \begin{array}{l} m_F = 1 \\ m_F = 0 \\ m_F = -1 \end{array}$$

and the Hamiltonian in rotating frame is

$$\tilde{H} = \frac{\hbar}{\sqrt{2}} \begin{pmatrix} \frac{q}{2\sqrt{2}} & -i\Omega & 0 \\ i\Omega & 0 & -i\Omega \\ 0 & i\Omega & \frac{q}{2\sqrt{2}} \end{pmatrix}. \tag{3.7}$$

If we choose a duration of the AC magnetic field so that $\Omega t = \pi/3$, the time-

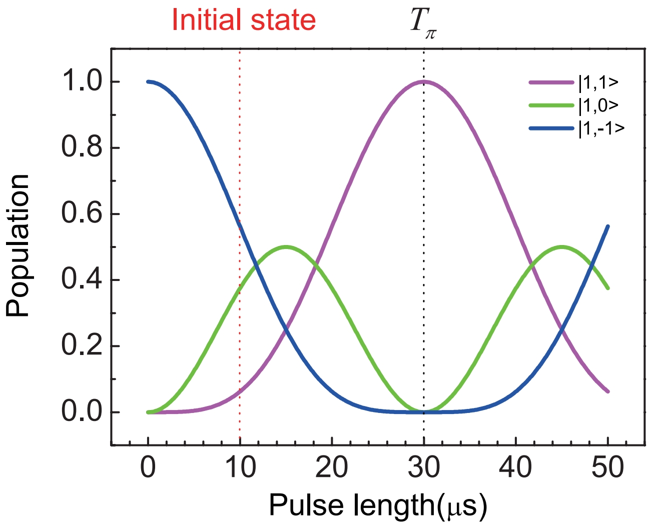

Figure 3.1: Rabi oscillation of a spin-1 atom with resonant rf couping. The three spin components exhibit sinusoidal oscillation, with maximum population 1 for $|-1\rangle$ and $|1\rangle$, and 0.5 for $|0\rangle$, indicated by different color lines. T_π is defined as the minimum time to completely transfer the population from $|-1\rangle$ to $|1\rangle$. In our experiment of spinor dynamics in a mixture, the initial state is the one with $T_\pi/3$ pulse length, indicated by the red dotted line.

evolution operator can be calculated numerically,

$$\tilde{U}(t) \approx \begin{pmatrix} 0.75-0.0009\mathrm{i} & -0.61+0.0003\mathrm{i} & 0.25-0.0002\mathrm{i} \\ 0.61-0.0003\mathrm{i} & 0.5+0.0002\mathrm{i} & -0.61+0.0003\mathrm{i} \\ 0.25-0.0002\mathrm{i} & 0.61-0.0003\mathrm{i} & 0.75-0.0009\mathrm{i} \end{pmatrix} \tag{3.8}$$

The state after the pulse is

$$\left|\tilde{\psi}(t)\right\rangle \approx \begin{pmatrix} 0.2500-0.0002\mathrm{i} \\ -0.6124+0.0003\mathrm{i} \\ 0.7500-0.0009\mathrm{i} \end{pmatrix} \approx \begin{pmatrix} \sqrt{0.0625}e^{i(-0.05^\circ)} \\ \sqrt{0.3750}e^{i(179.97^\circ)} \\ \sqrt{0.5625}e^{i(-0.07^\circ)} \end{pmatrix}. \tag{3.9}$$

Generally, the time evolutions of each spin components are periodic oscillations, similar to a two-level system with coupling. The population evolution of the pulse is plotted in Fig. 3.1.

3.2 Interacting Spinor Gases

3.2.1 The form of two-body interaction

In this section we derive the form of interaction between two particles with spin-1, spin-2 from the same or different atomic species. We denote the individual spin of two colliding particle as $\mathbf{F}_1$ and $\mathbf{F}_2$, and the total spin of the $\mathbf{F} = \mathbf{F}_1 + \mathbf{F}_2$.
In the system of ultracold dilute atomic gases, it it usually sufficient to consider only the two-body interaction [86], and collisions between two particles of the same atomic species are characterized simply by the s-wave scattering lengths in different total spin channel [35, 36, 87]:

$$V = \delta\left(\mathbf{x} - \mathbf{x}'\right) \sum_{F=0}^{2f} g_F P_F, \tag{3.10}$$

where $g_F = 4\pi\hbar^2 a_F / M$, M is the atomic mass, $P_F = \sum_{m_F=-F}^{F} \left|F, m_F\right\rangle \left\langle F, m_F\right|$ is the projection operator which project the state into the total spin F state, a_F is the s-wave scattering of the total spin F channel. The allowed values are the even F for identical bosons due to symmetry requirement.
Now we want to rewrite the interaction in terms of the operator for individual particles. From the algebra of angular momentum we have the relations:

$$\begin{aligned}
1 &= P_0 + P_2 \\
\mathbf{F}_1 \cdot \mathbf{F}_2 = \left(\mathbf{F}_1 + \mathbf{F}_2\right)^2 &= \frac{1}{2}\left(\mathbf{F}^2 - \mathbf{F}_1^2 - \mathbf{F}_2^2\right) \\
&= \frac{1}{2}\left(\mathbf{F}^2 - \mathbf{F}_1^2 - \mathbf{F}_2^2\right)\left(P_0 + P_2\right) \\
&= \frac{1}{2}\left(\mathbf{F}^2 - 4\right)\left(P_0 + P_2\right) \\
&= -2P_0 + P_2.
\end{aligned}$$

So $P_0 = \frac{1-\mathbf{F}_1\cdot\mathbf{F}_2}{3}, P_2 = \frac{2+\mathbf{F}_1\cdot\mathbf{F}_2}{3}$ and we have (dropping the δ-function)

$$V = g_0P_0 + g_2P_2 = \frac{g_0+2g_2}{3} + \frac{g_2-g_0}{3}\mathbf{F}_1\cdot\mathbf{F}_2 = c_0 + c_2\mathbf{F}_1\cdot\mathbf{F}_2, \tag{3.11}$$

where $c_0 = \frac{4\pi\hbar^2(a_0+2a_2)}{3M}, c_2 = \frac{4\pi\hbar^2(a_2-a_0)}{3M}$. Similarly we can derive the interactions for other systems. For two spin-2 particles of the same species, the angular momentum relations become

$$\begin{aligned} 1 &= P_0 + P_2 + P_4 \\ \mathbf{F}_1\cdot\mathbf{F}_2 &= \frac{1}{2}\left(\mathbf{F}^2 - 12\right)(P_0+P_2+P_4) = -6P_0 - 3P_2 + 4P_4. \end{aligned}$$

Hence $P_2 = \frac{4-\mathbf{F}_1\cdot\mathbf{F}_2-10P_0}{7}, P_4 = \frac{3+\mathbf{F}_1\cdot\mathbf{F}_2+3P_0}{7}$ and

$$\begin{aligned} V &= g_0P_0 + g_2P_2 + g_4P_4 \\ &= \frac{4g_2+3g_4}{7} + \frac{g_4-g_2}{7}\mathbf{F}_1\cdot\mathbf{F}_2 + \frac{7g_0-10g_2+3g_4}{7}P_0 \\ &= c_0 + c_1\mathbf{F}_1\cdot\mathbf{F}_2 + c_2P_0, \end{aligned} \tag{3.12}$$

where $c_0 = \frac{4\pi\hbar^2(4a_2+3a_4)}{7M}, c_1 = \frac{4\pi\hbar^2(a_4-a_2)}{7M}, c_2 = \frac{4\pi\hbar^2(7a_0-10a_2+3a_4)}{7M}$. Note that the singlet pairing term is present in the expression.

For two spin-1 particle of different atomic species with mass M_1 and M_2, since they are distinguishable, the allowed total spin can take all odd and even values. The mass M in the interspecies interaction strength g_F should be replaced by reduced mass $\mu = \frac{M_1M_2}{M_1+M_2}$ in this case,

$$\begin{aligned} 1 &= P_0 + P_1 + P_2 \\ \mathbf{F}_1\cdot\mathbf{F}_2 &= -2P_0 - P_1 + P_2, \end{aligned}$$

So $P_1 = \frac{1-\mathbf{F}_1\cdot\mathbf{F}_2-3P_0}{2}$, $P_2 = \frac{1+\mathbf{F}_1\cdot\mathbf{F}_2+P_0}{2}$ and

$$\begin{aligned} V &= g_0P_0 + g_1P_1 + g_2P_2 \\ &= \frac{g_1+g_2}{2} + \frac{g_2-g_1}{2}\mathbf{F}_1\cdot\mathbf{F}_2 + \frac{2g_0-3g_1+g_2}{2}P_0 \\ &= \alpha + \beta\mathbf{F}_1\cdot\mathbf{F}_2 + \gamma P_0, \end{aligned} \tag{3.13}$$

where $\alpha = \frac{4\pi\hbar^2(a_1+a_2)}{2\mu}, \beta = \frac{4\pi\hbar^2(a_2-a_1)}{2\mu}, \gamma = \frac{4\pi\hbar^2(2a_0-3a_1+a_2)}{2\mu}$.

It should be noticed that there are also other types of interaction that are not necessarily of the form in (3.10). For example, the dipolar interaction has the form $V = c_{dd}\frac{\mathbf{F}_1\cdot\mathbf{F}_2-3(3\mathbf{F}_1\cdot\mathbf{r}/r)(3\mathbf{F}_1\cdot\mathbf{r}/r)}{r^3}$ which is a long-range interaction [88]. Although the typical effect is small and negligible under usual experimental conditions, it is shown that the dipolar interaction can have contributions to the formation of spin texture or modify spin dynamics [54, 89]. In this thesis we do not take into account these interactions.

3.2.2 Second Quantization Formalism

An atomic cloud with spin degree of freedom is in essence a many-body system, hence the theoretical tool for calculating the properties of this system is second quantization. The starting point is to write down the two-body interaction explicitly.

The most general form of the Hamiltonian for a many-body system with two-body interaction for every two particles has already given by Eq. 2.43. For a particle with spin, the Hilbert space becomes a direct product space of coordinate and spin, the index $s = (\mathbf{x}, \sigma)$ and the field operator $a_s = a_{\mathbf{x},\sigma} = \psi_\sigma(\mathbf{x})$. The summation is replaced by $\sum\limits_{rs} = \iint d\mathbf{x}d\mathbf{x}' \sum\limits_{\sigma\sigma'}$ and the matrix element of an one-body operator is

$$\begin{aligned}\langle r|T|s\rangle &= \langle \mathbf{x},\sigma|T|\mathbf{x}',\sigma'\rangle = \delta\left(\mathbf{x}-\mathbf{x}'\right)\langle\sigma|T(\mathbf{x})|\sigma'\rangle = \delta\left(\mathbf{x}-\mathbf{x}'\right)T_{\sigma\sigma'}(\mathbf{x})\\ &= \delta\left(\mathbf{x}-\mathbf{x}'\right)\left(\delta_{\sigma\sigma'}A(\mathbf{x})+\delta_{\sigma\sigma'}B_{\sigma}(\mathbf{x})+C_{\sigma\sigma'}(\mathbf{x})\right).\end{aligned}$$

Here we distinguish three different types of operators: A is spin-independent (e.g., kinetic energy, trapping potential), B is spin-dependent but only has diagonal elements (e.g., linear and quadratic Zeeman shift), C is spin-dependent and has coupling between different spin components (e.g., microwave field).
Similarly the matrix element of a two-body operator is

$$\begin{aligned}\langle rs|V|tu\rangle &= \langle \mathbf{x}\sigma\mathbf{x}'\sigma'|V|\mathbf{y}\upsilon\mathbf{y}'\upsilon'\rangle = \delta\left(\mathbf{x}-\mathbf{y}\right)\delta\left(\mathbf{x}'-\mathbf{y}'\right)\langle\mathbf{x}\sigma\mathbf{x}'\sigma'|V|\mathbf{x}\upsilon\mathbf{x}'\upsilon'\rangle\\ &= \delta\left(\mathbf{x}-\mathbf{y}\right)\delta\left(\mathbf{x}'-\mathbf{y}'\right)\langle\sigma\sigma'|V(\mathbf{x},\mathbf{x}')|\upsilon\upsilon'\rangle.\end{aligned}$$

So the general form of a second quantized Hamiltonian with spin-dependent interaction is

$$\begin{aligned}H = &\int d\mathbf{x}\left(\sum_{\sigma}\psi^{\dagger}_{\sigma}(\mathbf{x})\left(A(\mathbf{x})+B_{\sigma}(\mathbf{x})\right)\psi_{\sigma}(\mathbf{x})+\sum_{\sigma\sigma'}\psi^{\dagger}_{\sigma}(\mathbf{x})C_{\sigma\sigma'}(\mathbf{x})\psi_{\sigma'}(\mathbf{x})\right)\\ &+\frac{1}{2}\iint d\mathbf{x}d\mathbf{x}'\sum_{\sigma\sigma'\upsilon\upsilon'}\psi^{\dagger}_{\sigma}(\mathbf{x})\psi^{\dagger}_{\sigma'}(\mathbf{x}')\langle\sigma\sigma'|V(\mathbf{x},\mathbf{x}')|\upsilon\upsilon'\rangle\psi_{\upsilon'}(\mathbf{x}')\psi_{\upsilon}(\mathbf{x}).\end{aligned}\tag{3.14}$$

For a spin-1 system, we have

$$\begin{aligned}\langle\sigma\sigma'|V(\mathbf{x},\mathbf{x}')|\upsilon\upsilon'\rangle &= \delta\left(\mathbf{x}-\mathbf{x}'\right)\langle\sigma\sigma'|\left(c_0+c_2\mathbf{F}_1\cdot\mathbf{F}_2\right)|\upsilon\upsilon'\rangle\\ &= \delta\left(\mathbf{x}-\mathbf{x}'\right)\left(\delta_{\sigma\upsilon}\delta_{\sigma'\upsilon'}c_0+c_2\langle\sigma|\mathbf{F}_1|\upsilon\rangle\cdot\langle\sigma'|\mathbf{F}_2|\upsilon'\rangle\right)\\ &= \delta\left(\mathbf{x}-\mathbf{x}'\right)\left(\delta_{\sigma\upsilon}\delta_{\sigma'\upsilon'}c_0+c_2\mathbf{F}_{\sigma\upsilon}\cdot\mathbf{F}_{\sigma'\upsilon'}\right).\end{aligned}\tag{3.15}$$

Finally,

$$\begin{aligned} H = & \int d\mathbf{x} \sum_{\sigma} \psi_{\sigma}^{\dagger}(\mathbf{x}) \left(-\frac{\hbar^2}{2m} \nabla^2 + U(\mathbf{x}) + E_{\sigma}(\mathbf{x}) \right) \psi_{\sigma}(\mathbf{x}) \\ & + \int d\mathbf{x} \sum_{\sigma\sigma'} \psi_{\sigma}^{\dagger}(\mathbf{x}) C_{\sigma\sigma'}(\mathbf{x}) \psi_{\sigma}(\mathbf{x}) \\ & + \frac{c_0}{2} \int d\mathbf{x} \sum_{\sigma\sigma'} \psi_{\sigma}^{\dagger}(\mathbf{x}) \psi_{\sigma'}^{\dagger}(\mathbf{x}) \psi_{\sigma'}(\mathbf{x}) \psi_{\sigma}(\mathbf{x}) \\ & + \frac{c_2}{2} \int d\mathbf{x} \sum_{\sigma\sigma' v v'} \psi_{\sigma}^{\dagger}(\mathbf{x}) \psi_{\sigma'}^{\dagger}(\mathbf{x}) \mathbf{F}_{\sigma v} \cdot \mathbf{F}_{\sigma' v'} \psi_{v'}(\mathbf{x}) \psi_{v}(\mathbf{x}). \end{aligned} \tag{3.16}$$

3.2.3 Single-Mode and Mean-Field Approximation

The Hamiltonian (3.16) can be a starting point to calculate the properties of the system. A few approximations can be applied, including the single-mode approximation (SMA) and mean-field approximation. These are two independent approximations and should be distinguished. In principle, we can adopt either or both approximation according to the systems and observables involved.

The SMA is to separate the spin and spatial part of the system. Specifically the field operator is written as $\hat{\psi}_{\sigma}(\mathbf{x}) = \hat{\xi}_{\sigma}\hat{\phi}(\mathbf{x})$, with $\hat{\xi}_{\sigma}$ the annihilation operator for the particle with spin σ component, $\hat{\phi}(\mathbf{x})$ the annihilation operator for the particle at $\mathbf{x}$. The SMA is usually valid when the system's size is smaller than the spin healing length, which is defined by $\xi_{sp} = [8\pi n (a_2 - a_0)]^{-1/2}$ for spin-1 case.

The mean-field approximation is to neglect the fluctuation and replace the operator by its mean value. Specifically the field operator is written as $\hat{\psi}_{\sigma}(\mathbf{x}) = \left\langle \hat{\psi}_{\sigma}(\mathbf{x}) \right\rangle \equiv \psi_{\sigma}(\mathbf{x})$.

When both approximation are adopted, the the field operator is replaced by $\hat{\psi}_{\sigma}(\mathbf{x}) = \psi_{\sigma}(\mathbf{x}) = \xi_{\sigma}\phi(\mathbf{x})$, where $\phi(\mathbf{x})$ can be shown to be the ground state wave function of the BEC, hence the order parameter of the system is $\phi(\mathbf{x})(\xi_{-1}, \xi_0, \xi_1) = \phi(\mathbf{x})\vec{\xi}$, in which $\vec{\xi}$ is called a "spinor". The mean-field SMA dynamics is the main subject of this thesis. Under these approximations the Hamiltonian (3.16) becomes the mean field energy functional

$$\begin{aligned}
E &= \int d\mathbf{x} \left(\frac{\hbar^2}{2m} |\nabla\phi(\mathbf{x})|^2 + U(\mathbf{x}) |\phi(\mathbf{x})|^2 \right) \\
&\quad + \int d\mathbf{x} \left(p \langle F_z \rangle |\phi(\mathbf{x})|^2 + q \left\langle F_z^2 \right\rangle |\phi(\mathbf{x})|^2 \right) \\
&\quad + \int d\mathbf{x} \left(\frac{c_0}{2} |\phi(\mathbf{x})|^4 + \frac{c_2}{2} |\phi(\mathbf{x})|^4 \langle \mathbf{F} \rangle^2 \right) \\
&= \int d\mathbf{x} \frac{\hbar^2}{2m} |\nabla\phi(\mathbf{x})|^2 + NU(\mathbf{x}) + N \frac{c_0 n}{2} \\
&\quad + N \left(p \langle F_z \rangle + q \left\langle F_z^2 \right\rangle + \frac{c_2 n}{2} \langle \mathbf{F} \rangle^2 \right),
\end{aligned} \tag{3.17}$$

where the average $\langle O \rangle = \sum_{\sigma\sigma'} \xi_\sigma^* O_{\sigma\sigma'} \xi_{\sigma'}$, $N = \int d\mathbf{x} |\phi(\mathbf{x})|^2$ is the particle number, $n = \int d\mathbf{x} |\phi(\mathbf{x})|^4 / N$ is the average number density.

It should be noted that the two approximation are not always adopted. When we adopt the SMA and make the mean-field approximation only for the spatial part, then the spin part is treated in terms of field operators and the exact many-body ground state and dynamics can be calculated for spins. This was done in [57] in 1998. Another example is the study of parametric amplification of vacuum fluctuation in spinor condensate [52], in which both approximations are not adopted, but the field operator is decomposed into a mean field plus fluctuations, the latter being a superposition of mode functions and field operators for spin.

3.2.4 Static and Dynamic Properties

Ground state

From the mean field energy functional (3.17) we can calculate the ground state, collective excitations and dynamics of the spinor BEC under SMA and mean field approximation. The ground state is found by minimizing the energy functional. Since $c_2 \ll c_0$, it is clear from (3.17) that the dependence of energy on spatial wave function is not affected by the spin-dependent part hence the spatial wavefunction is the same with scalar BEC (e.g., Thomas-Fermi density profile). The next step is to minimize the spin-dependent part

$$H_s = -p \langle F_z \rangle + q \left\langle F_z^2 \right\rangle + \frac{c_2 n}{2} \langle \mathbf{F} \rangle^2. \tag{3.18}$$

However, from the Hamiltonian (3.16) we can write down each term in the interaction explicitly and find that there only exist the spin changing process $|m_F = 1\rangle + |m_F = 2\rangle \leftrightarrow 2\,|m_F = 0\rangle$, hence the interaction conserves the longitudinal magnetization $\langle F_z \rangle$. Therefore, the minimization of the energy functional should under the constraint of constant magnetization, i.e., the ground state is the spinor minimizing $H_s - p_0 \langle F_z \rangle$, where p_0 is the Lagrangian multiplier to be determined [34]. Another constraint is the normalization of the spinor wavefunction, or equivalently the total atom number to be N. In summary, the ground state problem is to find the spinor to minimize the quantity

$$\begin{aligned} H' &= H_s - p_0 \langle F_z \rangle - \mu \left(|\xi_{-1}|^2 + |\xi_0|^2 + |\xi_1|^2 \right) \\ &= -\tilde{p} \langle F_z \rangle + q \left\langle F_z^2 \right\rangle + \frac{c_2 n}{2} \langle \mathbf{F} \rangle^2 - \mu \left(|\xi_{-1}|^2 + |\xi_0|^2 + |\xi_1|^2 \right), \end{aligned} \tag{3.19}$$

where $\tilde{p} = p + p_0$. Writing down explicitly,

$$\begin{aligned} H' = {} & -\tilde{p} \left(\xi_1 \xi_1^* - \xi_{-1} \xi_{-1}^* \right) + q \left(\xi_1 \xi_1^* + \xi_{-1} \xi_{-1}^* \right) + \frac{c_2 n}{2} \Big(\xi_1^2 \xi_1^{*2} \\ & + \xi_{-1}^2 \xi_{-1}^{*2} + 2 \xi_1 \xi_{-1} \xi_0^{*2} + 2 \xi_0^2 \xi_1^* \xi_{-1}^* - 2 \xi_1 \xi_{-1} \xi_1^* \xi_{-1}^* \\ & + 2 \xi_0 \xi_0^* \xi_{-1} \xi_{-1}^* + 2 \xi_0 \xi_0^* \xi_1 \xi_1^* \Big) - \mu \left(\xi_1 \xi_1^* + \xi_0 \xi_0^* + \xi_{-1} \xi_{-1}^* \right). \end{aligned} \tag{3.20}$$

Since each component of the spinor has a real and imaginary part, the problem is an extremal problem of a function with six variables and two constraints. The eight equations to determine the extremum are

$$\begin{aligned} \frac{\partial H'}{\partial \xi_\sigma^*} &= 0, (\sigma = -1, 0, 1) \\ (\xi_\sigma^*)^* &= \xi_\sigma, (\sigma = -1, 0, 1) \\ f_z &= \xi_1 \xi_1^* - \xi_{-1}\xi_{-1}^* \\ 1 &= \xi_1\xi_1^* + \xi_0\xi_0^* + \xi_{-1}\xi_{-1}^*, \end{aligned} \tag{3.21}$$

where f_z is a designated longitudinal magnetization. Choosing the phase of 0 component to be zero, the first line of the above equations are explicitly

$$\begin{aligned} c_2 n \xi_0 \left(\xi_1 + \xi_{-1}^*\right) + \xi_1 \left(-\tilde{p} + q + c_2 n f_z - \mu\right) &= 0 \\ \xi_0 \left[c_2 n \left(2\xi_1\xi_{-1} + \xi_{-1}\xi_{-1}^* + \xi_1\xi_1^*\right) - \mu\right] &= 0 \\ c_2 n \xi_0 \left(\xi_1^* + \xi_{-1}\right) + \xi_{-1}\left(\tilde{p} + q - c_2 n f_z - \mu\right) &= 0. \end{aligned} \tag{3.22}$$

The solution of the above equations can be classified into five groups according to the form of the energy [55]:

(1) (Longitudinal ferromagnetic state)

$$\left(e^{i\theta_1}, 0, 0\right)^T$$

$$f_z = 1, E = -\tilde{p} + q + \frac{c_2 n}{2}$$

(2) (Longitudinal ferromagnetic state)

$$\left(0, 0, e^{i\theta_{-1}}\right)^T$$

$$f_z = -1, E = \tilde{p} + q + \frac{c_2 n}{2}$$

(3) (State with partial longitudinal magnetization)

$$\left(e^{i\theta_1}\sqrt{\frac{1}{2}\left(1+\frac{\tilde{p}}{c_2 n}\right)}, 0, e^{i\theta_{-1}}\sqrt{\frac{1}{2}\left(1-\frac{\tilde{p}}{c_2 n}\right)}\right)^T$$

$$f_z = \frac{\tilde{p}}{c_2 n}, E = q - \frac{\tilde{p}^2}{2c_2 n}$$

(4) (Longitudinal polar state)

$$\left(0, e^{i\theta_0}, 0\right)^T$$

$$f_z = 0, E = 0$$

(5) (Broken-axisymmetry state)

$$\begin{pmatrix} e^{i(\theta_0+\theta)}\frac{q+\tilde{p}}{2q}\sqrt{\frac{-\tilde{p}^2+q^2+2c_2nq}{2c_2nq}} \\ e^{i\theta_0}\sqrt{\frac{(q^2-\tilde{p}^2)(-\tilde{p}^2-q^2+2c_2nq)}{4c_2nq^3}} \\ e^{i(\theta_0-\theta)}\frac{q-\tilde{p}}{2q}\sqrt{\frac{-\tilde{p}^2+q^2+2c_2nq}{2c_2nq}} \end{pmatrix}$$

$$f_z = \frac{\tilde{p}\left(-\tilde{p}^2+q^2+2c_2nq\right)}{2c_2nq^2}, E = \frac{\left(-\tilde{p}^2+q^2+2c_2nq\right)^2}{8c_2nq^2}$$

The phase diagram, in which the ground state is determined at each point in the $(p/|c_2|n, q/|c_2|n)$ parameter space, for $c_2 > 0$,$c_2 = 0$ and $c_2 < 0$ are plotted in Fig. 3.2.

In the above ground state classification and phase diagram, the parameter is q and $\tilde{p}$. However $\tilde{p}$ is not a designated number but a Langrangian multiplier needed to determined during the minimization. Thus, For designated magnetization f_z, one need to calculate $\tilde{p}$ according to the magnetization of each phase and determine the corresponding point in the phase diagram. Thus the phase diagram is not depend on f_z explicitly. In another point of view, if the constraint of magnetization conservation is not required, $\tilde{p}$ is purely the linear Zeeman shift, and the phase diagram can be viewed as the global phase diagram without con-

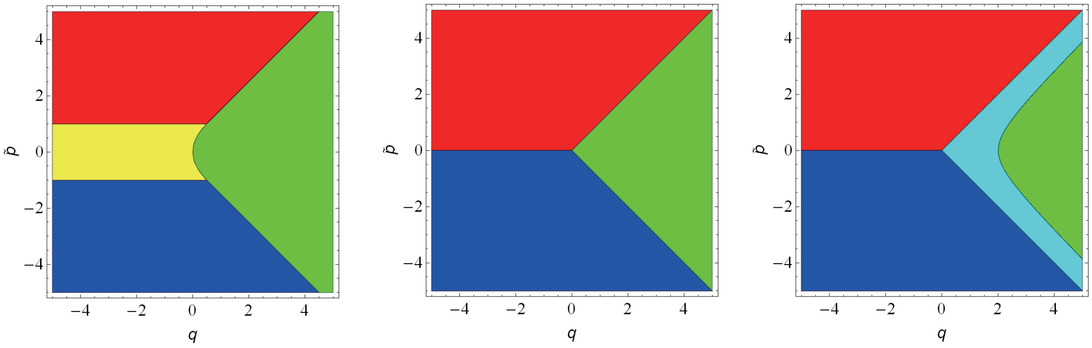

Figure 3.2: Ground state phase diagram of $F = 1$ spinor gases. In the $(p/|c_2|n, q/|c_2|n)$ parameter space, different colors represent different phases of the ground state which minimize the energy (3.18): Red, blue, yellow, green, cyan for state (1), (2), (3), (4), (5) respectively. (a) Antiferromagnetic interaction ($c_2 > 0$); (b) No interaction ($c_2 = 0$); (c) Ferromagnetic interaction ($c_2 < 0$).

straint. It can be used to discuss systems that the magnetization need not to be conserved (e.g., in some atomic species such as Cr [90]), or the ground state realized by magnetization non-conserving evaporation process.

A more practical approach is to contains f_z explicitly in minimizing the energy [91]. (3.18) can be rewritten as

$$E = -pm + \frac{c_2 nm}{2} + q\left(1-\rho\right) + c_2 n\rho\left(1-\rho+\sqrt{\left(1-\rho\right)^2 - m^2}\cos\theta\right), \quad (3.23)$$

where $\rho_\sigma = \xi_\sigma \xi_\sigma^*$, $\rho = \rho_0$, $m = f_z = \rho_1 - \rho_{-1}$. Now the ground state is obtained by minimizing E under the constraints $0 \le \rho \le 1$, $-1 \le m \le 1$ and $\rho - 1 \le m \le 1 - \rho$. The results are summarized as follows:

(1) $\boldsymbol{c_2 = 0}$:

(a) $q > 0$:

$$\rho = 1 - |m|, \rho_1 = \begin{cases} |m|, & m \ge 0 \\ 0, & m < 0 \end{cases}, \rho_{-1} = \begin{cases} 0, & m \ge 0 \\ |m|, & m < 0 \end{cases}$$

(b) $q = 0$:

$$0 \leq \rho \leq 1 - |m|\,, \rho_{\pm 1} = (1 - \rho \pm m)/2$$

(2) $c_2 < 0$:

(a) $q = 0$:

$$\rho = 1 - m^2, \rho_{\pm 1} = (1 \pm m)^2/4$$

(b) $q > 0$:

$$\rho = 1 - x, \rho_{\pm 1} = (x \pm m)/2$$

where x is the solution of $d\left[2c_2 n\left(1 - x\right)\left(x + \sqrt{x^2 - m^2}\right) + qx\right]/dx = 0$.

(3) $c_2 > 0$:

(a) $q = 0, m = 0$:

$$\rho_1 = \rho_{-1} = (1 - \rho)/2, \quad \rho \text{ undetermined}$$

(b) $q = 0, m \neq 0$:

$$\rho = 0, \rho_{\pm 1} = (1 \pm m)/2$$

(c) $q > 0, m = 0$:

$$\rho = 1, \rho_{\pm 1} = 0$$

(d) $0 < q \leq 2c_2 n\left(1 - \sqrt{1 - m^2}\right), m \neq 0$:

$$\rho = 0, \rho_{\pm 1} = (1 \pm m)/2$$

(e) $q > 2c_2 n\left(1 - \sqrt{1 - m^2}\right), m \neq 0$:

$$\rho = 1 - x, \rho_{\pm 1} = (x \pm m)/2$$

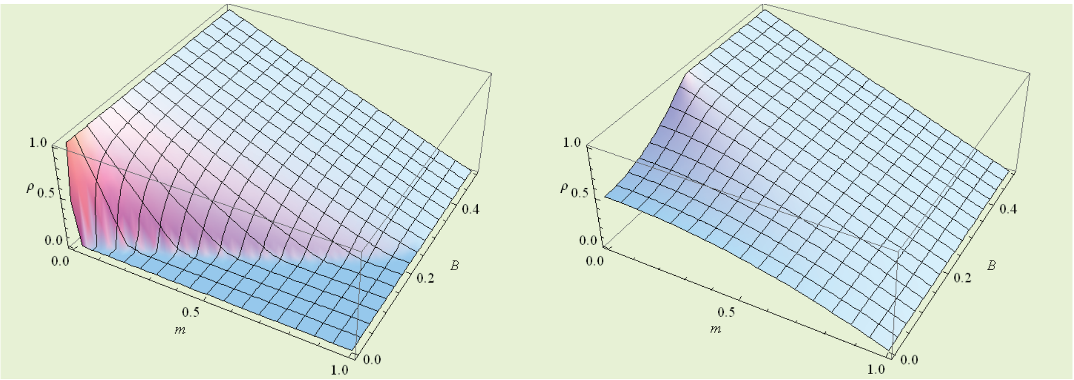

Figure 3.3: Ground state with explicit m dependence. The $|0\rangle$ population as a function of the longitudinal magnetization m and magnetic field B are plotted, for typical experimental condition of antiferromagnetic Na ($c_2 > 0$, left) and ferromagnetic Rb ($c_2 < 0$, right).

where x is the solution of $d\left[2c_2 n\left(1-x\right)\left(x-\sqrt{x^2-m^2}\right)+qx\right]/dx=0$.

The dependence of the ground state populations of $|0\rangle$ on the longitudinal magnetization m and magnetic field B are plotted in Fig. 3.3, for typical experimental condition of Na (antiferromagnetic) and Rb (ferromagnetic).

Dynamics

After figuring out the ground states of the system, we can study the dynamics by preparing the initial state which is not the ground state, and trace the evolution of the system.

There are several methods to derive the dynamical equations for the spinor. One general method is the variational approach. Under SMA, we can use (3.18) as the spin-dependent energy functional, and the dynamical equations are given by

$$i\hbar\frac{\partial\xi_m}{\partial t}=\frac{\delta E}{\delta\xi_m^*}. \tag{3.24}$$

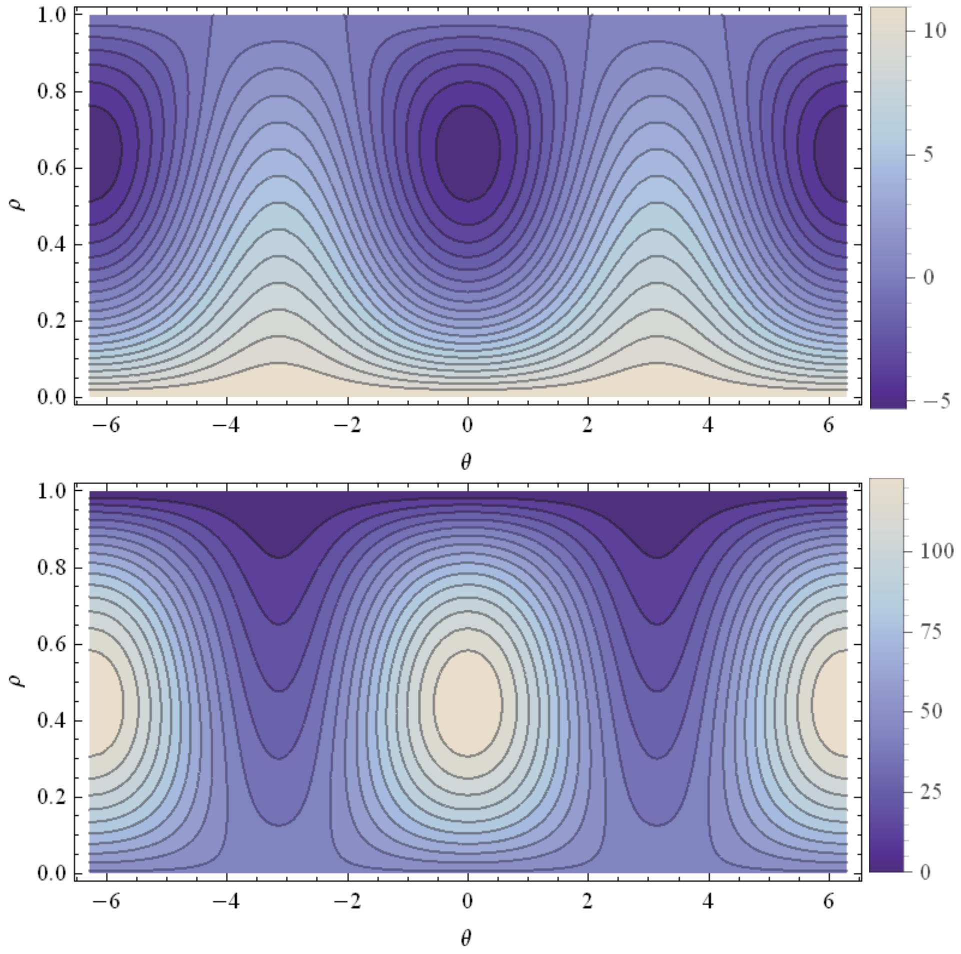

Figure 3.4: Mean field energy contour of Rb (upper pannel) and Na (lower pannel). The ground state corresponds to the lowest point in the plot. The dynamics of a system initial not in ground state can be represented by the contours, due to energy conservation. Note that there are two kinds of trajectories: open running ones and closed cycling ones. The resonance of the dyanmics corresponds to the seperatrix of these two trajectories.

Written down explicitly,

$$\begin{aligned} i\hbar\frac{\partial\xi_1}{\partial t} &= \left[-p+q+c_2n\left(\rho_1+\rho_0-\rho_{-1}\right)\right]\xi_1+\xi_0^2\xi_{-1}^* \\ i\hbar\frac{\partial\xi_0}{\partial t} &= c_2n\left(\rho_1+\rho_{-1}\right)\xi_1+2c_2n\xi_1\xi_{-1}\xi_0^* \\ i\hbar\frac{\partial\xi_{-1}}{\partial t} &= \left[p+q+c_2n\left(\rho_{-1}+\rho_0-\rho_1\right)\right]\xi_{-1}+\xi_0^2\xi_1^*. \end{aligned} \tag{3.25}$$

Note that if SMA is not adopted, the mean field energy functional should include the spatial dependence. In this case ξ_m is replaced by $\phi_m(\mathbf{x})$ in (3.24), and (3.25) becomes a multicomponent GP equation.

(3.25) can be further simplified to

$$\begin{aligned} \frac{d\rho}{dt} &= \frac{2c_2n}{\hbar}\rho\sqrt{\left(1-\rho\right)^2-m^2}\sin\theta \\ \frac{d\theta}{dt} &= -\frac{2q}{\hbar}+\frac{2c_2n}{\hbar}\left[\left(1-2\rho\right)+\frac{\left(1-\rho\right)\left(1-2\rho\right)-m^2}{\sqrt{\left(1-\rho\right)^2-m^2}}\cos\theta\right], \end{aligned} \tag{3.26}$$

where $\rho=\rho_0$, $\theta=\theta_1+\theta_{-1}-2\theta_0$. These equations can be viewed as a set of canonical equations $\dot{\rho}=-\left(2/\hbar\right)\partial E/\partial\theta$ and $\dot{\theta}=\left(2/\hbar\right)\partial E/\partial\rho$, where the energy is given by (3.18). The resulting dynamics of (3.26) is generally an oscillation of ρ and θ, hence the population of the three component transfer back and forth, while the magnetization m is kept constant. The analytical solutions and the exact form of period and amplitude have been studied [92]. Here we give a brief summary.

(1) When $q \ll c_2n$, the interaction energy dominates, the period of the oscillation $T=\pi\hbar/c_2n$, and the amplitude $A\propto q/c_2n$. It is called the interaction regime, and the dynamics corresponds to the closed circler trajectories in the phase space.

(2) When $q \gg c_2n$, the quadratic Zeeman energy dominates, the period of the oscillation $T=\pi\hbar/q$, and the amplitude $A\propto c_2n/q$. It is called the Zeeman regime, and the dynamics corresponds to the open running trajectories in the phase space.

(3) When q is comparable with $c_2 n$, the dynamics is slowed. For the initial state with $\rho(0) = 1/2$ which is widely used in experiments, and analytical expression is given by $\rho = \left(1 - (c_2 n/q)\,\mathrm{sn}_k^2\,(qt/\hbar)\right)/2$. The oscillation reaches a resonance at $q = c_2 n$ for $m = 0$, where the period diverges. This correspond to a separatrix between the closed and open trajectories in the phase space, similar to the simple pendulum, in which the separatrix between the two kind of trajectories represent the pendulum stopped at the highest point, and distinct the motions of oscillation and rotation.

3.2.5 Beyond Mean-Field and SMA

We have discussed the ground state and dynamics under SMA and mean field approximation. However, theories on spinor gases beyond these two approximations have been studies extensively, not only because in many cases they are not applicable to account for the experimental observations, but also because this system are promising to observe the effects predicted by more precise theories. In this section we present some of these knowledge accumulated so far.

First, within SMA and make the mean field approximation only for the spatial part $\hat{\psi}_\sigma(\mathbf{x}) = \hat{a}_\sigma \phi(\mathbf{x})$, one can treat the spin part of this system in an exact many-body way. Furthermore, let $\hat{N} = \hat{a}_1^\dagger \hat{a}_1 + \hat{a}_0^\dagger \hat{a}_0 + \hat{a}_{-1}^\dagger \hat{a}_{-1}$, $\hat{L}_z = \hat{a}_{-1}^\dagger \hat{a}_{-1} - \hat{a}_1^\dagger \hat{a}_1$, $\hat{L}_+ = \sqrt{2}\left(\hat{a}_0^\dagger \hat{a}_1 - \hat{a}_{-1}^\dagger \hat{a}_0\right)$ and $\hat{L}_- = \sqrt{2}\left(\hat{a}_1^\dagger \hat{a}_0 - \hat{a}_0^\dagger \hat{a}_{-1}\right)$, the Hamiltonian (3.16) in zero magnetic field becomes [57]

$$H = \mu \hat{N} - \lambda_0 \hat{N}\left(\hat{N} - 1\right) + \lambda_2\left(\hat{L}^2 - 2\hat{N}\right), \tag{3.27}$$

where $\lambda_i = N c_i n/2$, μ is the chemical potential determined by $\phi(\mathbf{x})$ satisfying the spin-independent GP equation. This form implies that the original Hamiltonian can be diagonalized using the number operator and effective angular momentum operators. The resulting eigenstates are simply the simultaneous eigenstates of $\hat{N}$

and $\hat{L}^2$, denoted by $|l, m_l\rangle$, which is a superposition of Fock states $|n_1, n_0, n_{-1}\rangle$. For $\lambda_2 < 0$, the ground state is given by $|l = N, m_l\rangle$, which is $(2m_l + 1)$-fold degenerate. This state is found to have narrow distribution on the Fock states hence the atom numbers in each components are well defined, and the number fluctuations are sub-Poissonian.

A striking different ground state from mean field theory is when $\lambda_2 < 0$. In this case the ground state is given by $|l = 0, m_l = 0\rangle = \sum_{k=0}^{[N/2]} A_k |k, N - 2k, k\rangle$, where A_k has a broad distribution over the Fock states. The expectation value of atom number in each component are $\left\langle \hat{a}_1^\dagger \hat{a}_1 \right\rangle = \left\langle \hat{a}_0^\dagger \hat{a}_0 \right\rangle = \left\langle \hat{a}_{-1}^\dagger \hat{a}_{-1} \right\rangle = N/3$, and the number fluctuation is very large, e.g., $\langle \Delta \hat{n}_0 \rangle \approx 2N/\sqrt{5}$. The unique feature of this state is that it is a state with all atoms form singlet pairs. It can be shown that the state can also be written as $A\left(\hat{S}^\dagger\right)^{N/2} |vac\rangle$ [93], where $\hat{S}^\dagger = 2\left(\hat{a}_0^\dagger\right)^2 - \hat{a}_1^\dagger \hat{a}_{-1}^\dagger$ creates a singlet pair, $|vac\rangle$ is a state with no particles, A is a normalization constant. Another feature is that it is a fragmented state, which means that the condensate cannot be viewed as all atoms condensed into a single particle state, but there are several states macroscopically occupied. A criteria for fragmentation is that the one-body density matrix $\left\langle \hat{a}_m^\dagger \hat{a}_{m'} \right\rangle$ contains several nonzero diagonal elements while the non-diagonal elements are zero. In contrast, for a mean field ground state, which can be written as a single particle state, $\left\langle \hat{a}_m^\dagger \hat{a}_{m'} \right\rangle$ can always be diagonalized to $\mathrm{Diag}\,[N, 0, 0]$.

The many-body dynamics of the system is also different from the mean field result. In mean field approximation, $|0, N, 0\rangle$ is a stationary state, while the many-body calculation predicts a decrease of the $|m_F = 0\rangle$ population, with a damping characterized by time scale $t_c = \hbar/2\lambda_2\sqrt{N}$. Note that this damping is not due to any energy dissipation but is a purely many-body effect. Other different features including the anharmonic oscillation and revival of the dynamics. However, the experimental confirmation is not yet been done since a BEC with small number under well control is needed.

Beyond SMA

A further question is if the SMA is not adopted, how will the system behave beyond mean-field approximation? The exact solution is of course difficult to find, but a "first-order" solution can be obtained by the Bogoliubov theory. It has been successfully used to demonstrate the dynamical instability and recently, account for the parametric amplification and spontaneous symmetry breaking in spinor BEC.

The main idea of this approach is to shift the field operator to a certain mean-field state and rewrite the field operator as a mean field plus a fluctuation operator, e.g., $\vec{\psi}\left(\mathbf{x}\right) = \left(0, \sqrt{n\left(\mathbf{x}\right)}, 0\right)^T + \left(\delta\psi_1\left(\mathbf{x}\right), \delta\psi_0\left(\mathbf{x}\right), \delta\psi_{-1}\left(\mathbf{x}\right)\right)^T$, then expand the Hamiltonian and keep the terms up to second order. Now the vacuum is given by the mean field state and the excitations can be found by diagonalizing the Hamiltonian in terms of the fluctuation operators.

In a uniform system, working in momentum space, $\vec{\psi}\left(\mathbf{x}\right) = \frac{1}{\sqrt{\Omega}}(0,1,0)^T + \frac{1}{\sqrt{\Omega}}\left(\sum\limits_{\mathbf{k}\neq 0} \hat{a}_{\mathbf{k},m} e^{i\mathbf{k}\cdot\mathbf{r}}, \sum\limits_{\mathbf{k}\neq 0} \hat{a}_{\mathbf{k},m} e^{i\mathbf{k}\cdot\mathbf{r}}, \sum\limits_{\mathbf{k}\neq 0} \hat{a}_{\mathbf{k},m} e^{i\mathbf{k}\cdot\mathbf{r}}\right)^T$, the Hamiltonian in a compact matrix form is given by [55]

$$\begin{aligned}\hat{H}_B = E_0 &+ \frac{1}{2}\sum_{\mathbf{k}\neq\mathbf{0}} \begin{pmatrix} \bar{\hat{\mathbf{a}}}_{\mathbf{k}}^{\dagger} & \bar{\hat{\mathbf{a}}}_{-\mathbf{k}} \end{pmatrix} \begin{pmatrix} \mathbf{H}_{\mathbf{k}}^{(\mathbf{0})} + \mathbf{H}^{(\mathbf{1})} & \mathbf{H}^{(\mathbf{2})} \\ \mathbf{H}^{(\mathbf{2})^*} & \left(\mathbf{H}_{-\mathbf{k}}^{(\mathbf{0})} + \mathbf{H}^{(\mathbf{1})}\right)^* \end{pmatrix} \begin{pmatrix} \hat{\mathbf{a}}_{\mathbf{k}} \\ \hat{\mathbf{a}}_{\mathbf{k}}^{\dagger} \end{pmatrix} \\ &- \frac{1}{2}\sum_{\mathbf{k}\neq\mathbf{0}} \left[Tr\left(\mathbf{H}_{\mathbf{k}}^{(\mathbf{0})} + \mathbf{H}^{(\mathbf{1})}\right) - \frac{D}{2\varepsilon_k}\right],\end{aligned} \tag{3.28}$$

where

$$
\begin{aligned}
\hat{\mathbf{a}}_{\mathbf{k}} &= \left(\hat{a}_{k,1}, \hat{a}_{k,0}, \hat{a}_{k,-1}\right)^T \\
\bar{\hat{\mathbf{a}}}_{\mathbf{k}} &= \left(\hat{a}_{k,1}, \hat{a}_{k,0}, \hat{a}_{k,-1}\right) \\
\mathbf{H}_{\mathbf{k}}^{(\mathbf{0})}+\mathbf{H}^{(\mathbf{1})} &= \begin{pmatrix} \varepsilon_k - p + q + c_2 n & 0 & 0 \\ 0 & \varepsilon_k + c_0 n & 0 \\ 0 & 0 & \varepsilon_k + p + q + c_2 n \end{pmatrix} \\
\mathbf{H}^{(\mathbf{2})} &= \begin{pmatrix} 0 & 0 & c_2 n \\ 0 & c_0 n & 0 \\ c_2 n & 0 & 0 \end{pmatrix} \\
E_0 &= N c_0 n/2 \\
D &= n^2 \left(c_0^2 + 2c_2^2\right).
\end{aligned}
$$

The Hamiltonian can be diagonalized to

$$
\hat{H}_B = E_0 + \frac{1}{2} \sum_{\mathbf{k} \neq \mathbf{0}} \left[Tr\left(\mathbf{E}_{\mathbf{k}} - \mathbf{H}_{\mathbf{k}}^{(\mathbf{0})} - \mathbf{H}^{(\mathbf{1})}\right) - \frac{D}{2\varepsilon_k} \right] + \sum_{\mathbf{k} \neq \mathbf{0}} E_{\mathbf{k},m} b_{\mathbf{k},m}^{\dagger} b_{\mathbf{k},m}, \tag{3.29}
$$

by Bogoliubov transformation

$$
\begin{aligned}
\hat{b}_{\mathbf{k},0} &= \operatorname{sgn}\left(c_0\right) \sqrt{\frac{\varepsilon_k + c_0 n + E_{\mathbf{k},0}}{2E_{\mathbf{k},0}}} \hat{a}_{\mathbf{k},0} + \sqrt{\frac{\varepsilon_k + c_0 n - E_{\mathbf{k},0}}{2E_{\mathbf{k},0}}} \hat{a}_{\mathbf{k},0}^{\dagger} \\
\hat{b}_{\mathbf{k},\pm1} &= \operatorname{sgn}\left(c_2\right) \sqrt{\frac{\varepsilon_k + q + c_2 n + \left(E_{\mathbf{k},\pm1} \pm p\right)}{2\left(E_{\mathbf{k},\pm1} \pm p\right)}} \hat{a}_{\mathbf{k},\pm1} \\
&\quad + \sqrt{\frac{\varepsilon_k + q + c_2 n - \left(E_{\mathbf{k},\pm1} \pm p\right)}{2\left(E_{\mathbf{k},\pm1} \pm p\right)}} \hat{a}_{-\mathbf{k},\mp1}^{\dagger}
\end{aligned} \tag{3.30}
$$

And the energy spectrum is

$$
\begin{aligned}
E_{\mathbf{k},0} &= \sqrt{\varepsilon_k \left(\varepsilon_k + 2c_0 n\right)} \\
E_{\mathbf{k},\pm1} &= \sqrt{\left(\varepsilon_k + q\right)\left(\varepsilon_k + q + 2c_2 n\right)} \mp p,
\end{aligned} \tag{3.31}
$$

$E_{\mathbf{k},0}$ and $E_{\mathbf{k},\pm1}$ represent density wave (phonon) and spin wave, repectively. In the case when the eigen energies are complex, the system is dynamically unstable, which means when we start in the vacuum (here is the polar state), the number of quasi-particles increases exponentially, and the time scale is given by $E_{\mathbf{k},m}/\hbar$. Eq. (3.31) can be used to explain the formation of magnetic domain in the experiment that quench q from above to below $2c_2n$ [40], in this way the the spin wave mode with $\varepsilon_k < 2\left|c_2\right|n - q$ become pure imaginary and $|\pm1\rangle$ populations grows with spatial periodicity corresponds to the wavelength of the mode. The effect of parametric amplification can also be investigated by the Bogoliubov theory [52, 55].

3.3 Mixture of Two-Species Spinor Gases

In this section we start to discuss the dynamics of a mixture of two atomic species with spin, which is a main subject of this thesis. The problem is in essence a many-body problem. But before going into the many-body formalism, we can get a prime picture and insight from a two-particle problem, which is further simplified to a two-level problem.

Two-Particle Problem

Let us consider two particles with one Rb atom and one Na atom, each has spin $F_{1,2} = 1$ and interaction of the form (3.13). Further, the system is prepared in a state with total angular momentum projection $M = -1$, so there exist only one kind of spin-changing collision $|-1_{\mathrm{Rb}}, 0_{\mathrm{Na}}\rangle \leftrightarrow |0_{\mathrm{Na}}, -1_{\mathrm{Rb}}\rangle$ due to magnetization conservation. Hence we can denote $|-1_{\mathrm{Rb}}, 0_{\mathrm{Na}}\rangle$ as state $|1\rangle$ and $|0_{\mathrm{Na}}, -1_{\mathrm{Rb}}\rangle$ as state $|2\rangle$. As the system becomes a two-level system, we would ask what are the bare energies and couplings. From Eq. (3.1), at an external magnetic field B, the Zeeman energy associated with the two state are $E_1\left(B\right) = p_{\mathrm{Rb}} + q_{\mathrm{Rb}}$, $E_2\left(B\right) =$

$p_{\mathrm{Na}} + q_{\mathrm{Na}}$, while the interaction of the two particles is given by

$$H_I = \sum_F U_F \left|F, M\right\rangle \left\langle F, M\right| = U_2 \left|2, -1\right\rangle \left\langle 2, -1\right| + U_1 \left|1, -1\right\rangle \left\langle 1, -1\right|, \tag{3.32}$$

where F is the total angular momentum which can only take 1 and 2, $U_F = \frac{4\pi\hbar^2 a_F}{\mu} \int |\psi|^2 |\phi|^2 d\mathbf{r}$ is the interaction energy in the F-channel, with $\psi(\mathbf{r})$ and $\phi(\mathbf{r})$ the spatial wavefunction of Rb and Na. Expressed in the two-level basis, according to the angular momentum coupling relation,

$$\begin{aligned} \left|2, -1\right\rangle &= \frac{1}{\sqrt{2}} \left(\left|1\right\rangle + \left|2\right\rangle\right) \\ \left|1, -1\right\rangle &= \frac{1}{\sqrt{2}} \left(-\left|1\right\rangle + \left|2\right\rangle\right). \end{aligned} \tag{3.33}$$

Hence

$$H_I = \frac{1}{2} \begin{pmatrix} U_2 + U_1 & U_2 - U_1 \\ U_2 - U_1 & U_2 + U_1 \end{pmatrix} \tag{3.34}$$

The total Hamiltonian is

$$H = \begin{pmatrix} E_1(B) + (U_2 + U_1)/2 & (U_2 - U_1)/2 \\ (U_2 - U_1)/2 & E_2(B) + (U_2 + U_1)/2 \end{pmatrix} \tag{3.35}$$

From this Hamiltonian we can see that the problem is similar to the usual two-level problem with the role of bare energies played by the Zeeman energy and interatomic interaction, while the coupling comes only from the interaction. We then expect the interation-driven Rabi oscillations with Rabi frequency

$$\Omega = \sqrt{\left(E_1(B) - E_2(B)\right)^2 + \left(U_2 - U_1\right)^2}/\hbar \tag{3.36}$$

This result predicts a maximum oscillation period at $E_1(B) - E_2(B) = 0$, or $B \approx 1.69$G, and decreasing period at two sides. The behavior of amplitude is similar. The prediction agrees well with experiment at two sides far from the resonant magnetic field, and in these regions the observed period is well approximated as $1/\Omega$. However, the many-body effects are not taken into account and the two-level model cannot explain the double resonance structure observed in experiment. Strictly speaking, the model may be realized only in optical lattice with both atoms in each site [94].

Mean-field treatment

The mean-field treatment presented in this section is mainly developed by our theoretical collaborator Prof. Zhifang Xu. Consider a system with n_{Rb} Rb atoms and n_{Na} Na atoms with spin $F = 1$. In principle, the system is a generalization of the single species spinor gas. However, as we will see, there are some new features that are unique in a mixture of spinor gases. The generalization is straight forward, just include all field operators as well as intraspecies and interspecies interaction in the general Hamiltonian (2.43). The resulting form is

$$\begin{aligned}
\hat{H} &= \hat{H}_{\mathrm{Rb}} + \hat{H}_{\mathrm{Na}} + \hat{H}_{\mathrm{RbNa}} \\
\hat{H}_{\mathrm{Rb}} &= \int dr \left[\hat{\psi}_m^\dagger \left(-\frac{\hbar^2}{2M_{\mathrm{Rb}}} \nabla^2 + V_{\mathrm{Rb}} - p_{\mathrm{Rb}} m + q_{\mathrm{Rb}} m^2 \right) \hat{\psi}_m \right. \\
&\qquad \left. + \frac{\alpha_{\mathrm{Rb}}}{2} \hat{\psi}_i^\dagger \hat{\psi}_j^\dagger \hat{\psi}_j \hat{\psi}_i + \frac{\beta_{\mathrm{Rb}}}{2} \hat{\psi}_i^\dagger \hat{\psi}_k^\dagger \mathbf{F}_{ij} \cdot \mathbf{F}_{kl} \hat{\psi}_l \hat{\psi}_j \right] \\
\hat{H}_{\mathrm{Na}} &= \int dr \left[\hat{\phi}_m^\dagger \left(-\frac{\hbar^2}{2M_{\mathrm{Na}}} \nabla^2 + V_{\mathrm{Na}} - p_{\mathrm{Na}} m + q_{\mathrm{Na}} m^2 \right) \hat{\phi}_m \right. \\
&\qquad \left. + \frac{\alpha_{\mathrm{Na}}}{2} \hat{\phi}_i^\dagger \hat{\phi}_j^\dagger \hat{\phi}_j \hat{\phi}_i + \frac{\beta_{\mathrm{Na}}}{2} \hat{\phi}_i^\dagger \hat{\phi}_k^\dagger \mathbf{F}_{ij} \cdot \mathbf{F}_{kl} \hat{\phi}_l \hat{\phi}_j \right] \\
\hat{H}_{\mathrm{RbNa}} &= \int dr \left[\frac{\alpha}{2} \hat{\psi}_i^\dagger \hat{\phi}_j^\dagger \hat{\phi}_j \hat{\psi}_i + \frac{\beta}{2} \hat{\psi}_i^\dagger \hat{\phi}_k^\dagger \mathbf{F}_{ij} \cdot \mathbf{F}_{kl} \hat{\phi}_l \hat{\psi}_j + \frac{\gamma}{2} \frac{(-1)^{i-j}}{3} \hat{\psi}_i^\dagger \hat{\phi}_{-i}^\dagger \hat{\phi}_{-j} \hat{\psi}_j \right],
\end{aligned} \tag{3.37}$$

where $\hat{\psi}_m$ and $\hat{\phi}_m$ are the field opererators of Rb and Na, α, β and γ are the interspecies interaction parameters defined in (3.13), α_i and β_i are intraspecies interaction parameters corresponding to c_0 and c_2 for each species. Starting from this Hamiltonian, we can make mean field approximation and SMA in the case that both Rb and Na are BEC. However, if they are not in condensed state, but are thermal cloud instead, the Hamiltonian is still valid but a quantum statistical treatment is needed for further calculations. To capture the main features of the dynamics, we start from treating the two BEC case.

From the form of interspecies interaction in Hamiltonian (3.37), we can conclude that the allowed spin-mixing collisions between a Rb atom and a Na atom have the following process characterized by the interaction strength [95]:

$$\begin{aligned} \beta: &\quad \left|1_{\mathrm{Rb}},0_{\mathrm{Na}}\right\rangle \leftrightarrow \left|0_{\mathrm{Rb}},1_{\mathrm{Na}}\right\rangle, \left|-1_{\mathrm{Rb}},0_{\mathrm{Na}}\right\rangle \leftrightarrow \left|0_{\mathrm{Rb}},-1_{\mathrm{Na}}\right\rangle \\ \beta-\gamma/3: &\quad \left|1_{\mathrm{Rb}},-1_{\mathrm{Na}}\right\rangle \leftrightarrow \left|0_{\mathrm{Rb}},0_{\mathrm{Na}}\right\rangle, \left|-1_{\mathrm{Rb}},1_{\mathrm{Na}}\right\rangle \leftrightarrow \left|0_{\mathrm{Rb}},0_{\mathrm{Na}}\right\rangle \\ \gamma: &\quad \left|1_{\mathrm{Rb}},-1_{\mathrm{Na}}\right\rangle \leftrightarrow \left|-1_{\mathrm{Rb}},1_{\mathrm{Na}}\right\rangle. \end{aligned} \tag{3.38}$$

By choosing proper initial state, we can select only one type of the above process while suppress the other process. This can be seen if we make the mean field approximation, i.e., replacing the field operators by their mean value. Specifically, if we choose

$$\vec{\hat{\psi}} = \begin{pmatrix} 0 \\ \sqrt{n_0^{\mathrm{Rb}}} e^{\theta_0} \\ \sqrt{n_{-1}^{\mathrm{Rb}}} e^{\theta_{-1}} \end{pmatrix} \psi(\mathbf{x}), \vec{\hat{\phi}} = \begin{pmatrix} 0 \\ \sqrt{n_0^{\mathrm{Na}}} e^{\varphi_0} \\ \sqrt{n_{-1}^{\mathrm{Na}}} e^{\varphi_{-1}} \end{pmatrix} \phi(\mathbf{x})$$

as the initial state, where $n_i^j (i = -1, 0, 1; j = \mathrm{Rb,Na})$ are the atom number of the two BECs, θ_i and φ_i are the condensate phase of each component, $\psi(\mathbf{x})$ and $\phi(\mathbf{x})$ are the condensate spatial wavefunctions for Rb and Na normalized to 1, $\int \psi(\mathbf{x})\, d\mathbf{x} = \int \phi(\mathbf{x})\, d\mathbf{x} = 1$. Substitute the above state into (3.37), we can get the mean field energy functional

$$\begin{aligned}
E &= E_{\text{Rb}} + E_{\text{Na}} + E \\
E_j &= -p_j m_j + q_j \left(n_j - n_0^j\right) + \frac{1}{2}{\beta'}_j m_j^2 \\
&+ {\beta'}_j n_0^j \left[\left(n_j - n_0^j\right) + \sqrt{\left(n_j - n_0^j\right)^2 - m_j^2} \cos\eta_j\right] \\
E_{\text{RbNa}} &= \frac{1}{2}\beta' m_{\text{Rb}} m_{\text{Na}} + \frac{1}{6}\gamma' \left(n_1^{\text{Rb}} n_{-1}^{\text{Na}} + n_0^{\text{Rb}} n_0^{\text{Na}} + n_{-1}^{\text{Rb}} n_1^{\text{Na}}\right) \\
&+ \frac{1}{3}\gamma' \sqrt{n_1^{\text{Rb}} n_{-1}^{\text{Rb}} n_1^{\text{Na}} n_{-1}^{\text{Na}}} \cos\eta_3 \\
&+ \left(\beta' - \frac{1}{3}\gamma'\right) \sqrt{n_0^{\text{Rb}} n_{-1}^{\text{Rb}} n_1^{\text{Na}} n_0^{\text{Na}}} \cos\left(\frac{\eta_1 + \eta_2 + \eta_3}{2}\right) \\
&+ \left(\beta' - \frac{1}{3}\gamma'\right) \sqrt{n_1^{\text{Rb}} n_0^{\text{Rb}} n_0^{\text{Na}} n_1^{\text{Na}}} \cos\left(\frac{\eta_1 + \eta_2 + \eta_3}{2}\right) \\
&+ \beta' \sqrt{n_0^{\text{Rb}} n_{-1}^{\text{Rb}} n_0^{\text{Na}} n_{-1}^{\text{Na}}},
\end{aligned} \tag{3.39}$$

where $n_j = n_{-1}^j + n_0^j + n_1^j$ is the total number for each species, $m_1 = n_1^{\text{Rb}} - n_{-1}^{\text{Rb}}$ and $m_2 = n_1^{\text{Na}} - n_{-1}^{\text{Na}}$ are the magnetization for eahc species, $m = m_1 + m_2$ is the total magnetization, $m_3 = m_1 - m_2$ is the magnetization difference, $\eta_1 = \theta_1 + \theta_{-1} - 2\theta_0$, $\eta_2 = \varphi_1 + \varphi_{-1} - 2\varphi_0$, $\eta_3 = \theta_{-1} - \theta_1 + \varphi_1 - \varphi_{-1}$. ${\beta'}_1 = \beta_1 \int |\psi(\mathbf{x})|^4 d\mathbf{x}$, ${\beta'}_2 = \beta_2 \int |\phi(\mathbf{x})|^4 d\mathbf{x}$, $(\beta', \gamma') = (\beta, \gamma) \int |\psi(\mathbf{x})|^2 |\phi(\mathbf{x})|^2 d\mathbf{x}$.

The dynamical equations are given by

$$\begin{aligned}
\dot{n}_0^{\text{Rb}} &= -\frac{2}{\hbar}\frac{\partial E}{\partial \eta_1}, \dot{\eta}_1 = \frac{2}{\hbar}\frac{\partial E}{\partial n_0^{\text{Rb}}}, \\
\dot{n}_0^{\text{Na}} &= -\frac{2}{\hbar}\frac{\partial E}{\partial \eta_2}, \dot{\eta}_2 = \frac{2}{\hbar}\frac{\partial E}{\partial n_0^{\text{Na}}}, \\
\dot{m}_3 &= -\frac{4}{\hbar}\frac{\partial E}{\partial \eta_3}, \dot{\eta}_3 = \frac{4}{\hbar}\frac{\partial E}{\partial m_3}.
\end{aligned} \tag{3.40}$$

The first two lines describe the intraspecies dynamics of Rb and Na respectively, which become fast and small amplitude oscillation at high magnetic field, as describe in previous section. When the magnetic field reaches as high as 0.7G, the populations of each components can be viewed as constant for each species in the absence of interspecies interaction. Hence we can neglect the first two lines of equations and concentrate on the third pair of equation, which describe the magnetization evolution of each species. written down explicitly, they are

$$\begin{aligned}\dot{m}_3 &= \frac{\beta'}{2\hbar}\sqrt{\left(m^2-m_3^2\right)\left(2n_{\mathrm{Rb}}+m+m_3\right)\left(2n_{\mathrm{Na}}+m-m_3\right)}\sin\left(\frac{\eta_1-\eta_2+\eta_3}{2}\right)\\ \dot{\eta}_3 &= -\frac{2\left(p_{\mathrm{Rb}}-p_{\mathrm{Na}}\right)}{\hbar}+\frac{{\beta'}_{\mathrm{Rb}}-{\beta'}_{\mathrm{Na}}}{\hbar}m+\frac{{\beta'}_{\mathrm{Rb}}+{\beta'}_{\mathrm{Na}}-\beta'}{\hbar}m_3\\ &\quad -\frac{\beta'}{2\hbar}\frac{m_3\sqrt{\left(2n_{\mathrm{Rb}}+m+m_3\right)\left(2n_{\mathrm{Na}}+m-m_3\right)}}{\sqrt{m^2-m_3^2}}\cos\left(\frac{\eta_1-\eta_2+\eta_3}{2}\right).\end{aligned} \tag{3.41}$$

This set of equation has a similar structure compare with the single species dynamical equations (3.26), with the role of (ρ_0,θ) played by (m_3,η_3). Hence, the solutions are periodic oscillations of these variables, and other populations can be calculated due to total magnetization conservation and atom number conservations for each species.

Equation (3.41) can be numerically solved, e.g., by Mathematica. Here, we give an analytical solution. (3.41) can be written as

$$\left(\dot{m}_3\right)^2=\left(\frac{\beta'}{2\hbar}\right)^2\left(d_0+d_1m_3+d_2m_3^2+d_3m_3^3+d_4m_3^4\right)$$

in which

$$\begin{aligned}e_1 &= -\frac{1}{2}\left(p_{\mathrm{Rb}}-p_{\mathrm{Na}}+q_{\mathrm{Rb}}-q_{\mathrm{Na}}\right)-\frac{1}{4}\left[{\beta'}_{\mathrm{Rb}}\left(2n_{\mathrm{Rb}}+m\right)-{\beta'}_{\mathrm{Na}}\left(2n_{\mathrm{Na}}+m\right)\right]\\ e_2 &= -\frac{1}{8}\left({\beta'}_{\mathrm{Rb}}+{\beta'}_{\mathrm{Na}}+\beta'\right)\\ \tilde{E} &= e_1m_3+e_2m_3^2+\frac{\beta'}{4}\sqrt{\left(m^2-m_3^2\right)\left(2n_{\mathrm{Rb}}+m+m_3\right)\left(2n_{\mathrm{Na}}+m-m_3\right)}\\ &\quad\cdot\cos\left(\frac{\eta_1-\eta_2+\eta_3}{2}\right).\end{aligned} \tag{3.42}$$

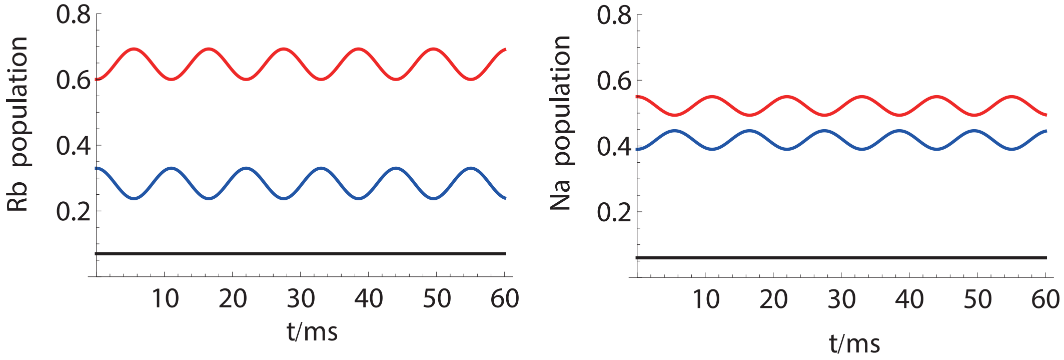

Figure 3.5: Spin mixing dynamics from mean field equation (3.41). The population oscillations are plotted for Rb (left) and Na (right), in hyperfine spin state $|1,-1\rangle$ (red), $|1,0\rangle$ (blue) and $|1,1\rangle$ (black). The experimental atom conditions are used and the magnetic field is 1.9G.

$$\begin{aligned}
&d_0 = -\frac{16}{\beta'}\tilde{E}^2 + m^4 + 2m^3\left(n_{\mathrm{Rb}} + n_{\mathrm{Na}}\right) + 4m^2 n_{\mathrm{Rb}} n_{\mathrm{Na}},\\
&d_1 = \frac{32e_1}{\beta'}\tilde{E} - 2m^2\left(n_{\mathrm{Rb}} - n_{\mathrm{Na}}\right), d_2 = -\frac{16}{\beta'}\left(e_1^2 - 2e_2\tilde{E}\right) - 2m\left(m + n_{\mathrm{Rb}} + n_{\mathrm{Na}}\right),\\
&d_3 = -\frac{32e_1e_2}{\beta'^2} + 2n_{\mathrm{Rb}} - 2n_{\mathrm{Na}}, \quad d_4 = 1 - \frac{16e_2^2}{\beta'^2}.
\end{aligned} \tag{3.43}$$

This form of differential equation has the solution that can be expressed by elliptic functions. After identifying the four roots of the equation $d_0 + d_1 m_3 + d_2 m_3^2 + d_3 m_3^3 + d_4 m_3^4 = 0$ and arranging them so that $x_1 < x_2 < x_3 < x_4$, the solution is given by

$$m_3\left(t\right) = \frac{\left(x_4 - x_2\right)x_3 + \left(x_2 - x_3\right)x_4 y^2}{x_4 - x_2 + \left(x_2 - x_3\right)y^2}, \tag{3.44}$$

where

$$
\begin{aligned}
y_1 &= F\left(\arcsin\sqrt{\frac{(x_2-x_4)(m_3(0)-x_3)}{(x_2-x_3)(m_3(0)-x_4)}},\sqrt{\frac{(x_2-x_3)(x_1-x_4)}{(x_1-x_3)(x_2-x_4)}}\right)\\
y_2 &= \frac{2}{\sqrt{(x_1-x_3)(x_2-x_4)}}\\
y_3 &= \sqrt{\frac{(x_2-x_3)(x_1-x_4)}{(x_1-x_3)(x_2-x_4)}}\\
y &= \mathrm{sn}\left(y_1+\sqrt{d_4}\frac{\beta'}{2\hbar}t/y_2, y_3\right),
\end{aligned}
\tag{3.45}
$$

in which $F(\varphi, k)$ is the elliptic function of the first kind, $\mathrm{sn}(u, k)$ is one of the Jocobi elliptic functions. The solution (3.44) is a period function of time, hence the population of each spin component of each species exhibit oscillations. A typical dynamics at the external field of 1.9G is depicted in Fig. 3.5.

Many-body formalism

The many-body formalism described in this section is mainly develop my our theoretical collaborators Prof. Shizhong Zhang and Prof. Zhifang Xu. When one of the atomic species are not in the condensed state, we can no longer use the mean field approximation. In this case, finite temperature must be taken into account. A basic kinetic approach can be adopted to derive the dynamical equations. For a thermal cloud (^{87}Rb in our experiment), the evolution of spin polarization and spatial distribution can be describe by the Wigner function [96, 97]

$$
g_{ij}(\mathbf{R},\mathbf{p};t)=\int d\mathbf{r}e^{-i\mathbf{p}\cdot\mathbf{r}}\left\langle\hat{\psi}_j^\dagger\left(\mathbf{R}+\frac{\mathbf{r}}{2},t\right)\hat{\psi}_i\left(\mathbf{R}-\frac{\mathbf{r}}{2},t\right)\right\rangle,
\tag{3.46}
$$

which can be viewed as a thermal average of the Wigner operator. Since there are three spin component for $F=1$, $g(\mathbf{R},\mathbf{p};t)$ is a 3×3 matrix. The equation that governs the time evolution of the Wigner function can be written in the following general form

$$\begin{aligned}&\frac{\partial g\left(\mathbf{R},\mathbf{p};t\right)}{\partial t}+\frac{\mathbf{p}}{m_{\mathrm{Rb}}}\cdot g\left(\mathbf{R},\mathbf{p};t\right)\\&-\frac{1}{2}\left\{\nabla_{\mathbf{R}}U_{\mathrm{Rb}},\nabla_{\mathbf{R}}g\left(\mathbf{R},\mathbf{p};t\right)\right\}-\frac{i}{\hbar}\left[g\left(\mathbf{R},\mathbf{p};t\right),U_{\mathrm{Rb}}\right]=I_{\mathrm{Rb}},\end{aligned}\tag{3.47}$$

where I_{Rb} is the collision integral that describes the effects of interactions that are not captured in the effective potential $U_{\mathrm{Rb}}\left(\mathbf{R},\mathbf{p};t\right)$, which is in general a matrix function of $\mathbf{R}$, $\mathbf{p}$ and t. The kinetic equation can be derived from the Heisenberg equation of motion for the Wigner operator. In our calculation, $U_{\mathrm{Rb}}\left(\mathbf{R},\mathbf{p};t\right)$ is obtained within the random phase approximation (RPA), which we generalize to the case of Bose-Bose mixtures. The anti-commutator $\{A,B\}$ and the commutator $[A,B]$ refer to quantities in spin space.

For Na condensate, as is the case in our experiment, the mean-field approximation is adopted, and the field operator is replaced by its expectation value $\phi_i\left(\mathbf{r},t\right)$. Starting from the Hamiltonian (3.37), we can find the expression for $U_{\mathrm{Rb}}\left(\mathbf{R},\mathbf{p};t\right)$ and the time dependences for $\phi_i\left(\mathbf{r},t\right)$. There are three contributions to $U_{\mathrm{Rb}}\left(\mathbf{R},\mathbf{p};t\right)$. The first comes from the single particle term

$$U_{\mathrm{Rb}}^{(1)}\left(\mathbf{R}\right)=V_{\mathrm{Rb}}\left(\mathbf{R}\right)-p_{\mathrm{Rb}}F_z+q_{\mathrm{Rb}}F_z^2\tag{3.48}$$

The second term comes from the intra-species interactions. Here one uses the RPA and obtain the following expression

$$U_{\mathrm{Rb}}^{(2)}\left(\mathbf{R};t\right)=c_0^{\mathrm{Rb}}\left(\mathrm{Tr}n_{\mathrm{Rb}}+n_{\mathrm{Rb}}\right)+c_2^{\mathrm{Rb}}\mathrm{Tr}\left(\mathbf{F}n_{\mathrm{Rb}}\right)\cdot\mathbf{F}+c_2^{\mathrm{Rb}}\mathrm{Tr}\left(\mathbf{F}n_{\mathrm{Rb}}\cdot\mathbf{F}\right)\tag{3.49}$$

where $\mathbf{F}=\left(F_x,F_y,F_z\right)$ is the spin-1 angular momentum vector operator, n_{Rb} is defined to be

$$n_{\mathrm{Rb,ij}}\left(\mathbf{R},t\right)=\left\langle\hat{\psi}_j^{\dagger}\left(\mathbf{R},t\right)\hat{\psi}_i\left(\mathbf{R},t\right)\right\rangle\tag{3.50}$$

The last contribution comes from the inter-species interactions and can be written as

$$U_{\mathrm{Rb}}^{(3)}\left(\mathbf{R};t\right)=\alpha\mathrm{Tr}n_{\mathrm{Na}}+\beta\mathrm{Tr}\left(\mathbf{F}n_{\mathrm{Na}}\right)\cdot\mathbf{F}+\gamma U_{\phi} \tag{3.51}$$

where

$$n_{\mathrm{Rb,ij}}\left(\mathbf{R},t\right)=\phi_j^*\left(\mathbf{R},t\right)\phi_i\left(\mathbf{R},t\right) \tag{3.52}$$

and

$$U_{\phi}=\frac{1}{3}\begin{pmatrix}\phi_{-1}^*\phi_{-1} & -\phi_{-1}^*\phi_0 & \phi_{-1}^*\phi_1\\ -\phi_0^*\phi_{-1} & \phi_0^*\phi_0 & -\phi_0^*\phi_1\\ \phi_1^*\phi_{-1} & -\phi_1^*\phi_0 & \phi_1^*\phi_1.\end{pmatrix} \tag{3.53}$$

The equation of motion for the condensate order parameter $b^{\dagger}=\left(b_{-1}^*,b_0^*,b_1^*\right)$ can be similary written as

$$\begin{aligned}i\hbar\frac{\partial}{\partial t}\phi=&\left[-\frac{\hbar^2\nabla^2}{2m_{\mathrm{Na}}}-p_{\mathrm{Na}}F_z+q_{\mathrm{Na}}F_z^2+V_{\mathrm{Na}}+c_0^{\mathrm{Na}}\mathrm{Tr}n_{\mathrm{Na}}+c_2^{\mathrm{Na}}\mathrm{Tr}\left(b^{\dagger}\mathbf{F}b\right)\cdot\mathbf{F}\right]b\\&+\alpha\mathrm{Tr}\left(n_{\mathrm{Rb}}\right)b+\beta\mathrm{Tr}\left(n_{\mathrm{Rb}}\mathbf{F}\right)\cdot\mathbf{F}b+\gamma U_{\psi}b,\end{aligned} \tag{3.54}$$

where

$$U_{\psi}=\frac{1}{3}\begin{pmatrix}\left\langle\psi_{-1}^*\psi_{-1}\right\rangle & -\left\langle\psi_{-1}^*\psi_0\right\rangle & \left\langle\psi_{-1}^*\psi_1\right\rangle\\ -\left\langle\psi_0^*\psi_{-1}\right\rangle & \left\langle\psi_0^*\psi_0\right\rangle & -\left\langle\psi_0^*\psi_1\right\rangle\\ \left\langle\psi_1^*\psi_{-1}\right\rangle & -\left\langle\psi_1^*\psi_0\right\rangle & \left\langle\psi_1^*\psi_1\right\rangle\end{pmatrix} \tag{3.55}$$

Now equation (3.47) and (3.54) provide a complete description of the Bose mixture system with one component being thermal and the other condensate. The equations are difficult to solve in general, however, SMA can be made as in the following. For Rb thermal cloud, we can write

$$n_{\mathrm{Rb},ij}\left(\mathbf{R},\mathbf{p};t\right)=Z^{-1}\exp\left[-\frac{p^{2}/2m_{\mathrm{Rb}}+V_{\mathrm{Rb}}\left(\mathbf{R}\right)}{k_{\mathrm{B}}T}\right]\sigma_{ij}\left(t\right). \tag{3.56}$$

Namely, the $\mathbf{R}$ and $\mathbf{p}$ dependences of $n_{\mathrm{Rb},ij}$ is given by the thermal distribution, which is also independent of time, while its spin dependence is given by $\sigma_{ij}\left(t\right)$. Here

$$Z=\int d\mathbf{R}\int\frac{d\mathbf{p}}{\left(2\pi\hbar\right)^{3}}\exp\left[-\frac{p^{2}/2m_{\mathrm{Rb}}+V_{\mathrm{Rb}}\left(\mathbf{R}\right)}{k_{\mathrm{B}}T}\right] \tag{3.57}$$

is the classical partition function. For Na condensate, we write

$$\phi_{i}\left(\mathbf{R},t\right)=\sqrt{\mathrm{Tr}\left(n_{\mathrm{Rb}}\left(\mathbf{R}\right)\right)}\varsigma_{i}\left(t\right)\equiv\sqrt{n_{\mathrm{c}}\left(\mathbf{R}\right)}\varsigma_{i}\left(t\right), \tag{3.58}$$

where the total condensate density of Na, $n_{\mathrm{c}}\left(\mathbf{R}\right)$, is independent of time. The spin part of the condensate wave function is given by $\varsigma_{i}\left(t\right)$ which carries all the time-dependences. The matrix σ and the spinor ς_{i} satisfy the following conditions:

$$\mathrm{Tr}\sigma=1,\sum_{i}\varsigma_{i}^{*}\varsigma_{i}=1 \tag{3.59}$$

The condensate density distribution can be approximated by the usual Thomas-Fermi form in the harmonic trap. With these prepartions, we can substitute equation (3.56) into equation (3.47) and integrate over $\mathbf{R}$ and $\mathbf{p}$ on both sides. Let us neglect the collision integral I_{Rb}, which contributes to the damping of the oscillations. The second and third terms in the left hand side of equation (3.47) vanishes upon integration over $\mathbf{R}$ and $\mathbf{p}$. Thus we find

$$\frac{\partial\sigma}{\partial t}=\frac{i}{\hbar}\left[\sigma,M_{\mathrm{TG}}\right], \tag{3.60}$$

where

$$
\begin{aligned}
M_{\mathrm{TG}} = & - p_{\mathrm{Rb}} F_z + q_{\mathrm{Rb}} F_z^2 + c_2^{\mathrm{Rb}} \bar{n} \mathrm{Tr}\left(\mathbf{F}\sigma\right) \cdot \mathbf{F} + c_2^{\mathrm{Rb}} \bar{n} \mathrm{Tr}\left(\mathbf{F}\sigma \cdot \mathbf{F}\right) \\
& + \beta \bar{n}_{\mathrm{tc}} \sqrt{\frac{N_{\mathrm{Na}}}{N_{\mathrm{Rb}}}} \mathrm{Tr}\left(\mathbf{F}\tau\right) \cdot \mathbf{F} + \gamma \bar{n}_{\mathrm{tc}} \sqrt{\frac{N_{\mathrm{Na}}}{N_{\mathrm{Rb}}}} U_{\varsigma},
\end{aligned}
\tag{3.61}
$$

where $\bar{n}$ and $\bar{n}_{\mathrm{tc}}$ are defined by

$$
\begin{aligned}
\bar{n} &= \frac{1}{N_{\mathrm{Rb}}} \int d\mathbf{R} [\mathrm{Tr}\left(n_{\mathrm{Rb}}\right)]^2 \\
\bar{n}_{\mathrm{tc}} &= \frac{1}{\sqrt{N_{\mathrm{Rb}} N_{\mathrm{Na}}}} \int d\mathbf{R} \mathrm{Tr}\left(n_{\mathrm{Rb}}\right) n_{\mathrm{c}}\left(\mathbf{R}\right),
\end{aligned}
\tag{3.62}
$$

and τ is defined by

$$
\tau_{ij} = \zeta_j^* \zeta_i, \mathrm{Tr}\left(\tau\right) = 1,
\tag{3.63}
$$

and the matrix

$$
U_{\tau} = \frac{1}{3} \begin{pmatrix} \zeta_{-1}^* \zeta_{-1} & -\zeta_{-1}^* \zeta_0 & \zeta_{-1}^* \zeta_1 \\ -\zeta_0^* \zeta_{-1} & \zeta_0^* \zeta_0 & -\zeta_0^* \zeta_1 \\ \zeta_1^* \zeta_{-1} & -\zeta_1^* \zeta_0 & \zeta_1^* \zeta_1 . \end{pmatrix}
\tag{3.64}
$$

The equation of motion of the condensate order parameter ϕ can be written in terms of τ, in a similar form as for σ. By substituting equation (3.58) into (3.54) and integrate over $\mathbf{R}$, we find

$$
\frac{\partial}{\partial t} \tau = \frac{i}{\hbar} \left[\tau, M_{\mathrm{BEC}}\right],
\tag{3.65}
$$

where

$$
\begin{aligned}
M_{\mathrm{BEC}} = & - p_{\mathrm{Na}} F_z + q_{\mathrm{Na}} F_z^2 + c_2^{\mathrm{Na}} \bar{n}_{\mathrm{c}} \mathrm{Tr}\left(\mathbf{F}\tau\right) \cdot \mathbf{F} \\
& + \beta \bar{n}_{\mathrm{tc}} \sqrt{\frac{N_{\mathrm{Rb}}}{N_{\mathrm{Na}}}} \mathrm{Tr}\left(\mathbf{F}\sigma\right) \cdot \mathbf{F} + \gamma \bar{n}_{\mathrm{tc}} \sqrt{\frac{N_{\mathrm{Rb}}}{N_{\mathrm{Na}}}} U_{\sigma},
\end{aligned}
\tag{3.66}
$$

in which the matrix U_σ is defined to be

$$U_\sigma = \frac{1}{3}\begin{pmatrix} \sigma_{-1,-1} & -\sigma_{-1,0} & \sigma_{-1,1} \\ -\sigma_{0,-1} & \sigma_{0,0} & -\sigma_{0,1} \\ \sigma_{1,-1} & -\sigma_{1,0} & \sigma_{1,1}, \end{pmatrix} \tag{3.67}$$

and the mean density $\bar{n}_{\mathrm{c}}$ defined by

$$\bar{n}_{\mathrm{c}} = \frac{1}{N_{\mathrm{Na}}}\int d\mathbf{R} n_{\mathrm{c}}(\mathbf{R})^2. \tag{3.68}$$

By solving the equaitons (3.60) and (3.65), we can calculate the dynamics of the mixture of a Na BEC and a Rb thermal cloud in a particular initial spin state. It turns out that the solutions are periodic oscillations of the population in each spin component. The effect of external magnetic field and interaction strength can be seen by changing the parameters in the equation. Both mean field theory and the kinetic equations predict a resonance behaviour near 1.69G, where the inter-species interaction energy and the differential Zeeman energy between Rb and Na are comparable.

Chapter 4

Experimental Setup and Methods

In this chapter the experiment setup for trapping Rb and Na and cooling them to quantum degeneracy is described in detail.

4.1 Components of the setup

Laser cooling and trapping is the basic technique in a lab working on quantum gases. To avoid severe loss from the background gas collision, the trapped atoms are placed in an ultra-high vacuum. To further cool down the gas, magnetic trap or optical trap are needed and the experimental methods utilizing magnetic coils, lasers and microwave devices become essential. Hence, the experimental apparatus for producing a BEC is sophisticated with advanced experimental methods developed in AMO physis and condensed matter physics. We can roughly divide our experimental setup into five parts and describe their basic structures and functions. These includes:

Vacuum system - Provides an ultra-high vacuum environment for the atom trap so that the atomic cloud has a long enough lifetime for physical experiments, and the system can be viewed as isolated from the thermal environment.

Lasers and optical system - Several lasers with different wavelengths are generated to provide lights for trapping, cooling, optical pumping and detecting the atoms, as well as for spectroscopy study. To guide the light paths and precisely control the frequency and intensity, a complex and compact optical system is designed.

Magnetic fields - Helmholtz and anti-Helmholtz coils are used to generate uniform magnetic field and magnetic gradient field, widely used to control the energy levels of the atoms and trap the spin polarized atoms.

RF and microwave devices - The high-frequency electronics produce oscillating electromagnetic waves which are used in evaporative cooling in magnetic trap and to manipulate the atomic spin states.

Computer control system - Computers are used to control the time sequences of all components in the system, precisely carry out the operations we design to run an experiment.

In the following, the five parts of the system will be described in detail.

4.1.1 Vacuum System

The vacuum system consists of a single chamber connected with an ion pump through standard stainless vacuum components. The chamber is a glass cell without anti-reflection coating, which outer dimensions is 100mm×40mm×40 mm. The atom sources of Rb and Na are provided by dispensers (Alvatec GmbH) which are directly inserted into the glass cell from the opposite site the CF35 tube connecting the cell, with a distance of $\sim$ 12cm from the dispenser and cell center. The vacuum is maintained by the ion pump Gamma Vacuum 45S, with a pressure of 1.2×10^{-11}torr. A titanium sublimation pump (Varian Vacuum TSP Cartridge) is also installed but was only fired once during the vacuum preparing stage. The whole vacuum system is shown in Fig. 4.1.

The high vacuum is, however, against the MOT loading due to low vapor pressure. To solve the contradiction, an 365nm ultraviolet (UV) light-emitting diode (LED) is turned on to temporarily increase the vapor pressure, exploiting the light induced atom desorption (LIAD) effect. The LED (Thorlabs M365L2) is located near the cell and has a maximum output power of 200mW. A simple test estimates that the atom number with LIAD loading into a MOT can reach ∼30 times of that without turning on the LED.

After the preparation for the ultra-high vacuum (UHV), the the dispenser was fired with a 2.5A current for one day in order to coat the cell walls with Rb. In day-to-day operations, we find a decrease of the Rb atoms without firing the dispenser while an increase of the pressure with too large current through the dispenser. Hence a 1.7A current is applied to the dispenser and keep Rb vapor pressure constant during experiment cycles.

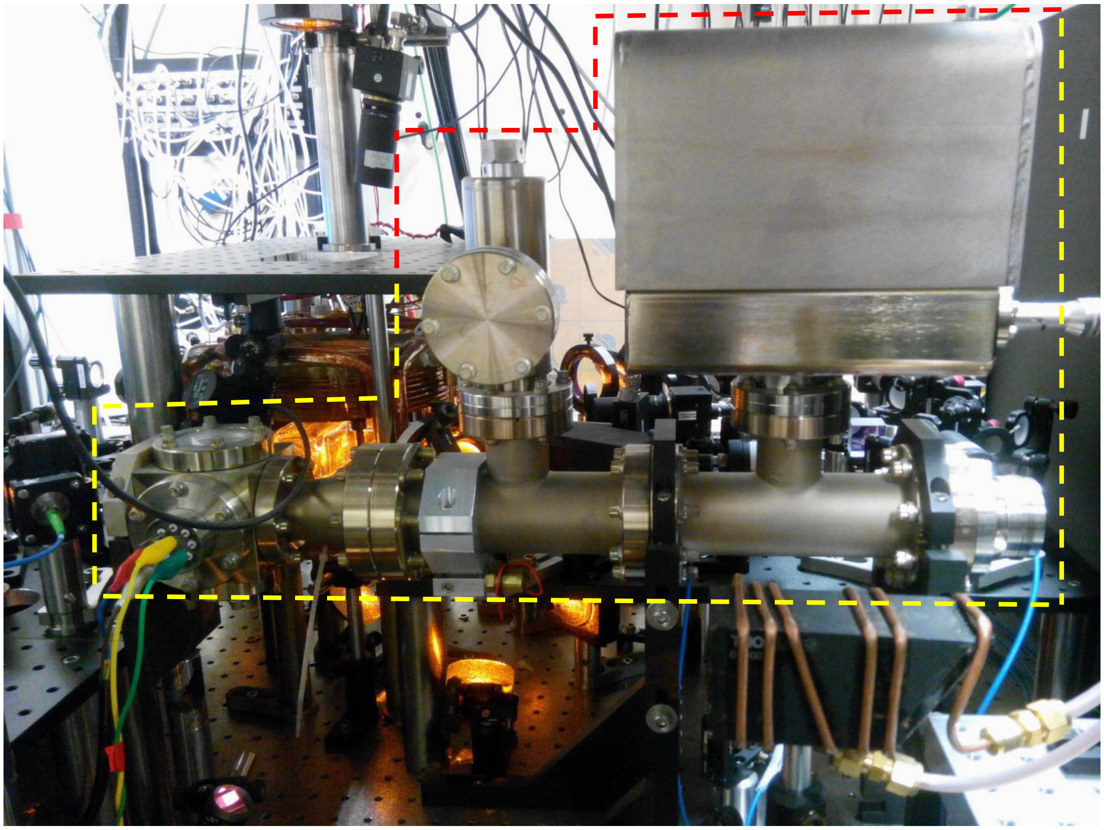

Figure 4.1: Photo of the vacuum system. Inside the dashed box are the ion pump, glass cell, dispenser, tubes and connectors.

4.1.2 Lasers

Lasers are essential tools for trapping and cooling atoms. In our experimental apparatus, the types of lasers with different wavelengths include:

(1) Diode laser

The laser diode is a semiconductor laser, with the active medium formed by a p-n junction. It is widely used in laser cooling and trapping experiments. The trapping beam for Rb MOT in our setup is provided by a slave diode laser (Thorlabs LD785-SH300) with wavelength 780nm and maximum power 300mW. The slave laser is seeded by another external cavity diode laser (ECDL), which is locked to the Rb atomic transition $F = 2 \leftrightarrow F' = 3$ by means of saturated absorption spectroscopy. Another ECDL locked to $F = 1 \leftrightarrow F' = 2$ is used to provide the light for repumping the atoms to the cycling transition.

Commercial laser diode has a large output linewidth, and the frequency fluctuation and drift can easily exceed the atomic transition linewidth. In order to reduce the linewidth, the laser diode is either seeded by another laser with narrower linewidth, or receive feedback from an external cavity, which are the cases for our slave laser and ECDLs, respectively.

We use a Littrow configuration in our ECDLs [98, 99]. The laser diode output beam is reflected by a light grating (Thorlabs GH13-18V, with 1800 grooves/mm) with the angle θ between the surface and the beam about 45°. The grating is chosen so that the zeroth order reflected beam is the output of the ECDL, and the first order diffracted beam coincides with the diode output and travels back, hence serves as an optical feedback for the laser diode. In this situation the mode determined by the cavity length (from diode to grating) become dominated and suppress other modes hence reduce the linewidth, and the output wavelength becomes tunable if we add a piezoelectric ceramic transducer (e.g., $\mathrm{Pb[Zr_xTi_{1-x}]O_3}$, or PZT) into the mount holding the grating. The configuration is shown in Fig.

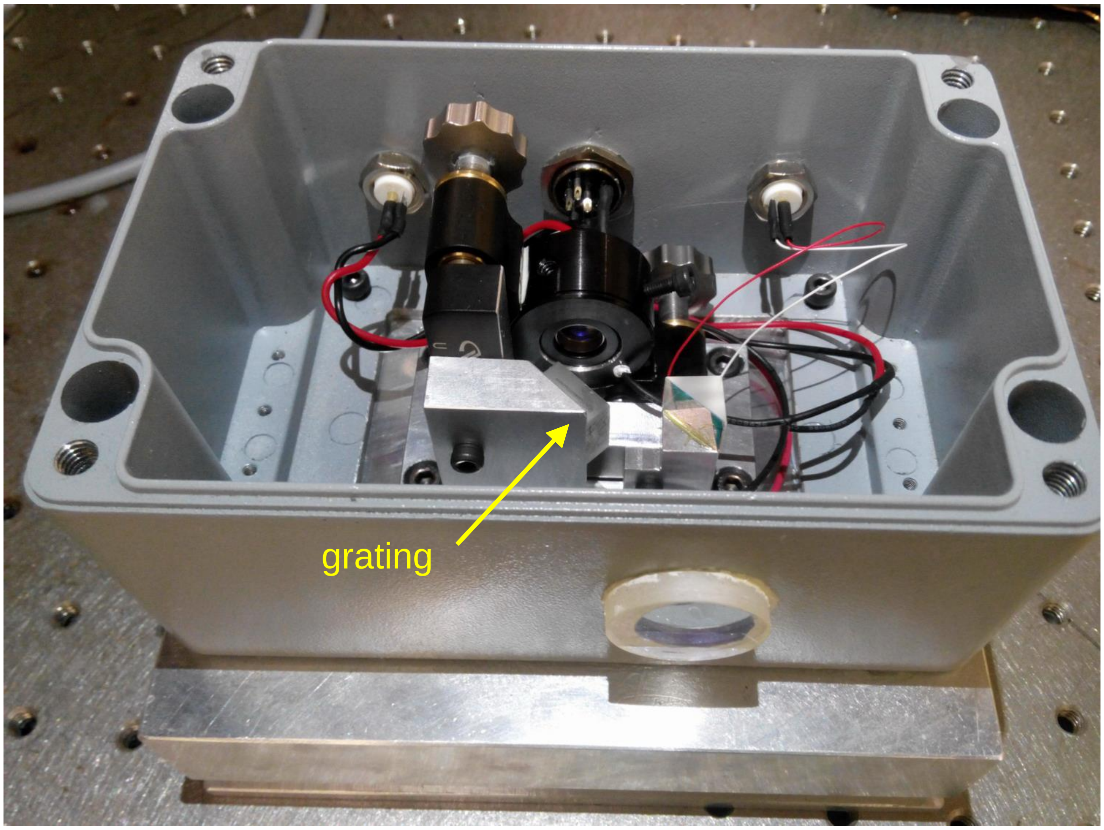

Figure 4.2: Photo of the structure of the ECDL. The yellow arrow indicates the position of the grating, which forms an external cavity together with the surface the laser diode in the Littrow configuration. The diode is inserted in the mirror mount installed on an aluminum block with a thermoelectric heat pump between them. The three ports on the rear panel are for the current driver, temperature controller and temperature sensor. To protect the laser output, a window with antireflection coating is installed at the output port.

4.2. A special type of diode laser is distributed feedback (DFB) laser in which the Bragg grating is built internally. DFB lasers have narrow linewidth (<1MHz) and tunable wavelengths in several hundreds of GHz range. In our lab, a 795nm DFB laser is setup and used in special purposes, for example in imaging in high magnetic field and spectroscopy studies.

(2) Dye laser

For Na atoms, the 589nm transition wavelength is not covered by most types

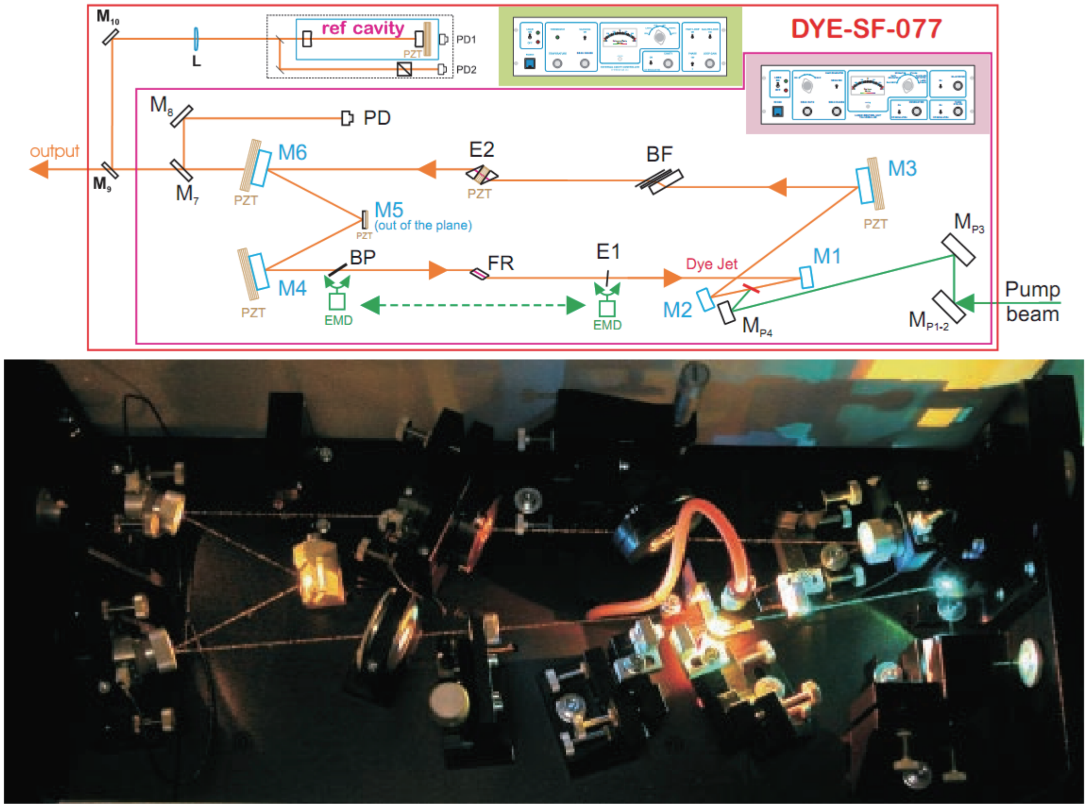

Figure 4.3: Dye laser generating the 589nm laser light for Na. Upper panel: Schematic diagram of the structure of the dye laser with a ring cavity. Lower panel: photo of the dye laser with laser generation. Pictures from the manual of the Dye laser DYE-SF-077.

of laser makes dye laser the only choice (in early days). Our dye laser (DYE-SF-077) is a CW single-frequency ring laser, which has a narrow output linewidth of less than 100kHz. The dye laser system consists of a ring cavity, an electronic control unit, a dye circulation system and a 532nm diode-pumped solid-state laser (DPSSL, IPG photonics) used to pump the dye. The dye in use is Rhodamine 6G powder, methanol and ethylene glycol as the solvent replaced about every three months due to degradation. The configuration of the ring cavity is shown in Fig. 4.3. The dye laser is placed inside a plexiglass box purged with filtered air to keep the cavity mirrors clean and maintain the output power, which is typically 600mW. To stabilize the output frequency, the ring cavity is locked to an external cavity which has a finesse of 300-400 and free spectral range of 750MHz, and the cavity is locked to the Na $F = 2 \leftrightarrow F' = 3$ atomic transition through saturated absorption spectroscopy.

(3) Fiber laser

The 1070nm laser beam which provides the far-off-resonant trap or optical dipole trap (ODT) is generated by a multi-frequency fiber laser (IPG photonics). The maximum output power is 100W but typically 15W is used. The fiber laser beam has a Gaussian profile and is particularly suited to form an ODT. Fig. 4.4 shows the intensity profile of the beam at waist after the optical system which tightly focus the beam and form a three dimensional Gaussian shape.

(4) Diode-pumped solid-state laser

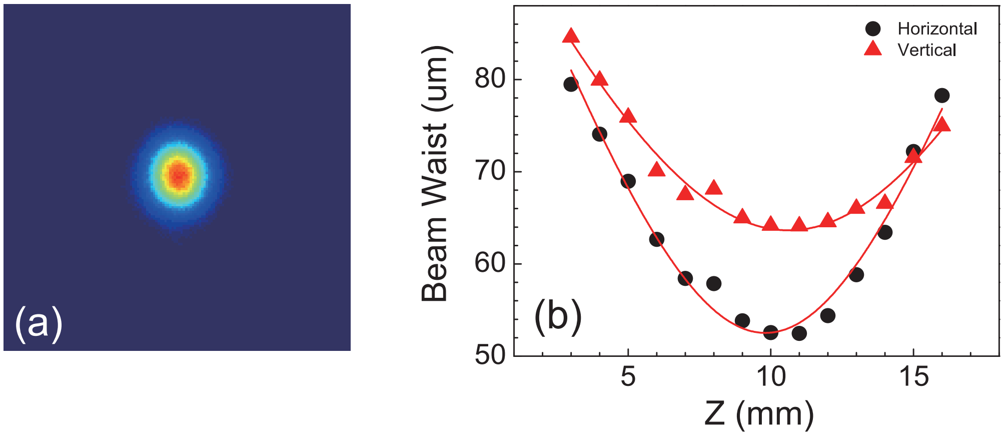

Figure 4.4: Beam profile of the 1070nm fiber laser. (a) The light spot is measured by a CCD (Mightex SCE-B013-U) at the focus which is also the center of ODT. (b) The measured beam sizes along the z direction, which is fitted by the propagation equation of Gaussian beam. The beam has a good gaussian profile with beamwaists of 52μm and 47μm in horizontal and vertical directions, and the typical measured value of M squared parameter is 1.2.

Compared with diode lasers, DPSSLs can usually have higher power and better beam quality. In our lab, the 532nm laser used to pump the dye laser is a DPSSL. Another DPSSL is working at 660nm, which is overlapped with one beam of the ODT and used to provide a deeper trap depth for Na while reduces the trap depth for Rb and makes the two atomic cloud sizes closer.

4.1.3 Optical System

For laser cooling and trapping, an enormous and complex optical system is usually need: (1) to guide the laser light to desired paths or form atom traps (e.g., MOT). (2) to stabilize the frequency and intensity of the light. The optical system is composed of mirrors, lens, beamsplitters, waveplates, filters, prisms, fibers, optical isolators, acousto-optic modulators (AOMs), atom vapor cells, photodiodes, charge-coupled devices (CCDs) and related electronic circuits, most of which are installed on the optical tables.

The optical layouts for producing 780nm beam for Rb are schematically drawn in Fig. 4.5 and Fig. 4.6 respectively. The trapping beam is generated by the trapping laser at frequency near $F = 2 \leftrightarrow F'$ or 384.22813THz, and pass through a anamorphic prism pairs (PBS871-B) to acquire a near unity aspect ratio of the beam profile. Then a small fraction of the beam is split out for saturated absorption spectroscopy, and the frequency is locked to the crossover peak of $F' = 1$ and $F' = 3$. The remaining beam is again splitted into two and each passes through a AOM double-pass configuration which shift the frequency of about 200MHz. One beam is with a tunable detuning $\sim$ 20MHz and sent to the slave laser as a seed. Another beam is on resonance and used for absorption imaging. The output light from the slave laser is split into three beam and guided to the optical fibers. The repump laser has a similar configuration, except that the output frequency is near 384.23468THz, the AOMs are single-passed, and the two splitting beams are used for repumping and optical pumping.

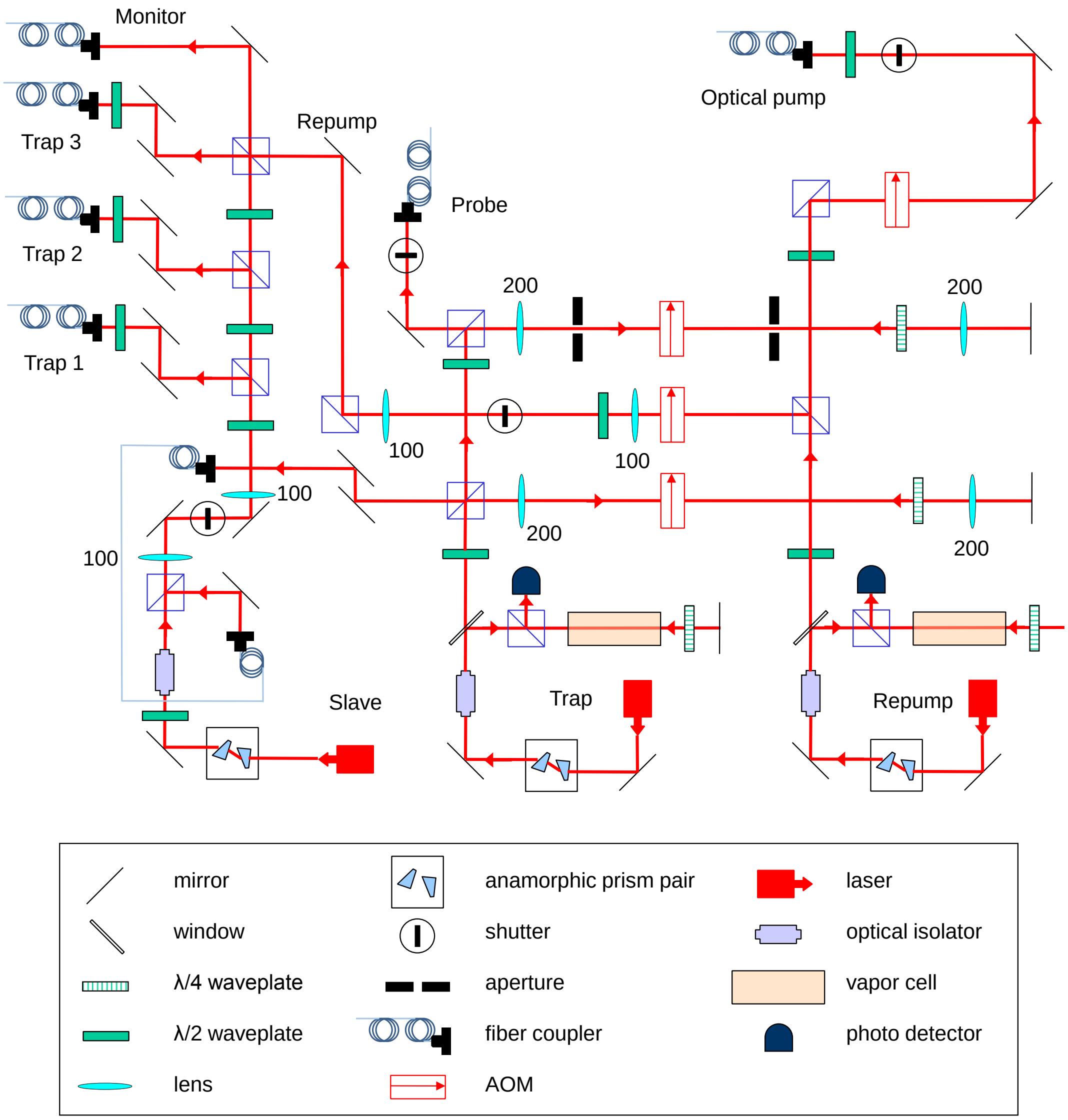

Figure 4.5: Optical layout for Rb laser system. The 780nm laser lights are generated from diode lasers and sent to fibers for laser cooling and trapping. The focal lengths of each lens are indicated.

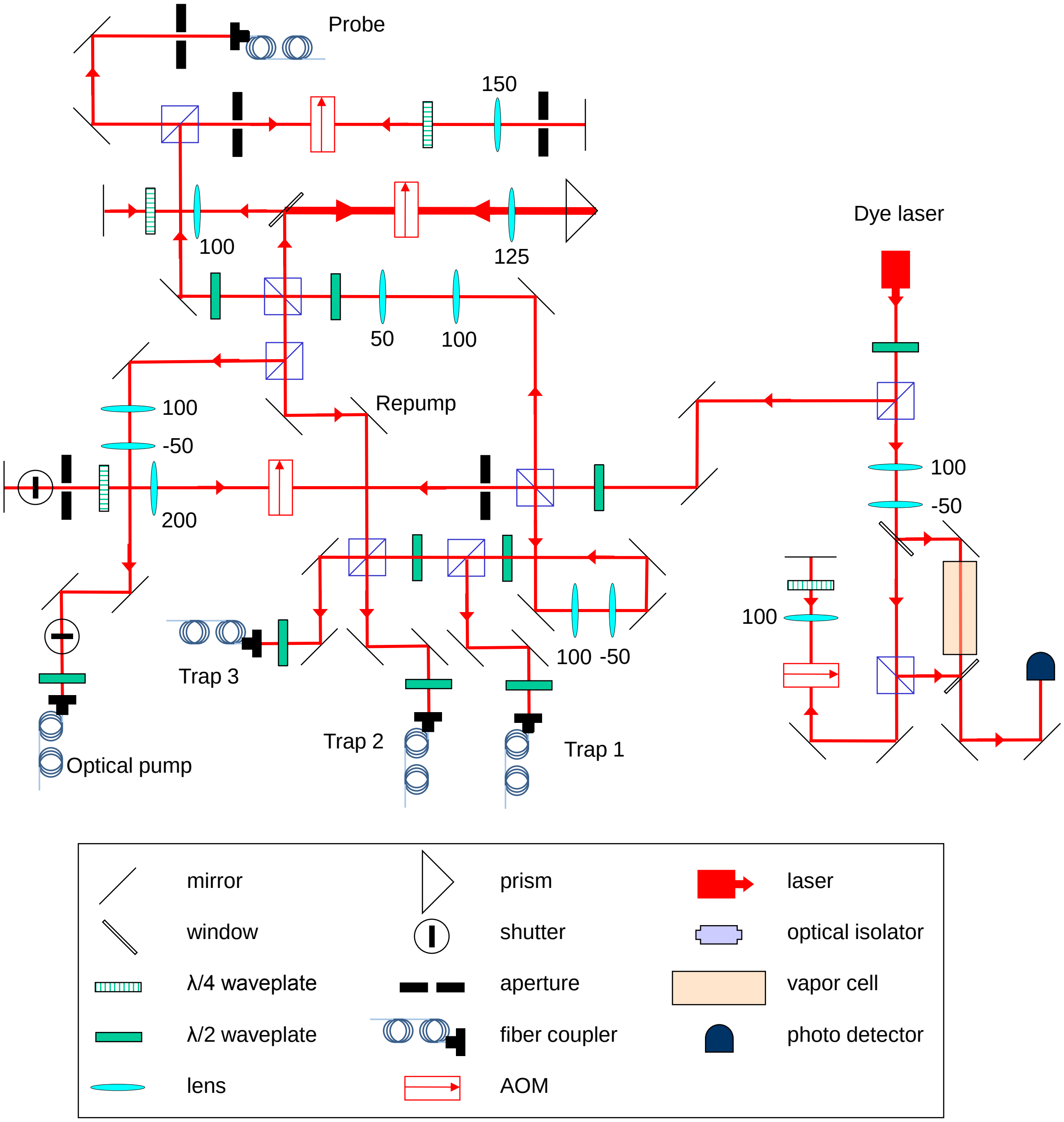

Figure 4.6: Optical layout for Na laser system. The 589nm laser light is generated from the dye laser.

Laser frequency stabilization

An important purpose of the optical layout is to lock the laser frequency through saturated absorption spectroscopy and frequency modulation spectroscopy. The former enables us to resolve the hyperfine structures of the atomic transitions, and the latter enables us to extract the error signal through modulation and provide feedback to lock the laser. The details of the spectroscopy methods can be found in excellent monographs [100]. The main idea of saturated absorption spectroscopy is to used an strong counterpropagating beam overlapping the probe beam to reduce the absorption at the peaks of hyperfine transitions, hence solving the problem of Doppler broadening of the absorption profile of probe beam.

After we get the spectral profile $I(\nu)$, we can modulate the laser frequency (e.g., by driving current modulation) so that the signal becomes $I(\nu + A\sin(\omega t))$, where A and ω are the modulation amplitude and frequency. When A is very small, the Taylor expansion of the signal is a DC term plus a leading AC term:

$$I(\nu + A\sin(\omega t)) \approx \mathrm{DCterm} + A\sin(\omega t)\,\frac{dI}{d\nu}. \tag{4.1}$$

The AC part of this signal is sent through a frequency mixer, in which it is multiplied by another AC signal $B\sin(\omega t + \phi)$ with amplitude B and tunable phase ϕ. The output is

$$A\frac{dI}{d\nu}\sin(\omega t + \phi)\cdot B\sin(\omega t + \phi) = \frac{AB}{2}\frac{dI}{d\nu}\left(\cos\phi - \cos(2\omega t)\right). \tag{4.2}$$

Finally by passing the signal through a low-pass filter, we can extract the first term at the right hand side of Eq. 4.2, which is a DC signal proportional to $dI/d\nu$. This is exactly the error signal we need: it is zero at the resonance position, positive at one side and negative at another side. The schematic diagram for saturated absorption spectroscopy and frequency modulation spectroscopy and corresponding signals for Rb are shown in Fig. 4.7. For Na, the configuration is similar, except that the modulation is on the AOM driving frequency, and the Na cell needs to heat up to ~150°C due to lower saturated vapor pressure.

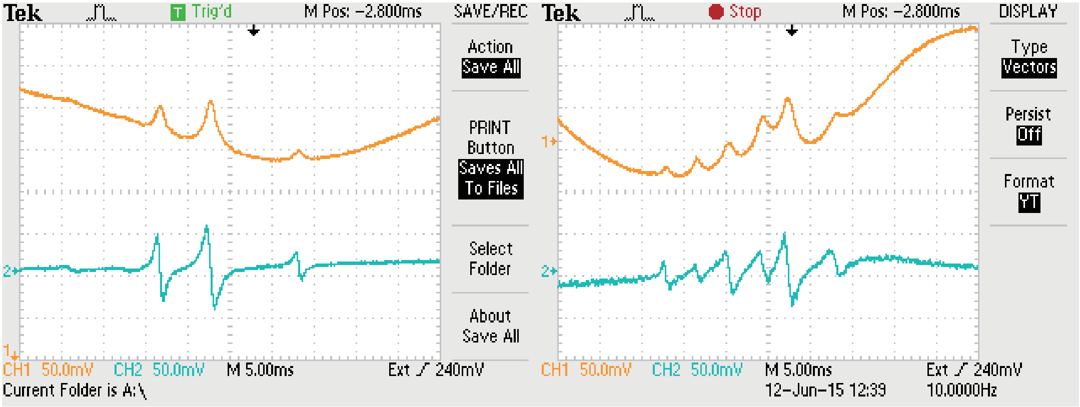

M Pos: −2.800ms
CH1 50.0mV CH2 50.0mV M 5.00ms Ext ⁄ 240mV
Current Folder is A:\
M Pos: −2.800ms
CH1 50.0mV CH2 50.0mV M 5.00ms Ext ⁄ 240mV
12-Jun-15 12:39 10.0000Hz

Figure 4.7: Rb saturated absorption spectroscopy. Left: Hyperfine transitions from $F = 2$ to F', to generate trapping light. Right: Hyperfine transitions from $F = 1$ to F', to generate repumping light. Upper orange curves are the saturated aborption peaks resolving hyperfine structure, while lower green curves are their first-order derivatives obtained by frequency modulation spectroscopy and serve as error signals. Captured by oscilloscope Tektronix TBS1064.

4.1.4 Magnetic Fields

Two kinds of magnetic fields are widely used in the cold atom experiment: the uniform magnetic field and magnetic gradient field. The former is produced by a pair of Helmholtz coil while the latter can be produced by a pair of anti-Helmhotz coil. In our lab, there are totally five pairs of coils: The first one is a pair of Helmholtz coils producing uniform magnetic field as large as 1000G. Each coil is winded by 70 turns of refrigerator copper tube with 4mm diameter, 10 turns at each of the 7 layers. An inductance of $\sim 650\mu$H is estimated. The copper tube is hollow and there is water running through the coil from the water cooling system. The power supply (Delta Elektronika SM30-200) can provide maximum current of 200A and usually it is working at constant voltage mode. The magnetic field is controlled and stabilized by a electronic feedback servo. In the control system the sensor is a current transducer (LEM IT200-S) and the controller is the MOSFET (IXFN230N10). The relative stability of the magnetic field can reach 3×10^{-5}. This pais of coils is used in providing high magnetic field

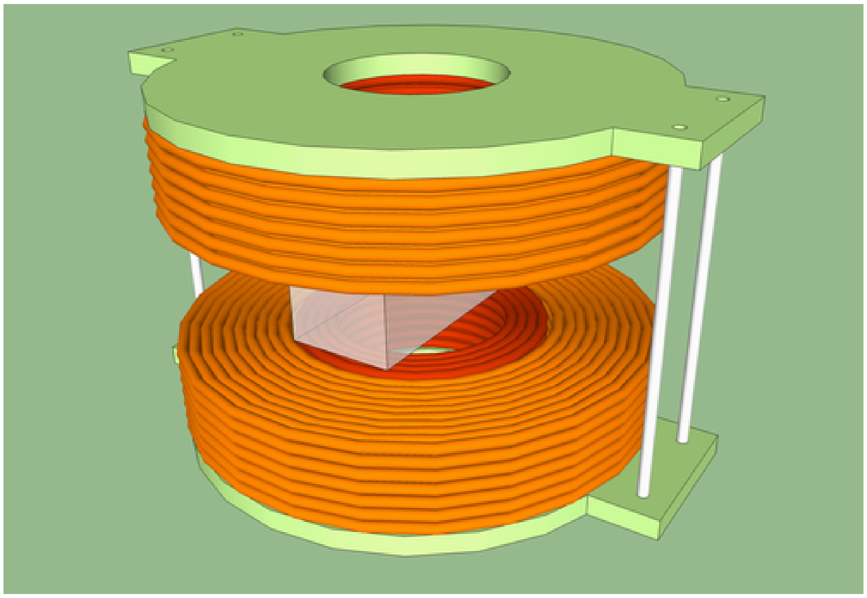

Figure 4.8: Sketch showing the configuration of the two set of coils. The outer pair is the Helmholtz coil producing uniform magnetic field up to 1000G. The inner one is the anti-Helmholtz coil producing magnetic gradient field for magnetic trapping as well as for MOT. The glass cell and the mount for the coils are also shown.

in finding Feshbach resonances and producing Feshbach molecules. The second pair is anti-Helmholtz coils which are used to provide magnetic gradient field in MOT stage as well as act as magnetic quadrupole trap. Each coil has 4 turns at each of the 7 layers. In the magnetic trapping stage, the coils produces 160G/cm magnetic gradient field at the current of 147A, while in MOT stage about 10G/cm is produced. The appearance of these two pair of coils and the mount is shown in Fig. 4.8. More detailed descriptions of the magnetic field system including the performance of the feed back control can be found in the thesis of another member Fudong Wang in our group.

The other three pairs of coils are used to compensate the earth magnetic field in three directions, as well as to provide quantization field for spinor gases in optical trap. They are winded by 50-60 turns of copper wires of 1mm diameter to rectangular shapes. Using the power supplies (ISO-TECH IPS 303DD), the uniform magnetic field can be generated up to 3G. The fluctuation of the magnetic field is less than 0.2mG without feedback servos, according to an experiment testing the stability of population transfer between hyperfine states.

4.1.5 RF and Microwave Devices

High frequency electronics are used in several places in our experiments, includes: (1) 50Hz PZT ramping and 50kHz modulation signal in the laser locking system; (2) 70-400MHz AC currents driving the AOMs; (3) RF electromagnetic field of several kHz to several MHz coupling the Zeeman sublevels in the same hyperfine manifold for Rb and Na; (4) Microwave electromagnetic field of 6.8GHz and 1.7GHz coupling the Zeeman sublevels in different hypfer manifolds for Rb and Na, respectively.

In dealing with high frequency electronics, the conducting wires are replaced by coaxial cables with BNC or SMA connector, and the high frequency components such as oscillator, mixer, switch, RF amplifier, antenna are used. For frequency less than 20MHz, the signal generator Rigol DG1022 works well. For higher frequency, the signal are generated by the generators (SRS SG386 and APSIN6000). The RF antennas are simply copper wire of a few turns. The microwave antenna we used in evaporative cooling in magnetic trap is the horn antenna (Ocean microwave OLB-112-20) which is placed about 10cm away from the atoms.

4.1.6 Computer Control

All the components described above has a certain time sequences in a single experiment run, from turning on the magnetic field and light for MOT, to the time of flight of an atomic cloud in optical trap. The sequence is precisely controlled by computers through PCI card (NI PCI-6733). The PCI card provides both digital (transistor-transistor logic, TTL) and analog (digital to analog converter, DAC) outputs, with the resolution of 16bits. The whole time sequence is constructed and modified in labview programs. The communication between the SRS signal generator and computer is through GPIB interface (NI GPIB-USB-HS). As an illustration, Fig. 4.14 shows a typical experimental sequence for producing an ultracold mixture in ODT.

4.2 Properties of atomic cloud in traps

In cold atom experiments, the atoms are contained in atom traps, hence the density distribution has spatial dependence. This is in contrast with conventional condensed matter system where usually uniform system is considered. The description of atomic cloud is therefore more subtle. The equilibrium properties of atoms in trap at finite temperature and zero temperature are well studied. Here we summarize these properties which are very useful in real experiments to characterize the atomic cloud. We can discuss three cases according to the temperature regimes: (1) Thermal clould ($T \gg T_c$, T_c is the transition temperature); (2) Quantum degeneracy ($T = 0$); (3) Near degeneracy ($T \sim T_c$).

Thermal cloud

The starting point is the classical Hamiltonian of an atom in the trapping potential $U(\mathbf{r})$

$$\begin{aligned} H(\mathbf{r},\mathbf{p}) &= \frac{p^2}{2m} + U(x,y,z) \\ &= \frac{p_x^2 + p_y^2 + p_z^2}{2m} + \frac{1}{2} m \left(\omega_x^2 x^2 + \omega_y^2 y^2 + \omega_z^2 z^2\right). \end{aligned} \tag{4.3}$$

The distribution function is assumed to be Boltzmann distribution for thermal gas at temperature T

$$f = \frac{1}{e^{-\frac{\mu - H}{kT}} + 0}, \tag{4.4}$$

so that the probability of the atom appears in $d^3\mathbf{r}d^3\mathbf{p}$ in phase space is given by $fd^3\mathbf{r}d^3\mathbf{p}/h^3$, μ is the normalization constant (chemical potential) keep the total probability to 1, or N in the case of N non-interacting atoms. In the latter case, the spatial density is given by

$$\begin{aligned} n\left(x,y,z\right) &= \frac{1}{h^3}\int fd^3\mathbf{p} \\ &= N\left(\frac{m\bar{\omega}^2}{2\pi kT}\right)^{\frac{3}{2}}\exp\left[-\frac{m\left(\omega_x^2x^2+\omega_y^2x^2+\omega_z^2x^2\right)}{2kT}\right], \end{aligned} \tag{4.5}$$

in which the chemical potential satisfy $\exp\left(\mu/kT\right) = N(h\bar{\omega}/2\pi kT)^3$. A useful form of Eq. 4.5 is written in terms of atom sizes

$$n\left(x,y,z\right) = n_{\mathrm{p}}\exp\left[-\frac{x^2}{2\sigma_x^2}-\frac{y^2}{2\sigma_y^2}-\frac{z^2}{2\sigma_z^2}\right], \tag{4.6}$$

where the rms size σ_x, σ_y, σ_z and the peak density n_{p} are

$$\sigma_i = \sqrt{\frac{kT}{m\omega_i^2}}, \left(i = x,y,z\right), \tag{4.7}$$

$$n_{\mathrm{p}} = \frac{N}{(2\pi)^{\frac{3}{2}}\sigma_x\sigma_y\sigma_z} = N\left(\frac{m\bar{\omega}^2}{2\pi kT}\right)^{\frac{3}{2}}. \tag{4.8}$$

In practise, only the column density, i.e., the density integrated along z direction is detected. In this case,

$$\tilde{n}\left(x,y\right) = \int n\left(x,y,z\right)dz = \frac{N}{2\pi\sigma_x\sigma_y}\exp\left[-\frac{x^2}{2\sigma_x^2}-\frac{y^2}{2\sigma_y^2}\right], \tag{4.9}$$

In the case of time-of-flight, the atomic cloud is allowed to free expand for time t, then the distribution function $f_t\left(\mathbf{r},\mathbf{p},t\right)$ has the following relation with the distribution function $f\left(\mathbf{r},\mathbf{p}\right)$ at zero time

$$f_t\left(\mathbf{r},\mathbf{p},t\right)=\int f\left(\mathbf{r}_0,\mathbf{p}\right)\delta^3\left(\mathbf{r}-\mathbf{r}_0-\frac{\mathbf{p}t}{m}\right)d^3\mathbf{r}_0. \tag{4.10}$$

Hence the spatial density distribution at time t is given by

$$\begin{aligned}n_t\left(x,y,z,t\right)&=\frac{1}{h^3}\int f_t\left(\mathbf{r},\mathbf{p},t\right)d^3\mathbf{p}\\&=n_{\mathrm{p}}\left(t\right)\exp\left[-\frac{x^2}{2\sigma_x^2\left(t\right)}-\frac{y^2}{2\sigma_y^2\left(t\right)}-\frac{z^2}{2\sigma_z^2\left(t\right)}\right],\end{aligned} \tag{4.11}$$

where the size and peak density at time t are given by

$$\sigma_i\left(t\right)=\sigma_i\sqrt{1+\omega_i^2t^2} \tag{4.12}$$

$$n_{\mathrm{p}}\left(t\right)=\frac{N}{\left(2\pi\right)^{\frac{3}{2}}\sigma_x\left(t\right)\sigma_y\left(t\right)\sigma_z\left(t\right)}. \tag{4.13}$$

Similarly the column density is

$$\tilde{n}_t\left(x,y,t\right)=\frac{N}{2\pi\sigma_x\left(t\right)\sigma_y\left(t\right)}\exp\left[-\frac{x^2}{2\sigma_x^2\left(t\right)}-\frac{y^2}{2\sigma_y^2\left(t\right)}\right], \tag{4.14}$$

which can be used directly to fit the absorption image recorded by CCD.

Quantum degenerate gas

At absolute zero temperature, the atomic gas is quantum degenerate. In the case of Boson, all atoms are condensed to the lowest energy state. In the mean field level and strong interaction limit, the density distribution is given by the solution of GP equation neglecting the kinetic energy term

$$n\left(x,y,z\right)=\frac{15}{8\pi}\frac{N}{R_xR_yR_z}\max\left[1-\frac{x^2}{R_x^2}-\frac{y^2}{R_y^2}-\frac{z^2}{R_z^2},0\right], \tag{4.15}$$

where R_i are the Thomas-Fermi radii

$$R_i = \sqrt{\frac{2\mu}{m\omega_i^2}}, (i = x, y, z), \tag{4.16}$$

in which the chemical potential is

$$\mu = \left(\frac{15\hbar^2 m^{\frac{1}{2}}}{2^{\frac{5}{2}}} N\bar{\omega}^2 a \right)^{\frac{2}{5}}. \tag{4.17}$$

The column density is calculated to be

$$\tilde{n}(x, y) = \frac{5}{2\pi} \frac{N}{R_x R_y} \max \left[1 - \frac{x^2}{R_x^2} - \frac{y^2}{R_y^2}, 0 \right]^{\frac{3}{2}}. \tag{4.18}$$

For BEC at time-of-flight, there is no analytical expression, but it turns out that the density distribution is still keep in parabolic shape, hence one can assume $R_i(t) = \lambda_i(t) R_i$, where λ_i are the time varying factors and put them into the GP equation for numerical solutions. The above distributions are still applicable at time t except that R_i are replaced by $R_i(t)$.

Near degenerate gas

When the temperature approaches the transition temperature, Bose-Einstein statistics become significant. The distribution function eq. 4.4 should change to the Bose distribution function

$$f = \frac{1}{e^{-\frac{\mu - H}{kT}} - 1}. \tag{4.19}$$

Integration over momentum space gives the spatial density distribution

$$n(x, y, z) = \frac{1}{\lambda_{\mathrm{dB}}^3} g_{3/2} \left(z \exp \left[-\frac{x^2}{2\sigma_x^2} - \frac{y^2}{2\sigma_y^2} - \frac{z^2}{2\sigma_z^2} \right] \right), \tag{4.20}$$

where $\lambda_{\mathrm{dB}} = h/\sqrt{2\pi mkT}$ is the thermal de Broglie wavelength, atom sizes σ_i have the same form with Eq. 4.7. $z = \exp\left(\mu/kT\right)$ is the fugacity which can be determined from the condition

$$N = \left(\frac{kT}{\hbar\bar{\omega}}\right)^3 g_3\left(z\right), \tag{4.21}$$

and the Riemann Zeta function $g_l(z)$ is

$$g_l\left(z\right) = \sum_{j=1}^{\infty} \frac{z^j}{j^l}. \tag{4.22}$$

The column density is given by

$$\tilde{n}\left(x,y\right) = \frac{1}{\lambda_{\mathrm{dB}}^3}\sqrt{2\pi}\sigma_z g_2\left(z\exp\left[-\frac{x^2}{2\sigma_x^2} - \frac{y^2}{2\sigma_y^2}\right]\right). \tag{4.23}$$

For time-of-fight, the above density distribution functions are valid when the size σ_i are replaced by the sizes $\sigma_i(t)$ at time t, and the relation between these two sizes is still given by Eq. 4.12.

4.3 Detection of atoms

4.3.1 Absorption Imaging

The detection method of the atomic cloud is the well established absorption imaging. It enables us to detect the spatial density profile by recording the absorption of the resonant light by a CCD. When a light beam which size is larger than the atomic cloud and on resonant with the atomic cycling transition pass through the atom sample, the intensity will have an exponential decay. According to Beer's law,

$$\frac{dI\left(x,y,z\right)}{dz} = -\sigma_{eg} n\left(x,y,z\right) I\left(x,y,z\right), \tag{4.24}$$

where $I(x, y, z)$ is the light intensity, σ_{eg} is the resonant absorption cross section, $n(x, y, z)$ is the atomic cloud density. Integration of the equation along z gives the intensity profile of the output light $I(x, y)$ relative to the input light $I_0(x, y)$

$$I\left(x,y\right)=I_0\left(x,y\right)\exp\left[-\sigma_{eg}\int n\left(x,y,z\right)dz\right], \tag{4.25}$$

hence the column density is given by

$$\tilde{n}\left(x,y\right)=\frac{1}{\sigma_{eg}}\ln\left(\frac{I_0}{I}\right). \tag{4.26}$$

In practise, $I(x, y)$ is recorded by a CCD (pco.pixelfly usb) for a short duration ($100\mu s$), hence the total counts which proportional to the photon number for each pixel is recorded. However, the background light is recorded together with the probe light. So the procedure is as follow: we first record a counts profile on the CCD $S(x, y)$ with probe light passes through the atom at time-of-flight, then after 700ms a second counts profile $S_1(x, y)$ is recorded with the same intensity and duration of the light (the atoms are absent), finally after 700ms a third profile $S_0(x, y)$ is recorded without probe light and atom. The column density is there for

$$\tilde{n}\left(x,y\right)=\frac{1}{\sigma_{eg}}\ln\left(\frac{S_1\left(x,y\right)-S_0\left(x,y\right)}{S\left(x,y\right)-S_0\left(x,y\right)}\right). \tag{4.27}$$

An example of the four profiles $S(x, y)$, $S_1(x, y)$, $S_0(x, y)$ and $\sigma_{eg}\tilde{n}(x, y)$ are shown in Fig. 4.9.

4.3.2 Measuring the physical quantities

Atom number

Since we have get the column density profile on the CCD, the total atom number can be calculated by integration of the density. Considering the discrete nature of the profile composed of pixels of sizes A and magnification M of the image

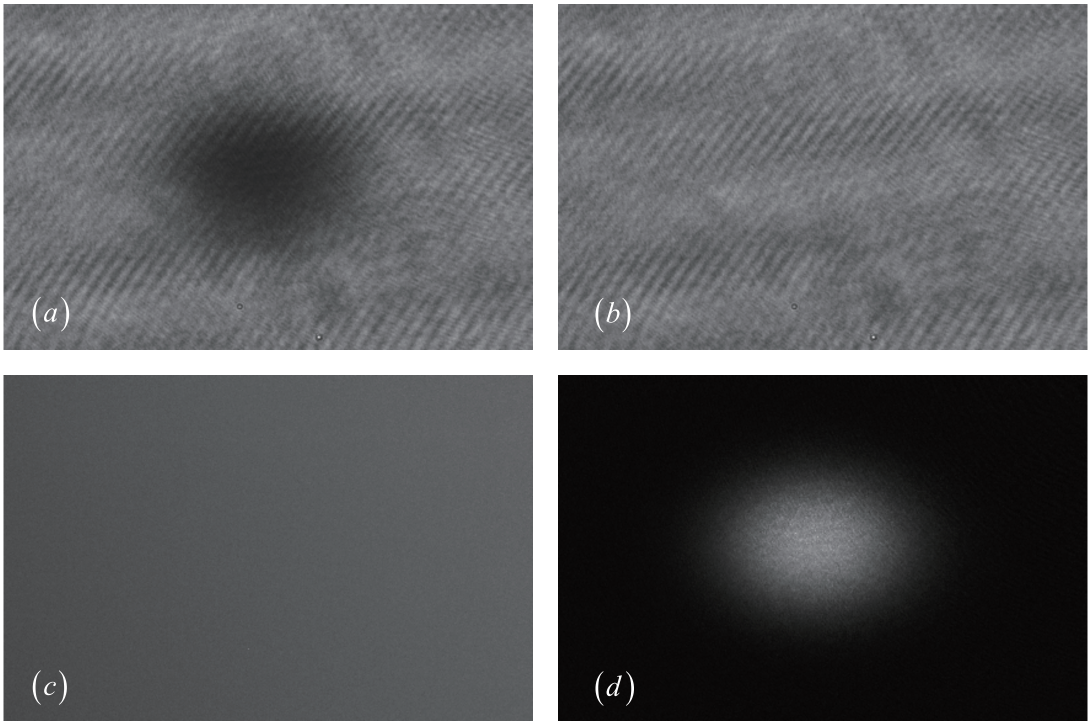

Figure 4.9: An example of the absorption images. (a) $S(x,y)$, in the presence of probe beam and atoms; (b) $S_1(x,y)$, in the presence of probe beam but without atoms; (c) $S_0(x,y)$, without probe beam and atoms; (d) $\sigma_{eg}\tilde{n}(x,y)$ calculated optical density (See text).

system, the integration is replaced by summation

$$N = \frac{A}{M^2\sigma_{eg}} \sum_i \ln\left(\frac{s_{1,i} - s_{0,i}}{s_i - s_{0,i}}\right), \tag{4.28}$$

here the summation is over all pixels on the CCD, s_i is the counts on i-th pixel corresponds to the S_i profile. A more practical approach is when we know that the atomic cloud has known profile, we can fit the distribution using the corresponding function and integrate. If a thermal cloud is expanded from a harmonic trap, the distribution has gaussian form and can be fit using Eq. 4.14, and the total number can be expressed in terms of the fitting parameters $p = \tilde{n}_p\left(x,y\right)\sigma_{eg}$ and σ_x, σ_y

$$N = \frac{A}{M^2\sigma_{eg}} 2\pi p \sigma_x \sigma_y. \tag{4.29}$$

In the case of BEC,

$$N = \frac{A}{M^2 \sigma_{eg}} \frac{2\pi}{5} p R_x R_y. \tag{4.30}$$

Atom density

The CCD records the column density distribution at time t, to calculate the initial density profile, the trap frequencies $(\omega_x, \omega_y, \omega_z)$ must be considered. The peak density at $t = 0$ for gaussian profile is calculated to be

$$n_{\mathrm{p}} = \frac{M}{\sigma_{eg}\sqrt{2\pi A}} \left(1 + \omega_x^2 t^2\right)^{\frac{3}{4}} \left(1 + \omega_y^2 t^2\right)^{\frac{3}{4}} \frac{\omega_z}{\sqrt{\omega_x \omega_y}} \frac{p}{\sqrt{\sigma_x \sigma_y}}. \tag{4.31}$$

The average density is given by

$$\langle n \rangle = \frac{\int n^2 \left(x, y, z\right) d^3\mathbf{r}}{N} = \frac{n_{\mathrm{p}}}{\sqrt{8}}. \tag{4.32}$$

Temperature

The measurement of temperature is straightforward if the trap frequencies are known. Combining Eq. 4.7 and Eq. 4.12 we can get the temperature from the sizes at time t

$$T = \frac{m}{k} \frac{\omega_i^2 \sigma_i^2 \left(t\right)}{1 + \omega_i^2 t^2}. \tag{4.33}$$

If the trap frequency are unknown, the temperature can be obtained by the widely used time-of-flight method: the above equation can be rewritten as

$$\sigma_i^2 \left(t\right) = \sigma_i^2 + \frac{kT}{m} t^2, \tag{4.34}$$

thus by measuring the sizes at different t, the data can be used to fit the above function using σ_i and T as free parameters. Fig. 4.10 shows such a measurement for Rb thermal cloud in ODT.

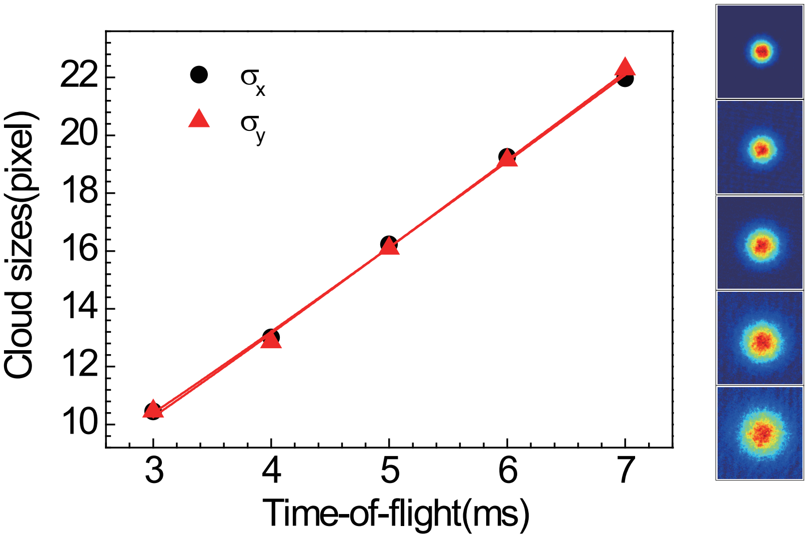

Figure 4.10: Measurement of the temperature of Rb thermal cloud in ODT. The atoms are released from the trap and allowed to expand for 3 to 7ms, and the cloud sizes are measured by absorption imaging. By fitting the sizes at different time using Eq. 4.34, the temperature is determined to be 900nK. The right panel shows the absorption images at 3 to 7ms from up to down.

Phase space density

Phase space density is a characterization of atom number occupying a single atom state. It is given by

$$D = n\lambda_{\mathrm{dB}}^3. \tag{4.35}$$

Hence it can be calculated after measuring the density and temperature. An useful expression is that for trapped atomic gases, from Eq. 4.8, the peak phase space density is given by

$$D_{\mathrm{p}} = N\left(\frac{\hbar\bar{\omega}^2}{2\pi kT}\right)^3. \tag{4.36}$$

4.3.3 Atom Number Calibration

The detection of atom density (hence atom number) described above is under some assumptions. The intensity of the probe light is assumed to be weak compared to the saturated intensity, the light has perfect polarization and propagation direction along the quantization field, the atoms are always in the cycling transition. However, imperfection is unavoidable and leads to deviation of the detected atom number. Particularly this is important in determining the mean field shift in a BEC which is proportional to the atom density. To take into account these effects, Eq. 4.24 should be modified by considering the saturated effect and assuming an effective intensity [101, 102]

$$\begin{aligned} \frac{dI\left(x,y,z\right)}{dz} &= -\sigma_{eg} n\left(x,y,z\right)\frac{I_{\text{eff}}}{1+I_{\text{eff}}/I_s} \\ &= -\sigma_{eg} n\left(x,y,z\right)\frac{I/\alpha}{1+I/\alpha I_s}, \end{aligned} \tag{4.37}$$

where we have assumed $I_{\text{eff}} = I/\alpha$. Integration along z axis gives

$$\begin{aligned} \sigma_{eg}\tilde{n} &= -\alpha \ln\left(\frac{I}{I_0}\right) + \frac{I_0 - I}{I_s} \\ &= \alpha\delta + \frac{I_0}{I_s}\left(1 - e^{-\delta}\right), \end{aligned} \tag{4.38}$$

where δ is the directly measurable optical density. Integration over the $x - y$ plane gives

$$\frac{I_0}{I_s}\int\left(1 - e^{-\delta}\right)dxdy = -\alpha\int \delta dxdy + \sigma_{eg}N. \tag{4.39}$$

This is an equation of the form $y = -\alpha x + \sigma_{eg}N$ where $y = \frac{I_0}{I_s}\int\left(1 - e^{-\delta}\right)dxdy$ and $x = \int \delta dxdy$. By measuring a set of (x_i, y_i), the correction factor α can be obtained from the linear fitting. Experimentally this is done by preparing atomic clouds at the same condition, but using probe light with different intensities. The intensity can be measured and (x_i, y_i) can be obtained by assuming δ has gaussian profile or doing direct summation. The number correction result for Rb is shown in Fig. 4.11 where $\alpha \approx 2$. For Na we also do similar measurement but the correction α is found to be near 1 in our system.

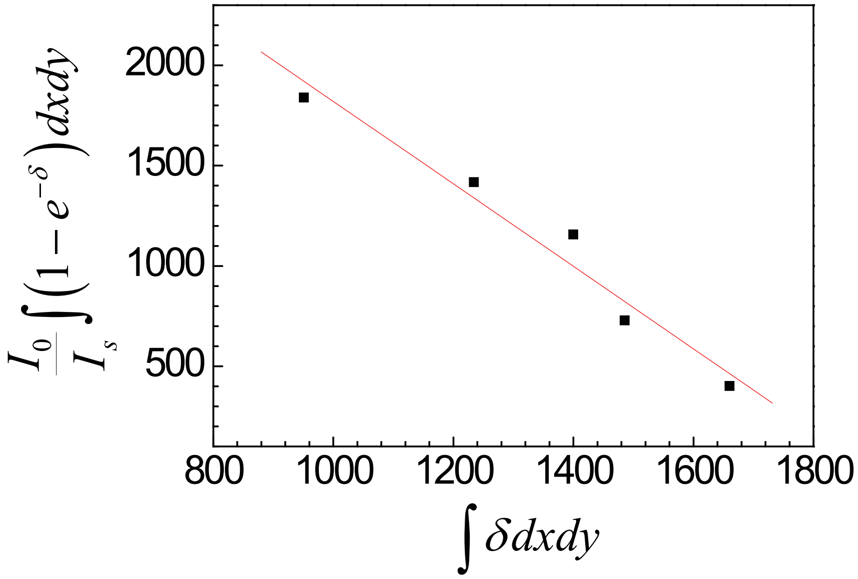

Figure 4.11: Number calibration of Rb atoms. The data are obtained by using different probe beam intensities for the atomic cloud prepared in the same conditions, and calculating the corresponding (x_i, y_i) (See text). The calibration factor is determined to be $\alpha = 2.0 \pm 0.2$ from the linear fitting (red line).

4.4 Achievements on the setup

In this section a brief introduction of the works on the setup is described previous to the spinor dynamics experiments. The main subject is to produce an ultracold mixture of Rb and Na towards the ground-state NaRb molecule in our simple and compact setup.

4.4.1 Rb BEC in a Hybrid Trap

After laser cooling in MOT, CMOT and Molasses stage, we have 3×10^8 Rb atoms at temperature of about 20μK. The atoms are then pumped to the hyperfine level $|F = 1, m_F = -1\rangle$ by a 1ms optical pumping pulse and transfer to the magnetic quadrupole trap with axial gradient field of 160G/cm. Then we apply the microwave field for evaporative cooling. The microwave frequency start at

6774MHz and the slope is optimized in different time segments to achieve highest cooling efficiency. Down to 6822MHz, the Majorana loss become severe and we solve the problem by applying an 1070nm optical beam displaced 150μm away from the QT center vertically, as shown in Fig. 4.12. Thus the atoms stay in the potential in the hybrid trap rather than the QT center. After further evaporative cooling in the hybrid trap to 6832MHz, the QT is ramped off and the atoms are transfer to the cross ODT for final evaporation. A BEC of 2×10^5 atoms can be obtained after 3s of evaporative cooling in ODT.

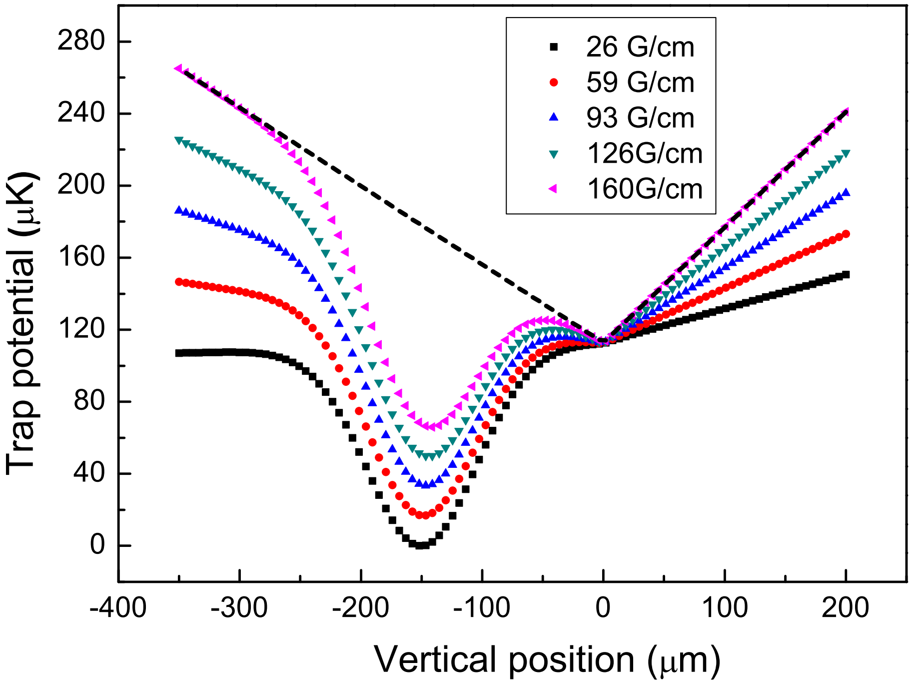

Figure 4.12: Hybrid trap potentials along y (gravity) direction. The optical beam is displaced 150μm below the QT center. The black dashed line is the potential without optical beam and the dotted lines are the overall potential at 26G/cm to 160G/cm with optical beam.

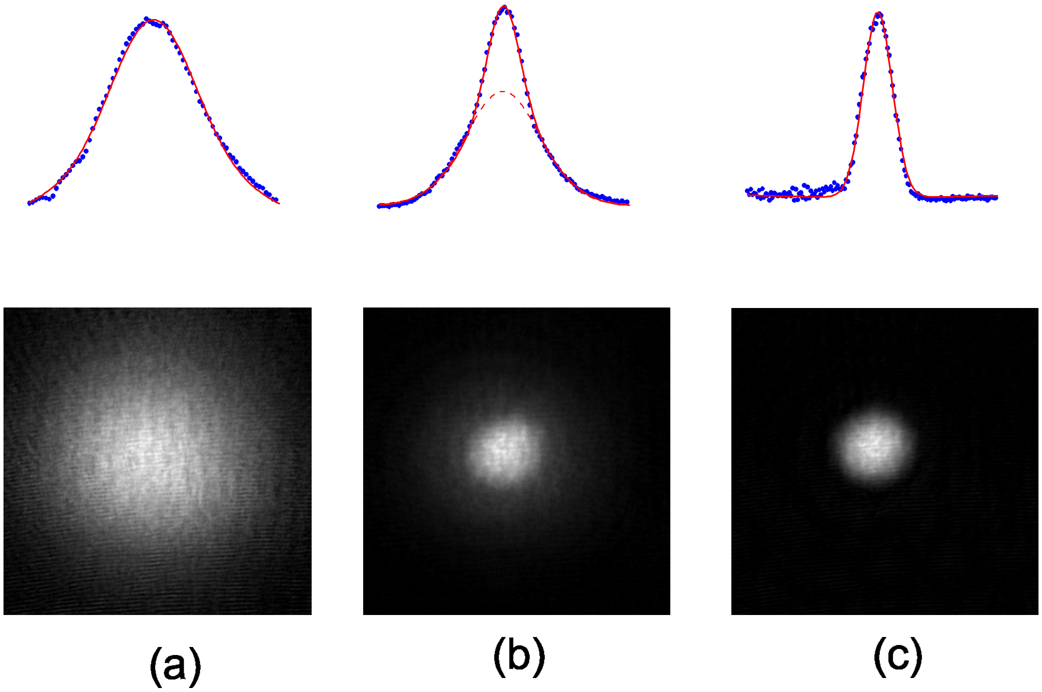

Figure 4.13: Absorption images at 30ms time-of-flight showing the BEC transition of Rb. Lower pannel: absorption images for (a) thermal cloud, (b) partially condensed atomic cloud, (c) quasi-pure BEC. Upper pannel indicate the integrated optical densities and fitting using (a) Gaussian distribution, (b) bimodal distribution (Gaussian + parabola), (c) parabola distribution. The size of the picture is 900μm by 900μm.

4.4.2 Two Species BEC

Since Na has much lower saturated vapor pressure than Rb in the vacuum chamber, the initial atom number in MOT is 5×10^6. It is difficult to get Na BEC by evaporative cooling, hence sympathetic cooling is adopted. In the MOT stage, in order to avoid severe light assisted collision loss, the Rb cloud is displaced away from the Na cloud until optical pumping. The two clouds then overlap in QT. By evaporative cooling of Rb, Na is cooled down through interspecies elastic collisions. The scheme works well due to appropriate interspecies scattering length ($\sim 75a_0$) and relative fast equilibrium.

To optimize the sympathetic cooling process, we try to place the optical beam

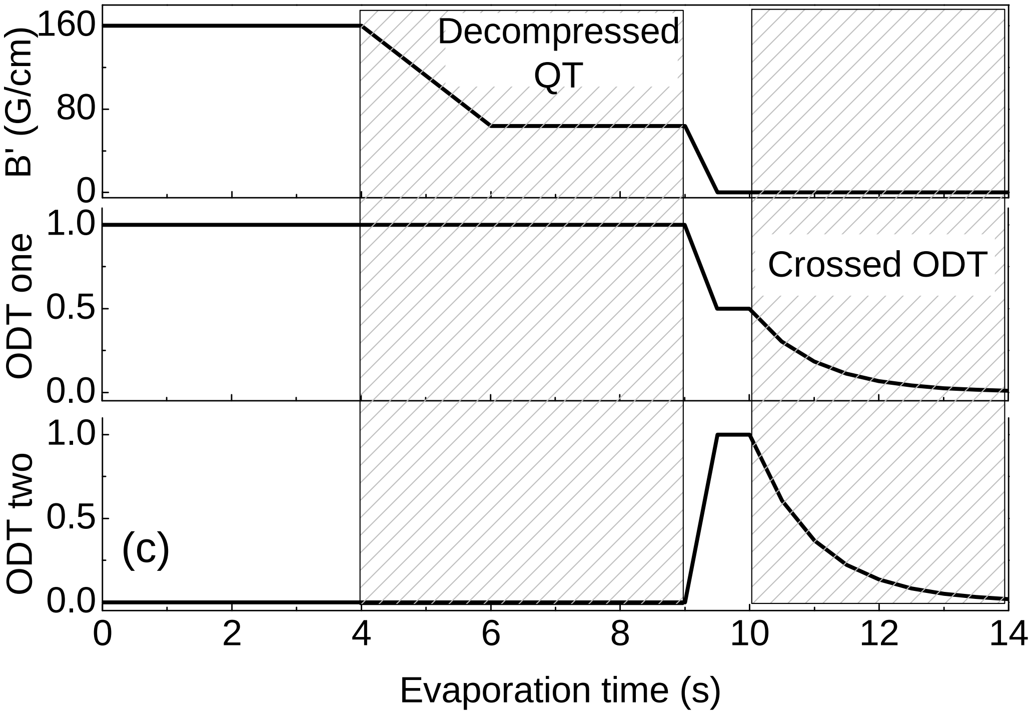

Figure 4.14: Time sequence of QT and cross ODT for producing two species BEC. To optimized the atom number of the BECs, the ODT is displaced 75μm horizontally from the QT center, and a decompress process for QT is found to avoid severe Majorana loss for Na before loading to ODT.

horizontally beside the QT center and find a larger trap depth for Na. Furthermore, when evaporation goes to 6822MHz, the QT is ramped down so that the Majorana loss for Na is suppressed. At the end of microwave evaporation at 6833.75MHz, the two clouds are transfer to ODT. Since Na has a shallower trap depth for Rb, it serves as the coolant in ODT instead. Finally, two BEC with 1×10^5 atoms in each species can be obtained. The number ratio can be tuned by controlling the final microwave frequency. Pure Na BEC of 2×10^5 is achieved when Rb is all removed before loading to ODT. Fig. 4.14 shows the time sequence for obtaining two species BECs and Fig. 4.15 shows the spatial density profile after time-of-flight of the BECs. We can see that a notch in the Na profile indicating the large repulsive interaction of the two BECs, which is consistent with theoretical predictions [31, 32, 84, 85] that when the $g_{12}^2/g_{11}g_{22} > 1$, the two condensates are immiscible. Recently we use Feshbach resonance to change the miscibility of the two BECs [81]

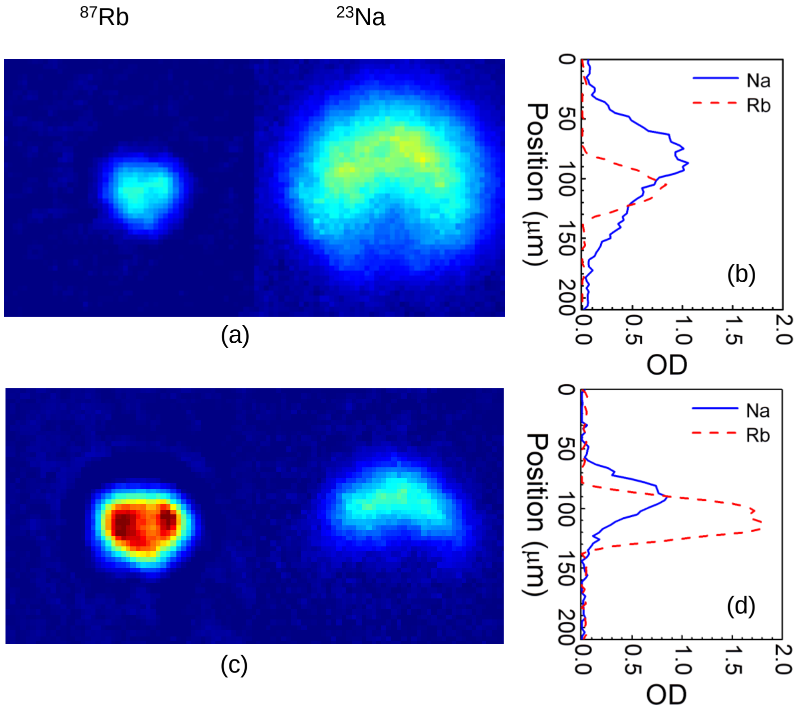

Figure 4.15: Absorption images at 10ms time-of-flight for two species BEC. The immiscibility of the two BECs is clearly seen from the density profiles. (a) 3.5×10^3 atoms for Rb and 3.2×10^4 atoms for Rb. (c)8.5×10^3 atoms for Rb and 1.3×10^4 atoms for Rb. (b) and (d) are the center cross sections along the vertical direction for images in (a) and (c),respectively. The size of the picture is 210μm by 210μm.

4.4.3 Feshbach resonance and Feshbach molecule

After preparing the ultracold mixture of Rb and Na and the high magnetic field Helmholtz coil, We have search the Feshbach resonances between these two species. The method is to prepare the sample in ODT with external magnetic field, and detect the number loss at different magnitudes of the field. Knowing the positions of the resonances enables a precise determination of the interaction strengths between Rb and Na atoms. From all found resonances the interspecies scattering length of Rb and Na is fitted to be $a_{\text{Singlet}} = 106.74a_0$ and $a_{\text{Triplet}} = 68.62a_0$. The Feshbach resonance is also used to produce Feshbach molecules by sweeping the magnetic field across the resonance at 347.7G. We estimate that about 4000 molecules are produced which is ready for transfer to the absolute ground state [103–105] by STIRAP. Details of these experiments can be found in references [106, 107] and one of our group members Fudong Wang's thesis.

Chapter 5

Spin Dynamics in a Spin-1 Mixture

5.1 Introduction

Understanding collective spin dynamics is a problem of fundamental importance in modern many-body physics. Central to this understanding is the role of spin-spin interactions and their interplay with the Zeeman energy. In this regard, the ultracold spinor quantum gas [55, 87] provides a powerful platform due to the high controllability. So far, a rich variety of phenomena have been explored theoretically and experimentally. Here we give a brief review of the studied of coherent spinor dynamics so far.

Coherent dynamics of spinor gases have attracted a great deal of attention since the success of creating a ultracold gas sample in an optical trap where the spin degree of freedom is frozen. In [35, 36], Ho and Ohmi, Machida pioneered the studies of the properties of the spinor gases, including the ground state structure in the absence of magnetic field, collective excitations, and topological defects. The antiferromagnetic interaction of Na is supported by the experiment studying the ground state while the domain formation is observed. Law pioneered the study of dynamics of spinor gases in spin degree of freedom, and pointed out the spin-mixing process that lead to interesting dynamics including the oscillation of spin populations. Pu detailed the study and put forward the mean field coupled GP theory. Their work motivated the search for the coherent dynamics in experiments. The spin-mixing collision were observed and studied in Hamburg and Georgia tech group in 2004. The coherence of the spin-mixing dynamics is evident in later experiment by Chang, where clean sinusoidal oscillations of the spin populations are observed. They attributed the observed behaviors to collisional coherence and pointed out the analog with Josephson oscillation and four wave mixing. Meanwhile, an analytical solution of the mean-field SMA dynamics was found and provided a simple model to describe the experiment, and the competition between mean field energy and Zeeman energy is predicted to produce a resonance of the period and amplitude in the dynamics. The resonance is indeed observed in Rb $F = 2$ spinor gases in Hamburg. Similar coherent dynamics is also found in Na. An interesting aspect of this kind of coherent dynamics is that the directly measurable frequency and amplitude of the oscillation can precisely provide quantitative information about the parameters of the systems. Recently, the study on coherent spinor dynamics has been extended to other spinor systems, including the Na thermal gas, Fermi gas, spinor gases with microwave coupling and in optical lattice.

Until now, however, spin dynamics in ultracold atoms has been explored only in a single atomic species. In this chapter, we decribe the realize of a system consisting of distinguishable spin-1 ^{87}Rb and ^{23}Na atoms, and demonstrate well-controlled and long-lived coherent spin oscillations between them. The study is motivated not only because it is a experimentally assessable new system and being a naturally extension of the study of single species spinor gases, but also because the underlying unique properties and possible applications of the system. There are several unique features of the spinor mixutre. (1) For collisions between two distinguishable spin-1 atoms, the interaction takes place over all possible total spin F channels [35, 36, 57, 108–112], while only even F are allowed for homonuclear collisions. (2) Both the linear and quadratic Zeeman shifts are different for the two species and are thus important for spin dynamics. Only quadratic Zeeman shift plays a role for single species spinor gases due to magnetization conservation [113]. (3) The two species also have very different response to optical field. A differential effective magnetic field can thus be generated with the vector light shift. Together with the external magnetic field, this can be used to further control the spin dynamics. Furthermore, the system can be viewed as a Josephson junction without spatial barrier, and the oscillating current replaced by oscillating spin current. It may find the applications in quantum computing, e.g., as a qubit. Other possible topics based on this system includes entangled BEC, magnetic impurity problems and two orbital-magnetism problem. In this chapter, we concentrate on the coherent spin-mixing dynamics between $F = 1$ Na and Rb spinor gases.

5.2 The Role of Interaction and Magnetic Field

Let us consider the collision between a ^{87}Rb atom in spin state $|m_1\rangle$ and a ^{23}Na atom in spin state $|m_2\rangle$, which we denote as $|m_1, m_2\rangle$ in the following. Here $m = \pm 1, 0$ are the three Zeeman sub-levels of the $f = 1$ hyperfine state. The magnetic energy associated with $|m_1, m_2\rangle$ will be denoted as $E^{m_1,m_2}(B)$. With the interaction between the Rb and Na described by Eq. (3.13), the β and γ terms can support several possible heteronuclear spin-changing processes satisfying the individual species population and total magnetization conservation, as given in (3.38). This is in stark contrast to the homonuclear spin-1 case, where the only allowed spin-changing process is the one between two $|0\rangle$ states, and one in $|-1\rangle$, another one in $|+1\rangle$. In this work, we focus on the following heteronuclear spin-changing process,

$$|0,-1\rangle \leftrightarrow |-1,0\rangle\,, \tag{5.1}$$

which is driven solely by the β term [95].

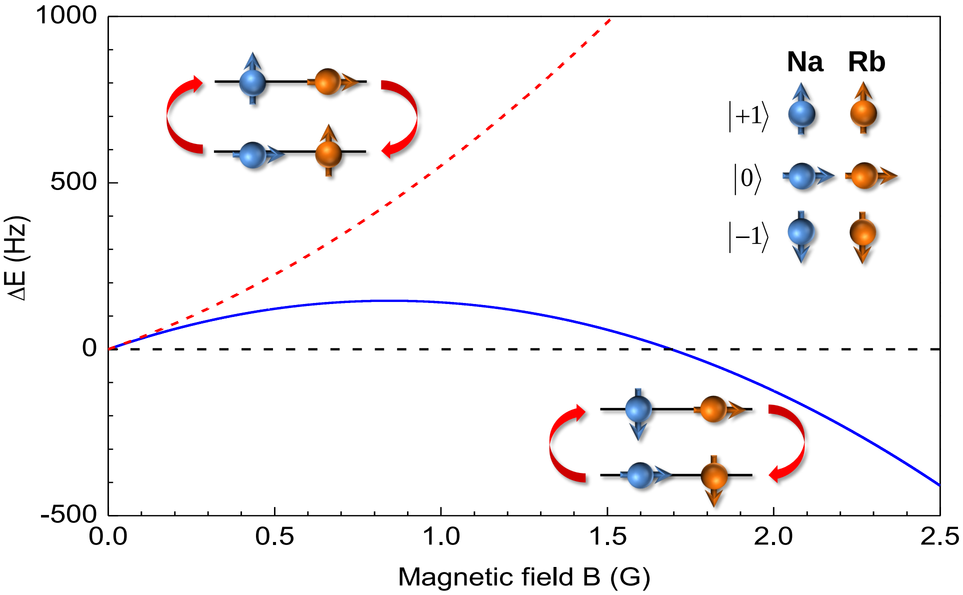

Figure 5.1: (color online) Magnetic energy diagram for two heteronuclear spin-changing processes. For the process in Eq. (5.1), ΔE has a zero-crossing point at $B_0 = 1.69$ G where spin oscillations can happen with large amplitude. Other homonuclear and heteronuclear processes are suppressed.

Intuitively, coherent spin dynamics of Eq. (5.1) can be understood from the interplay between the spin-dependent interaction energy (β term) and the total Zeeman energy difference between these two states: $\Delta E(B) \equiv E^{0,-1}(B) - E^{-1,0}(B)$, as depicted in Fig. 5.1. In analogy to a driven two-level system, when the two energies are very different, the system undergoes fast but small amplitude detuned oscillations, while when they are comparable, the system oscillates slowly with large amplitude [113]. Since β is small, typical spin-dependent mean-field energy is of the order of 10 Hz, and as a result, visible heteronuclear spin oscillations can only occur near $\Delta E = 0$. As shown in Fig. 5.1, ΔE depends on the magnetic field B in a non-monotonic manner, and in particular vanishes at $B_0 = 1.69$ G, where one expects resonant spin dynamics. This coincidence is a result of the slightly different Landé g-factors for ^{23}Na and ^{87}Rb, including contributions from both the linear and the quadratic Zeeman energies. Near B_0, homonuclear spin dynamics is greatly suppressed due to large quadratic Zeeman shifts and the other heteronuclear spin-changing processes are also suppressed due to large detuning. For example, the spin-changing process $|0, 1\rangle \leftrightarrow |1, 0\rangle$ has a magnetic energy difference larger than 1000 Hz and will be substantially suppressed. Thus, working near B_0, we can single out the process in Eq. (5.1) and obtain clear signatures of heteronuclear spin dynamics.

The considerations above offer only a qualitative picture of the inter-species spin dynamics. Experimentally, we use a bulk sample consisting of an essentially pure ^{23}Na BEC and a thermal gas of ^{87}Rb to increase the overlap of the two clouds. This many-body system is distinctively different from the conventional two-level system since spin- and density-dependent mean-field interactions enter nonlinearly into the equations of motion and furthermore, vary in the course of spin dynamics. One of the important consequences is the appearance of two magnetically tuned resonances as we shall discuss momentarily.

5.3 State Preparation

We produce the ultracold mixture of an essentially pure ^{23}Na BEC with 1.0×10^5 atoms and a ^{87}Rb thermal gas with about 6.3×10^4 atoms in a crossed ODT, following the procedure described in [81]. Thermal ^{87}Rb is used here to increase the overlap between two species as double BEC is immiscible [1]. The number imbalance is chosen such that the ^{87}Rb cloud is 100nK above its BEC transition temperature. The final stage of the evaporation is performed in the presence of a 2 G magnetic field to make sure that all atoms are polarized in the $|-1\rangle$

spin state. The final trap frequencies for Rb and Na are $2\pi \times (110, 215, 190)$ Hz and $2\pi \times (98, 190, 168)$ Hz, respectively. The average density is 5.9×10^{13} cm^3 (6.5×10^{12} cm^3) for Na (Rb). Along the vertical direction, the Thomas-Fermi radius of the Na BEC is 7.1μm and the size of the thermal Rb cloud is 5.1μm. There is a differential gravitational sag of about 2.4μm due to the trap frequency difference in the vertical y-direction.

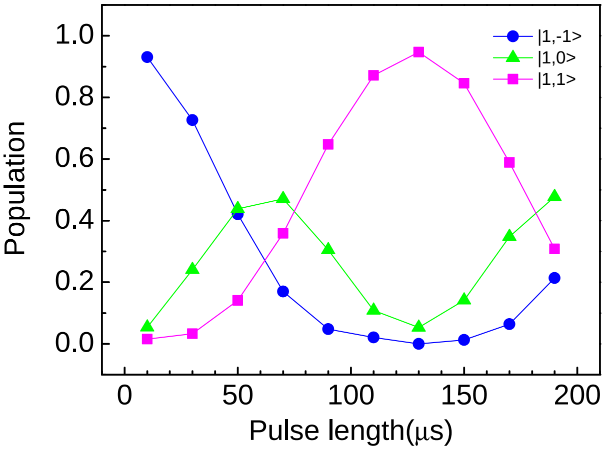

Figure 5.2: Experimental observed Rabi oscillation of $F = 1$ Rb spinor gas in the presence of radio frequency. Blue:$|-1\rangle$, green:$|-1\rangle$, purple:$|-1\rangle$. The power input to the rf coil is -5dBm, produced by the SRS signal generator, and the frequency is 0.722MHz. The solid lines are used to guide eye.

Both ^{23}Na and ^{87}Rb atoms are initially prepared in the spin state $|-1\rangle$ [81, 106]. To initiate the spin oscillations, we apply a radio-frequency (rf) Rabi pulse to simultaneously prepare both Rb and Na in coherent superposition states with most population in $|-1\rangle$ and $|0\rangle$ states, while populations in the $|+1\rangle$ states are typically less than 10%. The radio-frequency is produced by homemade magnetic coil, which magnetic field perpendicular to the bias magnetic field used to provide the quantization axis and maintain the spin state. Starting from the $|-1\rangle$ state, the resonance frequency is calibrated by scanning the rf requency at fixed pulse time smaller than a π-pulse, measuring the population of $|0\rangle$ state and fitting the resulting curve by Gaussian function. Then we fixed the rf frequency at resonance, and change the pulse length so that the Rabi oscillation between the three Zeeman states is oberved, as shown in fig. 5.2. By changing the input power to the coil, we can fix the π-pulse to 30μs, and the initial state is set to the state with 10μs pulse length. According to the calculation (3.9), the initial population is $(\rho_1, \rho_0, \rho_{-1}) = (0.0625, 0.375, 0.5625)$ while the initial relative phase is 0, for both Rb and Na.

5.4 Observation of Coherent Heteronuclear Spin Dynamics

To monitor the spin dynamics, we detect the fractional spin population $\rho^i_m = N^i_m/N^i$ for each species from the absorption images after various holding time. Here N^i_m is the atom number of species i in spin state $|m\rangle$. $N^i = N^i_{-1} + N^i_0 + N^i_{+1}$ is the total number of atoms of species i, with $i = \mathrm{Na}, \mathrm{Rb}$.

Fig. 5.3a and 5.3b show typical time evolution of ρ^{Rb}_m and ρ^{Na}_m at $B = 1.9$ G, respectively. The population in states $|-1\rangle$ and $|0\rangle$ oscillate periodically, while those in state $|1\rangle$ stays nearly constant. It is important to note the following features: (1) States $|-1\rangle$ and $|0\rangle$ of each individual species oscillate with π-phase shift due to number conservation; (2) The synchronized oscillation between the two species reflects the coherent spin dynamics driven by heteronuclear spin-changing interaction. This is even more clearly exhibited in the individual magnetization dynamics. The fractional magnetization for each species is $\mathcal{M}^i = (N^i_{+1} - N^i_{-1})/N^i$. The total magnetization of the system is defined as $\mathcal{M} = (N^{Na}_{+1} - N^{Na}_{-1} + N^{Rb}_{+1} - N^{Rb}_{-1})/N$, where $N = \sum_i N^i$ is the total number of atoms. As shown in Fig. 5.3c, 5.3d and the inset, $\mathcal{M}^{\mathrm{Na}}$ and $\mathcal{M}^{\mathrm{Rb}}$ are not conserved, but $\mathcal{M}$ is conserved within a few percent. The small variation in $\mathcal{M}$ is comparable to the uncertainties ($\sim 5\%$) in atom number detection. The coherent

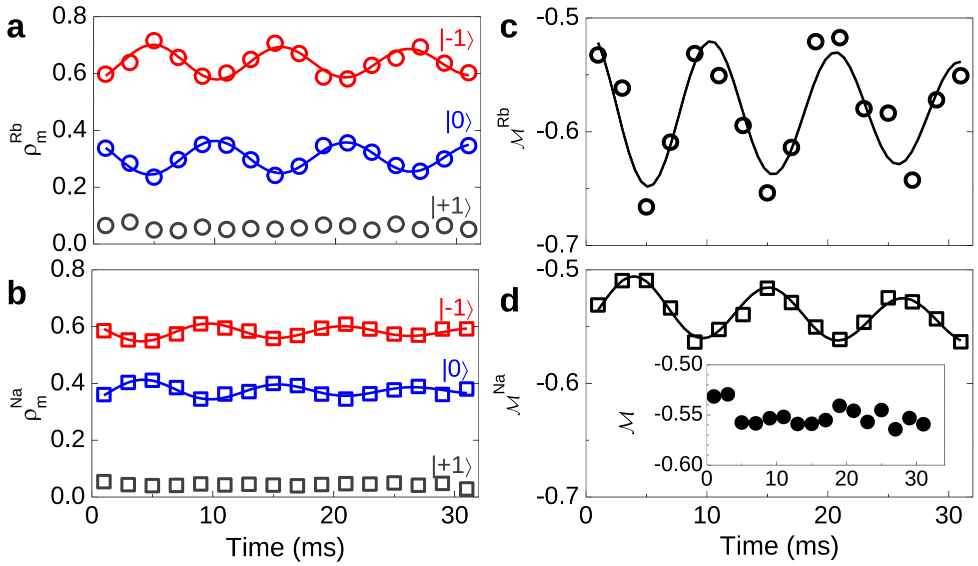

Figure 5.3: (color online) Coherent heteronuclear spin dynamics at $B = 1.9$ G. **a**, **b**, evolution of the fractional spin populations of Rb (circle) and Na (square). **c**, **d**, magnetization oscillations of Rb and Na. The oscillation amplitudes differences are due to the number imbalance. Inset: total magnetization. Solid lines are sinusoidal fitting.

oscillations of $\mathcal{M}^{\mathrm{Na}}$ and $\mathcal{M}^{\mathrm{Rb}}$ with a π-phase difference is a clear signature of the coherent heteronuclear spin-changing process. The clean oscillations between the $|-1\rangle$ and $|0\rangle$ states also indicates that homonuclear and other heteronuclear spin-changing processes are greatly suppressed.

Similar measurements are performed for a range of magnetic fields; three examples are plotted in Fig. 5.5a. Away from B_0, fast oscillation with small amplitude can be observed, while very close to B_0, *e.g.* at $B = 1.7$ G (middle), the oscillation is slow but with large amplitude. One further feature is worth noticing. Comparing oscillations at $B = 1.5$ G (top) and 1.9 G (bottom), we note that the initial slopes of population change for the same spin states have opposite signs on different sides of B_0. For instance, at the very beginning, the Rb $|-1\rangle$ population decreases at 1.5 G but increases at 1.9 G. The same behavior is observed for Na. This is a direct reflection of the sign change in ΔE, as depicted in Fig. 5.1. These behaviors are well reproduced in our numerical simulations

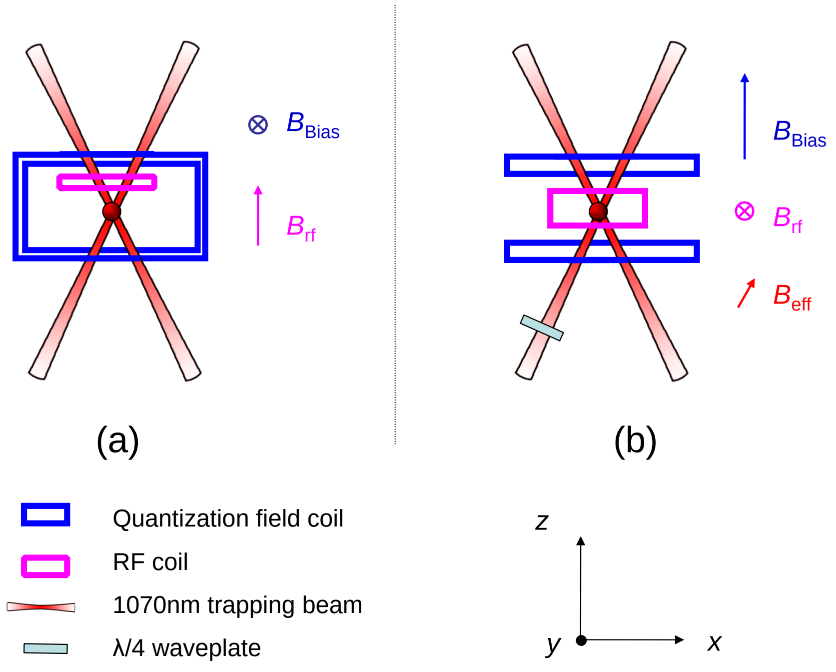

Figure 5.4: Experimental setup for the spinor dynamics at different magnetic fields. (a) The quantization field is along vertical direction (y-axis), so that the effective magnetic field is zero projected to this direction. The setup corresponds to Fig. 5.5. (b) The quantization field is along horizontal direction (z-axis), and the projected effective magnetic field can be control by adding a $\lambda/4$ waveplate. The setup corresponds to Fig. 5.6.

and the initial oscillation directions are consistent with the ferromagnetic spin-changing interaction $\beta < 0$.

We extract the oscillation amplitudes and periods for different magnetic fields and summarize the results in Fig. 5.5c and 5.5d. Near B_0, the system is in the interaction dominated regime where an asymmetric double peak appears in the oscillation amplitude with a non-zero dip in between. This can be understood by noting that resonances appear when the absolute values of ΔE and spin-dependent interaction are comparable, which can occur on either side of B_0, analogous to the single species case where the quadratic Zeeman shift is

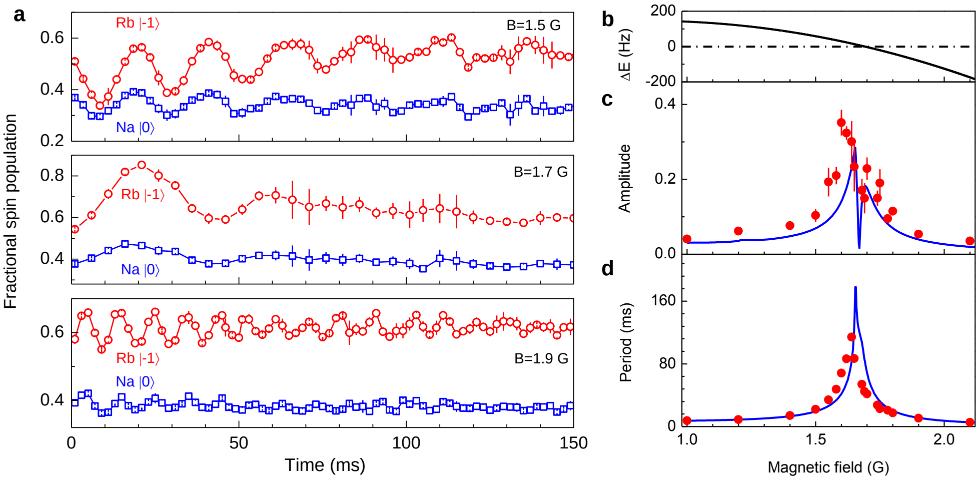

Figure 5.5: (color online) Dependence of heteronuclear spin dynamics on external magnetic field B. **a**, spin oscillations at $B = 1.5$ G (top), 1.7 G (middle) and 1.9 G (bottom) for $|-1\rangle$ of Rb (red circle) and $|0\rangle$ of Na (blue squares). The solid curves are for eye guiding and error bars are from statistics of several shots. **b**, magnetic energy ΔE vs. B. **c**, **d**, spin oscillation amplitudes **c** and periods **d** extracted from the Rb data. Solid blue lines are calculations based on many-body kinetic equations using experimental atomic conditions without fitting parameters. Error bars for both the amplitude and the period are from fitting of the oscillations and represent one standard deviation.

tuned by microwave [114]. However, the exact resonance positions depend also on homonuclear spin-dependent interactions and initial conditions. The double peak behavior is, however, not readily distinguishable in the period where only one peak is observed.

To understand the observed spin dynamics quantitatively, we model the Na condensate with the time-dependent Gross-Pitaevskii equation [57, 95] and the thermal Rb cloud with the kinetic equation for the Wigner distribution function [96, 97]. The dynamics of the two species are coupled through the interaction in Eq.(3.13). Within the random phase and single mode approximations (SMA), our simulation agrees well with the measurements, as shown in Fig. 5.5c and 5.5d. The simulated oscillation period shows only a small kink near B_0, consistent with our experiment conditions. This kink can be regarded as a remnant of the double peak structure that occurs if the numbers of the two species are equal. As the number imbalance increases, one of the peaks gradually disappears, leading to a kink structure in our simulation. We note that the SMA is valid for both BEC and thermal clouds in the tight crossed ODT [96, 97].

5.5 Control of the Resonance

A unique feature of the heteronuclear spin dynamics is its dependence on the vector light shift, which is spin- and species-dependent. The position of the resonance is determined by the differential Zeeman shift as well as the interspecies interaction strength. The zero point of the Zeeman energy can be tuned by the trapping 1070nm optical dipole beam, which generate an effective magnetic field for atoms. In the following, we tune the ellipticity of the ODT beams to control the spin dynamics. We start by evaluating the magnitude of the effective field.

Vector Light Shift

The interaction of optical field with atoms causes the energy shifts of the levels, which is called the AC stark shift. The total shift can be calculated and expressed in terms of the quantum numbers due to the angular momentum structure of the atom, and divided into three parts [60]:

$$\begin{aligned}\Delta U\left(F, m_F; \omega\right) = -\alpha^{(0)}\left(F; \omega\right)\left|E_0^{(+)}\right|^2 - \alpha^{(1)}\left(F; \omega\right)\left(i\mathbf{E}_0^{(-)} \times \mathbf{E}_0^{(+)}\right)_z \frac{m_F}{F} \\ -\alpha^{(2)} \frac{\left(3\left|E_{0z}^{(+)}\right|^2 - \left|E_0^{(+)}\right|^2\right)}{2}\left(\frac{3m_F^2 - F(F+1)}{F(2F-1)}\right),\end{aligned} \tag{5.2}$$

where F and m_F are the quantum numbers of the total angular momentum and its projection on z-axis, ω is the frequency of the light. The complex vector fields are defined such that the electric field is rewritten as

$$\mathbf{E}\left(t\right) = \mathbf{E}_0^{(-)} e^{i\omega t} + \mathbf{E}_0^{(+)} e^{-i\omega t}, \tag{5.3}$$

$\alpha^{(0)}$, $\alpha^{(1)}$, $\alpha^{(2)}$ are the scalar, vector and tensor polarizabilities, defined as

$$\begin{aligned}
&\alpha^{(0)}\left(F;\omega\right)=\sum_{F'}\tfrac{2\omega_{F'F}\left|\langle F\|\mathbf{d}\|F'\rangle\right|^2}{3\hbar\left(\omega_{F'F}^2-\omega^2\right)}\\
&\alpha^{(1)}\left(F;\omega\right)=\sum_{F'}\left(-1\right)^{F+F'+1}\sqrt{\tfrac{6F(2F+1)}{F+1}}\begin{Bmatrix}1&1&1\\F&F&F'\end{Bmatrix}\tfrac{\omega_{F'F}\left|\langle F\|\mathbf{d}\|F'\rangle\right|^2}{\hbar\left(\omega_{F'F}^2-\omega^2\right)}\\
&\alpha^{(2)}\left(F;\omega\right)=\sum_{F'}\left(-1\right)^{F+F'}\sqrt{\tfrac{40F(2F+1)(2F-1)}{3(F+1)(2F+3)}}\begin{Bmatrix}1&1&2\\F&F&F'\end{Bmatrix}\tfrac{\omega_{F'F}\left|\langle F\|\mathbf{d}\|F'\rangle\right|^2}{\hbar\left(\omega_{F'F}^2-\omega^2\right)},
\end{aligned}\tag{5.4}$$

where F' runs over all other states, $\langle F\left\|\mathbf{d}\right\|F'\rangle$ is the reduced matrix element related to the transition dipole matrix element $\langle J\left\|\mathbf{d}\right\|J'\rangle$. $\alpha^{(1)}$ is calculated to be $1.22\times10^{-40}\mathrm{C}\cdot\mathrm{m}^2\cdot\mathrm{V}^{-1}$ for Rb, and two orders of magnitude smaller for Na. For a given F, neglecting the much smaller tensor part, the scalar part gives an overall shift for all m_F, while the vector part is m_F-dependent and resembles the linear Zeeman effect, thus the light acts as an effective magnetic field, which magnitude depends on the polarization.

To estimate the effective magnetic field, we need to calculate the circular polarization component of the light beam of optical trap. Assume that the electric field at atom position is

$$\mathbf{E}\left(t\right)=E_x\hat{\mathbf{e}}_x\cos\left(\omega t+\theta_x\right)+E_y\hat{\mathbf{e}}_y\cos\left(\omega t+\theta_y\right).\tag{5.5}$$

So $\mathbf{E}_0^{(\pm)}=\left(E_x\hat{\mathbf{e}}_xe^{\mp i\theta_x}+E_y\hat{\mathbf{e}}_ye^{\mp i\theta_y}\right)/2$, and the term related to the polarization in 5.2 is

$$i\mathbf{E}_0^{(-)}\times\mathbf{E}_0^{(+)}=i\begin{vmatrix}\hat{\mathbf{e}}_x&\hat{\mathbf{e}}_y&\hat{\mathbf{e}}_z\\E_xe^{i\theta_x}/2&E_ye^{i\theta_y}/2&0\\E_xe^{-i\theta_x}/2&E_ye^{-i\theta_y}/2&0\end{vmatrix}=\frac{1}{2}E_xE_y\sin\left(\theta_x-\theta_y\right)\hat{\mathbf{e}}_z.\tag{5.6}$$

In our case, the optical beam is linear initially, so $E_x=E$, $E_y=0$ and $\theta_x=\theta_y=0$. In the presence of a $\lambda/4$ waveplate, which optical axis is rotated by θ with respect to the linear polarization direction, we can decompose the electric field in the frame with the waveplate (x, y-axis along fast and slow axis):

$$\begin{aligned} E_x &= E\cos(\theta) \\ E_y &= E\sin(\theta) \\ \theta_x - \theta_y &= k\tfrac{\lambda}{4} = \tfrac{\pi}{2}. \end{aligned} \tag{5.7}$$

Hence

$$i\mathbf{E}_0^{(-)} \times \mathbf{E}_0^{(+)} = \frac{1}{4}E^2\sin(2\theta)\,\hat{\mathbf{e}}_z = \frac{1}{4}E^2\wp\hat{\mathbf{e}}_z, \tag{5.8}$$

where we define the polarization factor $\wp = \sin(2\theta)$ such that $\wp = 0, \pm1$ for $\pi, \sigma^{\pm}$ polarization ($\theta = 0, \pm 45^\circ$).

In terms of the intensity $I = \frac{1}{2}c\varepsilon_0 E^2$, the effective magnetic field along the optical beam is given by

$$B_{\text{ac,max}} = \alpha^{(1)}\frac{1}{4}E^2\wp/c_1 = \alpha^{(1)}\frac{I}{2c\varepsilon_0}\wp/c_1, \tag{5.9}$$

where $c_1 = 0.70\text{MHz/Gauss}$ is the coefficient for the linear Zeeman shift $p = c_1 B$. For our optical beam with 128mW power and 48μm beamwaist, the maximum effective field is $B_{\text{ac,max}} = 1.74\text{mG}$. Finally when the angle between the quantization axis and the optical beam is α, the effective magnetic field experienced by the atoms is $B_{\text{ac}} = B_{\text{ac,max}}\cos(\alpha)$, in our horizontal quantization axis case, $\alpha = 31^\circ$ and $B_{\text{ac}} = 1.49\text{mG}$.

For large detuning Δ (laser frequency relative to the center of mass frequency of D-lines) exceeding the excited state fine structure splitting Δ_{FS}, a useful expression for estimation of the spin-dependent vector light shift is [115]

$$U_m(\vec{r}) \propto \frac{\wp m}{\omega_0^3}\frac{\Delta_{\text{FS}}}{\Delta^2}I(\vec{r}), \tag{5.10}$$

It is more clear from this expression that due to the larger Δ, ω_0 and smaller Δ_{FS}

for ^{23}Na, B_{ac} for ^{23}Na is less than 1% of ^{87}Rb. So effectively speaking, by tuning $\wp$, we can control the linear Zeeman energy for Rb and Na independently. The measurements shown in Fig. 5.3 and Fig. 5.5 are performed with B_{ac} essentially zero.

Tuning the Dynamics

Although small, B_{ac} has a dramatic influence on the heteronuclear spin dynamics. For simplicity, the much smaller B_{ac} for Na is ignored from now on. On the other hand, the much larger B_{ac} for ^{87}Rb can shift ΔE significantly, as illustrated in Fig. 5.6a. For $B_{\text{ac}} < 0$, the zero crossing point is shifted to smaller external magnetic fields. Eventually, for $B_{\text{ac}} < -0.2$ mG the entire ΔE curve is shifted to below zero and the zero crossing disappears. In such cases, the spin dynamics will be essentially driven by Zeeman energies with a peak at the field of minimum $|\Delta E|$. When $B_{\text{ac}} > 0$, the zero crossing point and thus the resonance position always shifts to higher magnetic field.

Experimentally, $\wp$, and hence B_{ac}, is tuned by applying the external magnetic field in the horizontal plane and inserting a $\lambda/4$ waveplate into one of the ODT beams as discussed above, with θ the angle between the waveplate's axis and the input linear polarization of the light. For the typical range of θ varied in our experiment without causing significant heating, B_{ac} ranges from -0.32 to 0.32 mG. As shown in our measurement in Fig. 5.6b, a rather small B_{ac} can cause a significant change of the resonance position. For example, at $B_{\text{ac}} = 0.32$ mG, the resonance is shifted upward by about 0.4 G. On the other hand, for negative B_{ac} such that the zero crossing disappears, the lineshape of the oscillation becomes much broader, as for example when $B_{\text{ac}} = -0.32$ mG, where the oscillation is always far off resonance.

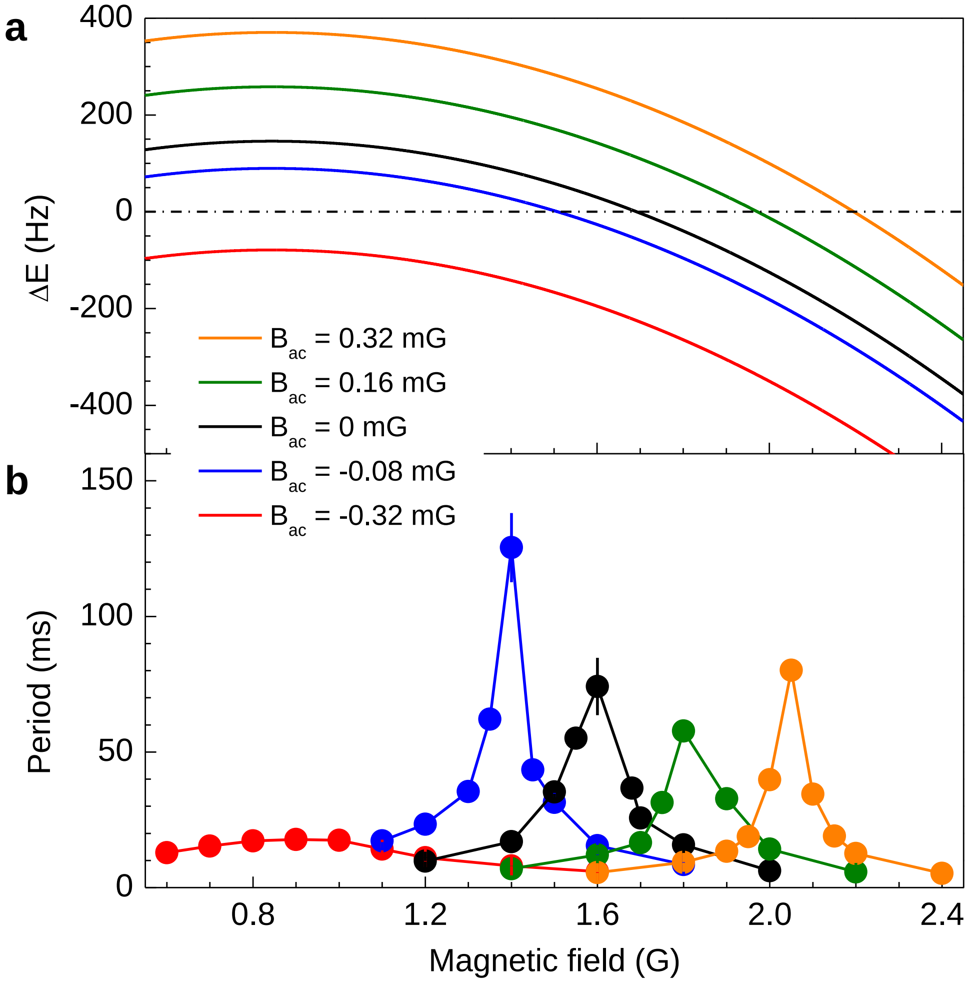

Figure 5.6: (color online) Optical control of coherent heteronuclear spin dynamics with vector light shift. **a**, modified dependence of ΔE on B with light induced effective magnetic field $B_{\rm ac}$ on Rb. **b**, resonance positions as observed in the period vary with changing $B_{\rm ac}$. Solid curves are for eye guiding and error bars are from fitting of the oscillations. $B_{\rm ac}$ is calculated based on the measured light intensity I and $\wp$.

5.6 Prospect

To summarized the experiments described above, we have observed interaction driven coherent spin-changing dynamics between two different spin-1 Bose gases. Both the oscillation period and amplitude can be tuned over a large range with either external magnetic fields or, quite unique to our system, the light polarizations of the ODT. This latter capability is especially promising because it allows sensitive and versatile control of the spin dynamics, as demonstrated in our experiment.

Our system can serve as an ideal platform for simulating complicated spin systems, such as the coupled electronic and nuclear spin system. The exchange interaction allow us to simulate the magnetic impurity problems. For example, a bosonic version of Kondo model [116, 117] may be realized in optical lattice. Out system is similar to the two-orbital magnetism model originally proposed for alkali-earth atoms [118], but the two orbits are replaced by two different kinds of atoms with one the species prepared in the Mott regime while the other in the superfluid regime. In addition, in analogous to the generation of entanglement with spin-changing interactions in single species spinor condensates [119, 120], the inter-species spin-changing interaction can also be used to generate entanglement between distinguishable atoms and strongly correlated state [121]. Finally, similar dynamics should exist in other ultracold spinor mixtures consisting of atoms of all possible statistical combinations. Furthermore, what we have investigated here with Na and Rb can be readily extended to other Bose-Bose, Fermi-Fermi and Bose-Fermi mixtures, which are already available in many labs around the world. Our work can be a wake-up call for them toward a new research direction in ultracold atoms. In fact, theoretical proposals motivated by our experiment already appeared for Bose- Fermi spinor mixtures. Recently it is predicted that the spin-exchange interaction between bosons and fermions can lead to spontaneous quantum Hall effect and a chiral superfluid [122]. The collective modes in a Bose-Fermi spinor mixture are also investigated very recently [123].

5.7 Acknowledgement

The main part of this chapter appears in the published journal article in our group
X. Li, B. Zhu, X. He, F. Wang, M. Guo, Z. Xu, S. Zhang, and D. Wang, Coherent Heteronuclear Spin Dynamics in an Ultracold Spinor Mixture. Phys. Rev. Lett. **114**, 255301 (2015),
of which the author of this thesis is the first author.

Chapter 6

Spin Dynamics in Thermal ^{87}Rb Gases

6.1 Introduction

In chapter 5 we study the coherent spin mixing dynamics between Rb and Na with spin $F = 1$. The focus is on the interspecies spin-exchange interaction and its interplay with differential Zeeman energy. In this chapter, we focus on the thermal nature of a spinor gas and address the problem of whether coherence exist in such gas rather than condensate and what would be the difference. The experiments are carried out with Rb thermal gases both in spin-1 and spin-2 cases.

A significant difference between a BEC and a thermal cloud is that atoms in a BEC occupy the lowest energy state and share the same spatial wavefunction. In analyzing the coherent spin-mixing dynamics in spinor BECs, nice agreements can typically be obtained under SMA, in which the external and internal degree of freedom are seperated [57, 124–126]. It is thus natural to ask whether such dynamics can be observed with multi-spatial-mode spinor gases. Although collisions in these gases are typically considered random or incoherent in sptial degree of freedeom, coherence among spin degree of freedeom can persist for a long time [127, 128]. In fact, coherent spin-mixing dynamics were recently observed in a thermal spin-1 ^{23}Na gas [129] and a degenerate Fermi gas ^{40} [53, 130]. The experimental result agree well with dynamical equations consider only spin degree of freedom, indicating that the spin and spatial degree of freedom can still be decoupled even without condensate.

In this work, we present experimental investigation of coherent spin-mixing dynamics in ultracold thermal ^{87}Rb gases. Different from the antiferromagnetic spin-1 Na spinor gas [34], the spin-dependent interaction in spin-1 ^{87}Rb is ferromagnetic and typically much smaller in magnitude [131, 132]. Amazingly we still observe robust and long-time coherent spin-mixing dynamics driven by the 70pK spin-dependent interaction in thermal samples with a typical temerature of 400nK. In addition, we also observe clean coherent spin-mixing dynamics in spin-2 ^{87}Rb thermal gas, which has more spin-mixing channels and thus richer dynamics [133, 134]. In both cases, dependences of the spin dynamics on external magnetic fields are studied in detail and are explained well by a theoretical model develped under a single-spatial-mode approximation.

6.2 Dynamical Equation for $F = 2$ thermal gas

While spinor BECs are well described by coupled Gross- Pitaevskii equations, pure thermal spinor gases can be handled with the semiclassical Boltzmann transport equation with the Wigner function as the distribution function. Following this approach, several groups have predicted the existence of spin waves and spin-mixing oscillations in spin-1 thermal gases [96, 97]. These theoretical results were successfully applied to the spin-1 Na thermal spinor gas in Ref. [129]. It was found that under the right experimental conditions, the spin dynamics can be separated from the multispatial modes. Compared with spin-1 spinor BECs, one needs only to multiply a factor of 2 in the spin-dependent interaction coefficient [129]. The formalism for spin-1 has been derived in the last chapter. For spin-2 case, considering the interaction of the form 3.12, the Hamiltonian in second-quantization language is expressed as

$$\begin{aligned} H = \int dr \Bigg[& \hat{\psi}_k^\dagger \left(-\frac{\hbar^2}{2m} \nabla^2 + V(r) + qF_z^2 \right) \hat{\psi}_k \\ & + \frac{g_0}{2} \sum_{kj} \hat{\psi}_k^\dagger \hat{\psi}_j^\dagger \hat{\psi}_j \hat{\psi}_k + + \frac{g_1}{2} \sum_{kjlm} \hat{\psi}_k^\dagger \hat{\psi}_j^\dagger \mathbf{F}_{kj} \cdot \mathbf{F}_{lm} \hat{\psi}_m \hat{\psi}_j \\ & + \frac{g_2}{2} \sum_{kj} \frac{1}{5} (-1)^{k-j} \hat{\psi}_k^\dagger \hat{\psi}_{-k}^\dagger \hat{\psi}_{-j} \hat{\psi}_j \Bigg], \end{aligned} \tag{6.1}$$

where all parameters have been defined previously. Spin-2 ^{87}Rb is believed to be antiferromagnetic withg_1 positive and g_2 negative but of much smaller magnitude. Following the derivation of the spin-1 Boltzmann equation in Sec. 3.3, we define the Wigner distribution function 3.46, and the Boltzmann equation is given by Eq. 3.47, where the matrix elements of the interaction potential U are

$$\begin{aligned} U_{kj}(\mathbf{r}) = & \left[qF_z^2 + g_0 \mathrm{Tr}(\mathrm{n}) + \mathrm{g_0 n} \right]_{kj} \\ & + \left[g_1 \sum_\mu \mathrm{Tr}(\mathrm{F}_\mu \mathrm{n}) \mathrm{F}_\mu + g_1 \sum_\mu Tr(F_\mu n) F_\mu \right] \\ & + 2g_2 \frac{(-1)^{k-j}}{5} n_{-j,-k}, \end{aligned} \tag{6.2}$$

here $\mu = x, y$, and z, and Tr is the trace operation. The factor of 2 in the last term is a result of equal Hartree and Fock term contributions. Note that this term vanishes for the spin-1 case.

In the limit of strong trapping potential where the spatial motion is moderately faster than the spin dynamics character- ized by interaction energies $g_{1,2}\mathrm{Tr}(n)$, the spatial-dependent interactions can be averaged out. As done in Sec. 3.3, we can decouple the spinor evolution $\sigma_{kj}(t) = \sqrt{\rho_k} e^{i\theta_k} \sqrt{\rho_j} e^{-i\theta_j}$ from the spatial and momentum distribution $w(\mathbf{r}, \mathbf{p})$ and express the Wigner function matrix elements as $f_{kj}\left(\mathbf{r},\mathbf{p},t\right)=w\left(\mathbf{r},\mathbf{p}\right)\sigma_{kj}\left(t\right)$, analogous to the popular SMA in dealing with spin dynamics in BECs. Substituting this into Eq. 3.47 and integrating over position and momentum, we obtain the following equation of motion for the coherent spinor dynamics in a thermal gas:

$$\frac{\partial}{\partial t}\sigma_{kj}=\frac{1}{i\hbar}\left[U^{\text{spin}},\sigma\right]_{kj}, \tag{6.3}$$

where the spin-dependent interaction potential

$$\begin{aligned}U_{kj}^{\text{spin}}\left(\mathbf{r}\right)=&\left[qF_z^2+g_1\bar{n}\sum_{\mu}\text{Tr}\left(\text{F}_\mu\sigma\right)\text{F}_\mu\right.\\&\left.+g_1\bar{n}\sum_{\mu}F_\mu\sigma F_\mu\right]_{kj}+2g_2\bar{n}\frac{\left(-1\right)^{k-j}}{5}\sigma_{-j,-k},\end{aligned} \tag{6.4}$$

here, $\bar{n}=\int d\mathbf{r}[\text{Tr}\left(n\left(\mathbf{r}\right)\right)]^2/N$, N is the total atom number.

For spin 1, σ is represented by 3×3 matrices. With identity $\sum\limits_{\mu}F_\mu AF_\mu=\text{Tr}A+A+\sum\limits_{\mu}\text{Tr}\,(F_\mu A)F_\mu$ for any 3×3 matrix A, it can be easily shown that the two g_1 terms have equal contributions in Eq. 6.3. Thus the spin-dependent interaction can be summed as $2g_1\bar{n}\sum\limits_{\mu}\text{Tr}\,(F_\mu\sigma)F_\mu$, which is a factor-of-2 larger than that in spin-1 pure BECs [129].

In the case of spin 2, σ is represented by 5×5 matrices and the above identity is not true in general. However, if σ is constructed from pure-state spinor wave functions, which is the case in our experiment, contributions from the two g_1 terms are again the same and thus the factor of 2 still holds. Combined with the factor of 2 in the g_2 term, the overall spin-dependent interaction is also doubled compared with spin-2 pure BECs.

6.3 Experimental Procedure

The experimental procedures are similar to those in the spin-1 mixture experiment described in the last chapter. In brief, we prepare the ultracold ^{87}Rb sample by evaporative cooling in a hybrid magnetic quadrupole plus ODT [81, 106, 135] first. The magnetic trap ensures a 100% spin-polarized sample in the $|1,-1\rangle$ hyperfine Zeeman state. The sample is then transferred to a crossed ODT in which the final evaporation is performed within a weak magnetic field to preserve the atom's spin state. In the same setup, we can produce a pure ^{87}Rb BEC with 2×10^5 atoms. For the current experiment, we control the atom number and stop the evaporation before the BEC phase transition to make pure thermal gases. The measured typical final trap frequencies are $(\omega_x, \omega_y, \omega_z) = 2\pi \times (190, 211, 113)$Hz.

For investigating the spin-1 case, after the final evaporation, we hold the sample in the ODT for several hundred milliseconds to ensure full thermalization before the magnetic field is set to a desired value along the z axis, with the transverse magnetic fields compensated to less than 3mG. To initialize the spin dynamics, we directly apply a resonant RF $\pi/2$ pulse to transfer the sample from the $|1,-1\rangle$ hyperfine state to the fully transversely magnetized initial state $\varsigma_1(0) = \left(1/2, 1/\sqrt{2}, 1/2\right)^T$.

To investigate spinor dynamics in the spin-2 case, we first transfer the atoms to a $|2,-2\rangle$ hyperfine state with a microwave rapid adiabatic passage at a Bield of 1.3 G with a near-unity efficiency. The magnetic field is then changed adiabatically to a desired value before a fully transversely magnetized state $\varsigma_2(0) = \left(1/4, 1/2, \sqrt{3/8}, 1/2, 1/4\right)^T$ is pre- pared with a RF $\pi/2$ pulse. The magnetization is defined as $2\rho_{+2} - 2\rho_{-2} + \rho_{+1} - \rho_{-1}$ in this case.

After initialization, the system is in a far-from-equilibrium state and spin-mixing dynamics will start. After holding the sample in the trap for a range of time for the dynamics to evolve, the ODT is turned off abruptly and atoms in different spin states are detected with the time-of-flight Stern-Gerlach absorption imaging technique after 12-ms expansion. Our absorption imaging setup is calibrated with the high saturation method [101, 102]. The number of atoms in each spin state N_i is extracted from the images and the fractional population $\rho_i = N_i/N$ is then calculated.

6.4 Experimental Result

Spin-1 Case

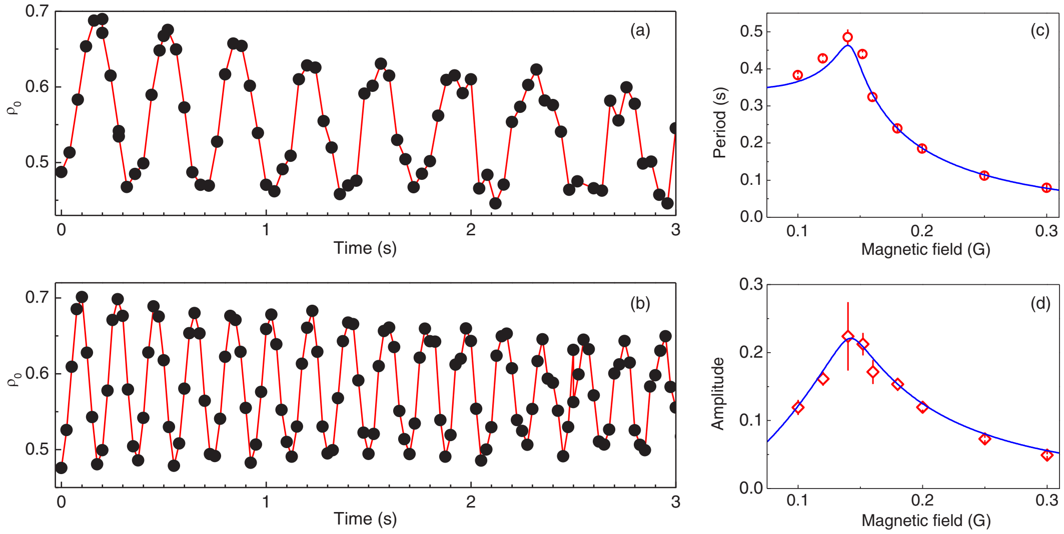

Figure 6.1: Coherent spin population oscillation of ^{87}Rb spin-1 normal gas and its dependence on magnetic field. (a, b) Exemplary temporal evolution of ρ_0 at magnetic fields of 0.1 and 0.18G, respectively. Red solid curves are to guide the eye. (c, d) The magnetic field dependence of the oscillation period ($\circ$) and amplitude ($\diamond$) with a resonant feature located near 0.14G. Error bars here are from fitting of the oscillations. Blue solid curves are fittings with Eq. 6.3.

In Figs. 1(a) and 1(b) we present spin population oscilla- tions for ^{87}Rb thermal spin-1 gases at magnetic felds of 0.1 and 0.18G, respectively. We can immediately see that the oscillation depends strongly on the magnetic field. This can be understood from U^{spin}, which has only the $2g_1$ term and the quadratic Zeeman q term for spin 1. While the negative $2g_1$ term favors the ferromagnetic state, the positive q favors the polar state [35]. Nonequilibrium spin-mixing dynamics is just the result of the competition between them. Similar to spin-1 BEC, depending on their relative strengths, spin dynamics can be divided into the interaction regime and the Zeeman regime [136]. With the $2g_1$ term fixed by the density, external magnetic fields can be applied to tune the system into either regime.

When the magnetic field is low and thus q is small, the system is in the interaction regime and the oscillation period is predominately determined by the $2g_1$ term [136]. This is the case in Fig. 6.1. At higher magnetic field B, $q(\sim 72B^2\text{Hz}/\text{G}^2)$ dominates the rather small $2g_1$ term ($2g_1\langle n\rangle \sim 1.45Hz$ for our typical density) and the system enters the Zeeman regime in which the oscillation period is $\propto 1/q$ [136]. In both cases these oscillations last for a rather long time, although only data in the first 3s are shown. For longer times, the oscillation continues but becomes nonperiodic. To extract the oscillation period and amplitude, we fit the first several oscillations to a damped sinusoidal function.

For the current initial state, the crossover between these two regimes happens when $q \approx 2g_1\langle n\rangle$ [92, 129].Aresonance feature is observed near this crossover in our experiment, as illustrated in Figs. 6.1(c) and 6.1(d). The resonance happens at about 0.14G, evident by the longest period and the largest amplitude at this field. On the higher field side where the dynamics is dominated by q, the oscillations become faster with smaller amplitude. This is similar to the detuned Rabi oscillations in driven two-level systems. Eventually, when the magnetic field is too large, which corresponds to the large detuning case, the oscillation amplitude becomes too small to be observed. On the lower field side, the behavior is quite different. While the amplitude also keeps decreasing, the period levels off to $\sim 1/2g_1\langle n\rangle$.

As illustrated by the solid curves in Figs. 6.1(c) and 6.1(d), these behaviors are well captured by the simulation with Eq. 6.3. These curves are fits to the data points with the measured mean density of $\langle n \rangle \approx 3.0 \times 10^{13}\text{cm}^3$ and a residual magnetization of 0.06(2) due to imperfect control of the RF pulse area in the initial state preparation. With g_1 as the only fitting parameter, we obtain $a_2 - a_0 \approx -1.00 \pm 0.12 a_\mathrm{B}$ (a_B) is the Bohr radius), consistent with the reported value of $a_2 - a_0 \approx -1.07 a_\mathrm{B}$ in Ref. [137]. The rather small but nonzero magnetization also explains the nondivergance on the resonance oscillation period [92].

Here we observe magnetically tuned spin oscillation resonance in the spin-1 ^{87}Rb spinor gas. Previous works with BECs were performed with either an initial state with large magnetization [124] or in a quasi-one-dimensional trap [136]. In the former case, the resonance does not exist [92]. For the latter, the spin healing length $\xi = \hbar/\sqrt{2mn\,|g_1|}$ is smaller than the size in the elongated direction and thus SMA is violated. Spin-mixing dynamics is unstable [113] in this case, as perturbations can cause irreversible conversion of the spin-dependent energy to collective excitation modes. This will lead to the formation of multiple spin domains and destroy the spin coherence within a single full oscillation, making it impossible to observe the resonance. This problem is mitigated in the current work by the tight and near three-dimensional crossed trap.

Spin-2 Case

The interaction between spin-2 ^{87}Rb atoms is antiferromagnetic with $g_1 > 0$, $g_2 < 0$, and $|g_2| \ll g_1$ [138]. Unlike the spin-1 case, spin-2 spinor oscillations can have more than one interaction channel and the spin-2 equation of motion has no exact analytic solutions. The spin-2 ^{87}Rb gas is also subject to inelastic hyperfine changing collisions which greatly limit its lifetime to be about 0.5s.

As shown in Figs. 6.2(a) and 6.2(b), several full oscillations show up within hundreds of milliseconds. The observed behaviors are similar to those studied previously on spin-2 ^{87}Rb BECs with the same initial state [125, 139] and can be understood intuitively from the competition between q and the spin-dependent

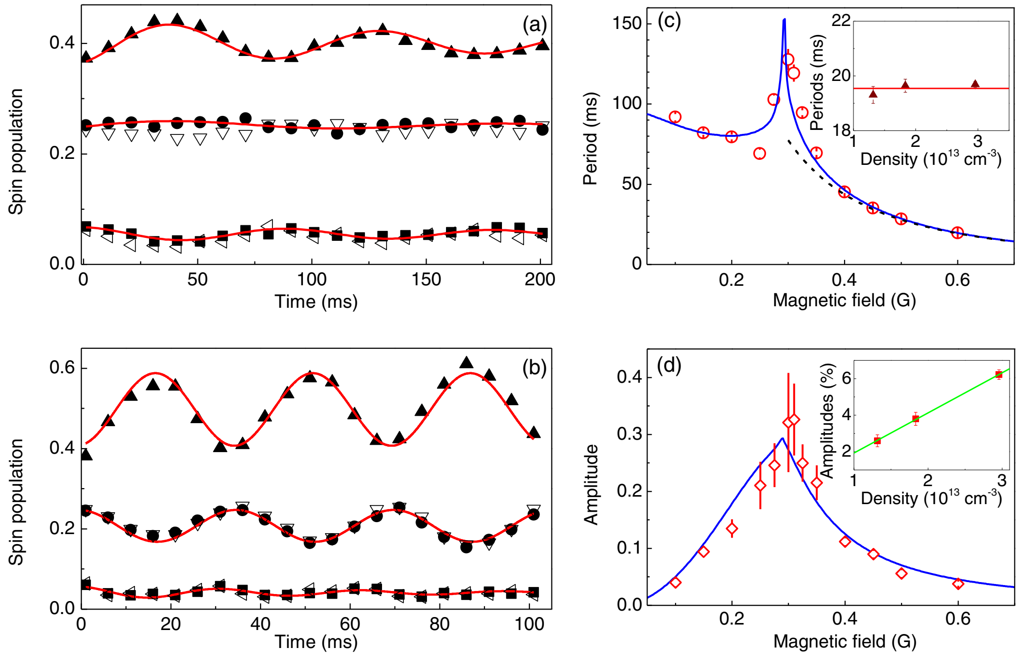

Figure 6.2: Spinor dynamics and its dependence on magnetic field for the ^{87}Rb spin-2 normal gas. (a, b) Evolutions of $\rho_0(\blacktriangle)$, $\rho_1(\bullet)$, $\rho_{-1}(\triangledown)$, $\rho_2(\blacksquare)$, and $\rho_{-2}(\triangleleft)$ at 0.1 and 0.45 G, respectively. Red solid curves in (a) and (b) are fits to the damped sinusoidal function for ρ_0, ρ_1,and ρ_2 only. The measured periods ($\circ$) and amplitudes ($\diamond$)of ρ_0 vs magnetic fields are summarized in (c) and (d). The accompanying error bars are fitting errors. The blue solid curves here are obtained from numerical calculations with Eq. 6.3 and the black dashed curve is a plot of π/q. The insets of (c) and (d) show dependence of the oscillation periods (up triangle) and amplitudes (squares), respectively, on densities at 0.6 G (see text).

interactions. Indeed, ignoring the small g_2 term, for the chosen initial state ζ_2, approximate solutions have been obtained in Refs. [125] and [139], both in the deep interaction and Zeeman regimes. These solutions can be directly generalized to our case by replacing the g_1 factor with $2g_1$, as discussed in the last section.

The factor-of-2 thermal enhancement of the spin-dependent interaction can be verified experimentally. In the Zeeman regime, the spin-mixing process $(0) + (0) \leftrightarrow (-1) + (1)$ dominates and the oscillation follows the fundamental period π/q [125, 139], as depicted by the dashed curve in Fig. 6.2(c). Although the amplitude is typically small, the oscillations are quite fast so that several periods can be observed clearly. As shown in the insets of Figs. 6.2(c) and 6.2(d), with the density varied from $1.3 \times 10^{13}\text{cm}^{-3}$ to $2.9 \times 10^{13}\text{cm}^{-3}$ at 0.6G, the periods are nearly constant, while the amplitudes increase linearly with a slope of $0.022(2.5)/10^{13}\text{cm}^{-3}$. With the best-known value $a_4 - a_2 \approx 6.95a_\text{B}$ [137], this slope gives the oscillation amplitude as $2.0\,(3) \times 3g_1 \langle n \rangle /8q$, while for $F = 2$ spinor BEC, the oscillation amplitude is $3g_1 \langle n \rangle /8q$ [125, 139]. This measurement thus confirms our theoretical prediction that, given a pure initial spin state, the factor-of-2 enhancement in the g_1 term holds for the spin-2 thermal gas.

Figure 6.2(a) is taken in the interaction regime at 0.1G, where q is smaller than the g_1 term, while Fig. 6.2(b) is taken at 0.45G with q much larger than the g_1 term. Besides the rather different oscillation amplitudes and periods, we also find that in the interaction regime, populations only oscillate between $m_F = 0$ and $m_F = \pm 2$ states, while those of the $m_F = \pm 1$ states are nearly 0.25. In the other regime, all spin states are involved but the $m_F = \pm 2$ states have a smaller oscillation amplitude. In the interaction regime at very low field, the oscillation period is $\pi/4g_1 \langle n \rangle$ [125, 139], which is typically long as $g_1 \langle n \rangle$ is small. As a result, few oscillations can be observed within the sample lifetime and these oscillations also show strong damping.

We have carried out similar measurements with magnetic fields ranging from 0.1 to 0.6G and extracted the amplitudes and periods by fitting the oscillations to the damped sinusoidal function. As summarized in Figs. 6.2(c) and 6.2(d), a resonance is observed near 0.3G. Close to resonance, the approximate solution fails. Numerical calculation of the equation of motion in Eq. 6.3 is thus necessary to fully describe the magnetic field dependence. This is performed with the g_1 term obtained from the enhancement factor verification above and the experimentally measured number densities. As shown by the solid curves in Figs. 6.2(c) and 6.2(d), without any free parameters the results already agree with our measurements very well.

As a summary, we have observed and analyzed the nonequilibrium interaction-driven collective spin-mixing dynamics in ferromagnetic spin-1 and antiferromagnetic spin-2 gases of ultracold but noncondensed ^{87}Rb atoms. These dynamics and their magnetic field dependence are proved to be the same as those found in spinor BECs under SMA,with only a factor-of-2 enhancement in the spin-dependent interactions. In the spin-1 case, we can observe oscillations lasting for a very long time limited only by the trap lifetime. Although these oscillations already become irregular at 3s, we nevertheless cannot tell any obvious equilibrium state is reached within 10s. Spin domain formations are fully suppressed in both cases, but even for the spin-1 case without hyperfine changing losses, damping is still observed for most oscillations. This may come from the ignored collisional integral in the Boltzmann equation [53] as well as technical imperfections, such as the residual magnetic field gradient.

6.5 Acknowledgement

The main part of this chapter is extracted from the published journal article in our group
X. He, B. Zhu, X. Li, F. Wang, Z. Xu, and D. Wang, Coherent spin-mixing dynamics in thermal ^{87}Rb spin - 1 and spin - 2 gases, Phys. Rev. A **91**, 033635 (2015).
of which the author of this thesis is the third author, and the largest contribution to the work comes from the first author, Xiaodong He.

Chapter 7

Summary

In this thesis, we describe our two experimental work on the dynamics of spinor gases. The first one is the heteronuclear spin-mixing dynamics between spin-1 ^{87}Rb and ^{23}Na. We successfully observe the coherent oscillations of the population in each spin state by preparing the sample in particular spin states, densities and external magnetic fields. We find that the period and amplitude have a resonance while vary the magnetic field up to 2.4G. The resonance is found to be extremely sensitive to the polarization of the trapping, due to the produced vector light shift. This is unique in the ^{87}Rb-^{23}Na spinor mixture system because they have similar hyperfine structure and nearly equal energy scales, and the relevant Zeeman energy is the difference of the linear and quadratic shift of both species, which is sensitive to a small effective magnetic field for one species.

In the second work we describe the spin-mixing dynamics in thermal spin-1 and spin-2 ^{87}Rb gases. We observed long- lasting oscillation of the population, which indicate the coherence can also exist and in noncondensed atomic cloud. We highlight the role of interaction energy and Zeeman energy in the dynamics, and make a comparison between BEC and thermal cloud. It is interesting that they can obey the same equation of motion, with the spin-dependent interaction term multiplied by a factor-of-2 in the thermal cloud.

We also introduce the necessary theoretical background and describe our experimental apparatus in detail. The experimental findings described above benefit from the stable working of the system. As working in a very compact setup, we are able to load 3×10^8 ^{87}Rb and 5×10^6 ^{23}Na in to the MOTs, and steadily produce 1×10^5 BEC for each species in the final stage. We have also controllable lasers, magnetic fields, RF and microwaves. The system is a versatile platform to study multicomponent quantum gases, as well as to produce ground state ^{23}Na^{87}Rb molecule in the future. For the spinor experiments, we have discussed some research directions in Sec. 5.6 in the setup, including possible studies of the magnetic impurity and entangled BEC. We also hope that our experiment would stimulate more studies on Bose-Bose mixture as well as Bose-Fermi mixture, such as the recent prosposed spontaneous quantum Hall in a mixture of spinor bosons and fermions [122].

Bibliography

[1] M H Anderson, J R Ensher, M R Matthews, C E Wieman, and E a Cornell. Observation of bose-einstein condensation in a dilute atomic vapor. *Science*, 269(5221):198–201, 1995.

[2] C C Bradley, C A Sackett, J J Tollett, and R G Hulet. Evidence of Bose-Einstein condensation in an atomic gas with attractive interactions. *Phys. Rev. Lett.*, 75(9):1687–1690, 1995.

[3] K B Davis, M O. Mewes, M R Andrews, N. J. Van Druten, D S Durfee, D M Kurn, and W Ketterle. Bose-Einstein condensation in a gas of sodium atoms. *Phys. Rev. Lett.*, 75(22):3969–3973, 1995.

[4] Einstein. Quantum theory of the monoatomic ideal gas. *Sitzungsberichte*, V:261–267, 1924.

[5] S. N. Bose. Planck 's Law and Light Quantum Hypothesis . *Zeitschrift für Phys.*, 26(Received):1–4, 1924.

[6] F. London. The λ-Phenomenon of Liquid Helium and the Bose-Einstein Degeneracy. *Nature*, 141(3571):643–644, 1938.

[7] A Griffin, D W Snoke, and S Stringari. *Bose-Einstein Condensation.* Cambridge University Press, 1996.

[8] Charles E Hecht. The possible superfluid behaviour of hydrogen atom gases and liquids. *Physica*, 25(7–12):1159–1161, 1959.

[9] W.C. Stwalley and L.H. Nosanow. Possible "New" Quantum Systems. *Phys. Rev. Lett.*, 36(15):910–913, 1976.

[10] V S Letokhov. Narrowing of the Doppler width in a standing wave. *ZhETF Pisma Redaktsiiu*, 7:348, 1968.

[11] A Ashkin. Trapping of Atoms by Resonance Radiation Pressure. *Phys. Rev. Lett.*, 40(12):729–732, 1978.

[12] Steven Chu, J. E. Bjorkholm, a. Ashkin, and a. Cable. Experimental observation of optically trapped atoms. *Phys. Rev. Lett.*, 57(3):314–317, 1986.

[13] E. L. Raab, M. Prentiss, Alex Cable, Steven Chu, and D. E. Pritchard. Trapping of Neutral Sodium Atoms with Radiation Pressure. *Phys. Rev. Lett.*, 59(23):2631–2634, 1987.

[14] William D. Phillips. Nobel Lecture: Laser cooling and trapping of neutral atoms. *Rev. Mod. Phys.*, 70(3):721–741, 1998.

[15] Alan L Migdall, John V Prodan, William D Phillips, Thomas H Bergeman, and Harold J Metcalf. First Observation of Magnetically Trapped Neutral Atoms. *Phys. Rev. Lett.*, 54(24):2596–2599, 1985.

[16] Eugene P Gross. Structure of a quantized vortex in boson systems. *Nuovo Cim. Ser. 10*, 20(3):454–477, 1961.

[17] Eugene P Gross. Hydrodynamics of a superfluid condensate. *J. Math. Phys.*, 4(2):195–207, 1963.

[18] L P Pitaevskii. Vortex lines in an imperfect Bose gas. *Sov. Phys. JETP*, 13(2):451–454, 1961.

[19] W. Ketterle, D. S. Durfee, and D. M. Stamper-Kurn. Making, probing and understanding Bose-Einstein condensates. page 90, 1999.

[20] S. Stringari. Collective Excitations of a Trapped Bose-Condensed Gas. *Phys. Rev. Lett.*, 77(12):2360–2363, 1996.

[21] D. Jin, J. Ensher, M. Matthews, C. Wieman, and E. Cornell. Collective Excitations of a Bose-Einstein Condensate in a Dilute Gas. *Phys. Rev. Lett.*, 77(3):420–423, 1996.

[22] D. Stamper-Kurn, H.-J. Miesner, S. Inouye, M. Andrews, and W. Ketterle. Collisionless and Hydrodynamic Excitations of a Bose-Einstein Condensate. *Phys. Rev. Lett.*, 81(3):500–503, 1998.

[23] Robert Graham and Dan Walls. Collective excitations of trapped binary mixtures of Bose-Einstein condensed gases. *Phys. Rev. A*, 57(1):484–487, 1998.

[24] S. Burger, K. Bongs, S. Dettmer, W. Ertmer, and K. Sengstock. Dark Solitons in Bose-Einstein Condensates. *Phys. Rev. Lett.*, 83(25):5198–5201, 1999.

[25] J. Denschlag. Generating Solitons by Phase Engineering of a Bose-Einstein Condensate. *Science (80-.).*, 287(5450):97–101, 2000.

[26] K.W. Madison, F. Chevy, and W. Wohlleben. Vortex formation in a stirred Bose-Einstein condensate. *Quantum Electron. Laser Sci. Conf. (QELS 2000). Tech. Dig. Postconf. Ed. TOPS Vol.40 (IEEE Cat. No.00CH37089)*, pages 3–6, 2000.

[27] F Chevy, K W Madison, and J Dalibard. Measurement of the angular momentum of a rotating Bose-Einstein condensate. *Phys. Rev. Lett.*, 85(11):2223–2227, 2000.

[28] J R Abo-Shaeer, C Raman, J M Vogels, and W Ketterle. Observation of

vortex lattices in Bose-Einstein condensates. *Science*, 292(5516):476–479, 2001.

[29] P Engels, I Coddington, P C Haljan, and E a Cornell. Nonequilibrium effects of anisotropic compression applied to vortex lattices in bose-einstein condensates. *Phys. Rev. Lett.*, 89(10):100403, 2002.

[30] I Coddington, P Engels, V Schweikhard, and E a Cornell. Observation of Tkachenko oscillations in rapidly rotating Bose-Einstein condensates. *Phys. Rev. Lett.*, 91(10):100402, 2003.

[31] Tin-Lun Ho and V. Shenoy. Binary Mixtures of Bose Condensates of Alkali Atoms. *Phys. Rev. Lett.*, 77(16):3276–3279, 1996.

[32] H. Pu and N. Bigelow. Collective Excitations, Metastability, and Nonlinear Response of a Trapped Two-Species Bose-Einstein Condensate. *Phys. Rev. Lett.*, 80(6):1134–1137, 1998.

[33] V S Bagnato, D J Frantzeskakis, P G Kevrekidis, B a Malomed, and D Mihalache. Bose-Einstein Condensation: Twenty Years After. *arXiv*, 67(1):5–50, 2015.

[34] J. Stenger, S. Inouye, DM M. Stamper-Kurn, H.-J. Miesner, A. P. Chikkatur, and W. Ketterle. Spin domains in ground-state Bose–Einstein condensates. *Nature*, 396(November):345–348, 1998.

[35] Tin-Lun Ho. Spinor Bose Condensates in Optical Traps. *Phys. Rev. Lett.*, 81(4):742–745, 1998.

[36] Tetsuo Ohmi and Kazushige Machida. Bose-Einstein condensation with internal degrees of freedom in alkali atom gases. *J. Phys. Soc. Japan*, 67(6):1822–1825, 1998.

[37] D S Hall, M R Matthews, C E Wieman, and E A Cornell. Measurements of Relative Phase in Two-Component Bose-Einstein Condensates. *Phys. Rev. Lett.*, 81(8):1543–1546, 1998.

[38] D S Hall, M R Matthews, J R Ensher, C E Wieman, and E A Cornell. Dynamics of Component Separation in a Binary Mixture of Bose-Einstein Condensates [Phys. Rev. Lett. 81, 1539 (1998)]. *Phys. Rev. Lett.*, 81(20):4531, 1998.

[39] M R Matthews, D S Hall, D S Jin, J R Ensher, C E Wieman, E A Cornell, F Dalfovo, C Minniti, and S Stringari. Dynamical Response of a Bose-Einstein Condensate to a Discontinuous Change in Internal State. *Phys. Rev. Lett.*, 81(2):243–247, 1998.

[40] L E Sadler, J M Higbie, S R Leslie, M Vengalattore, and D M Stamper-Kurn. Spontaneous symmetry breaking in a quenched ferromagnetic spinor Bose-Einstein condensate. *Nature*, 443(7109):312–315, 2006.

[41] Stephen Blaha. Quantization rules for point singularities in superfluid He3 and liquid crystals. *Phys. Rev. Lett.*, 36(15):874–876, 1976.

[42] J. Ruostekoski and J.R. R Anglin. Monopole Core Instability and Alice Rings in Spinor Bose-Einstein Condensates. *Phys. Rev. Lett.*, 91(19):190402, 2003.

[43] Usama Al Khawaja and Henk Stoof. Skyrmions in a ferromagnetic Bose-Einstein condensate. *Nature*, 411(6840):918–920, June 2001.

[44] Jae Yoon Choi, Woo Jin Kwon, and Yong Il Shin. Observation of topologically stable 2D skyrmions in an antiferromagnetic spinor bose-einstein condensate. *Phys. Rev. Lett.*, 108(3):1–5, 2012.

[45] S.-K. K. Yip. Internal Vortex Structure of a Trapped Spinor Bose-Einstein Condensate. *Phys. Rev. Lett.*, 83(23):4677–4681, 1999.

[46] Gordon W. Semenoff and Fei Zhou. Discrete symmetries and 1/3-quantum vortices in condensates of F=2 cold atoms. *Phys. Rev. Lett.*, 98(10):1–4, 2007.

[47] Yuki Kawaguchi, Muneto Nitta, and Masahito Ueda. Knots in a spinor bose-einstein condensate. *Phys. Rev. Lett.*, 100(18):1–4, 2008.

[48] J. M. Higbie, L. E. Sadler, S. Inouye, a. P. Chikkatur, S. R. Leslie, K. L. Moore, V. Savalli, and D. M. Stamper-Kurn. Direct, non-destructive imaging of magnetization in a spin-1 bose gas. *IQEC, Int. Quantum Electron. Conf. Proc.*, 2005(July):1635–1636, 2005.

[49] Masahiro Kitagawa and Masahito Ueda. Squeezed spin states. *Phys. Rev. A*, 47(6):5138–5143, 1993.

[50] C. D. Hamley, C. S. Gerving, T. M. Hoang, E. M. Bookjans, and M. S. Chapman. Spin-nematic squeezed vacuum in a quantum gas. *Nat. Phys.*, 8(4):305–308, 2012.

[51] C. Klempt, O. Topic, G. Gebreyesus, M. Scherer, T. Henninger, P. Hyllus, W. Ertmer, L. Santos, and J. J. Arlt. Multiresonant Spinor Dynamics in a Bose-Einstein Condensate. *Phys. Rev. Lett.*, 103(19):1–4, 2009.

[52] C. Klempt, O. Topic, G. Gebreyesus, M. Scherer, T. Henninger, P. Hyllus, W. Ertmer, L. Santos, and J. J. Arlt. Parametric amplification of vacuum fluctuations in a spinor condensate. *Phys. Rev. Lett.*, 104(19):1–4, 2010.

[53] Ulrich Ebling, Jasper Simon Krauser, Nick Fläschner, Klaus Sengstock, Christoph Becker, Maciej Lewenstein, and André Eckardt. Relaxation dy-

namics of an isolated large-spin fermi gas far from equilibrium. *Phys. Rev. X*, 4(2):1–18, 2014.

[54] M. Vengalattore, S. R. Leslie, J. Guzman, and D. M. Stamper-Kurn. Spontaneously modulated spin textures in a dipolar spinor Bose-Einstein condensate. *Phys. Rev. Lett.*, 100(17):2–5, 2008.

[55] Yuki Kawaguchi, Masahito Ueda, Yuki Kawaguchia, and Masahito Uedaa. Spinor Bose-Einstein condensates. *Phys. Rep.*, 520(5):253–381, 2012.

[56] Nguyen Thanh Phuc, Yuki Kawaguchi, and Masahito Ueda. Beliaev theory of spinor Bose-Einstein condensates. *Ann. Phys. (N. Y).*, 328:158–219, 2013.

[57] C. K. Law, H. Pu, and N. P. Bigelow. Quantum spins mixing in spinor Bose-Einstein condensates. *Phys. Rev. Lett.*, 82(February):4, 1998.

[58] Xiaoke Li, Bing Zhu, Xiaodong He, Fudong Wang, Mingyang Guo, Zhi-Fang Xu, Shizhong Zhang, and Dajun Wang. Coherent Heteronuclear Spin Dynamics in an Ultracold Spinor Mixture. *Phys. Rev. Lett.*, 114(25):255301, 2015.

[59] Xiaodong He, Bing Zhu, Xiaoke Li, Fudong Wang, Zhi-Fang Xu, and Dajun Wang. Coherent spin-mixing dynamics in thermal ^{87}Rb spin-1 and spin-2 gases. *Phys. Rev. A*, 91(3):033635, 2015.

[60] Daniel Adam Steck. Quantum and Atom Optics, available online at http://steck.us/teaching (revision 0.8.3, 25 May 2012). 2012.

[61] J. P. Gordon and a. Ashkin. Motion of atoms in a radiation trap. *Phys. Rev. A*, 21(5):1606–1617, 1980.

[62] E. Arimondo, M. Inguscio, and P. Violino. Experimental determinations of the hyperfine structure in the alkali atoms. *Rev. Mod. Phys.*, 49(1):31–75, 1977.

[63] The mathematica add-on "Quantum" is free available online on: http://homepage.cem.itesm.mx/jose.luis.gomez/quantum/index.htm.

[64] J. Dalibard and C. Cohen-Tannoudji. Laser cooling below the Doppler limit by polarization gradients: simple theoretical models. *J. Opt. Soc. Am. B*, 6(11):2023, 1989.

[65] Wolfgang Ketterle and N J Van Druten. Evaporative Cooling of Trapped Atoms. *Adv. At. Mol. Opt. Phys.*, 37:181, 1996.

[66] a. Mosk, S. Kraft, M. Mudrich, K. Singer, W. Wohlleben, R. Grimm, and M. Weidemüller. Mixture of ultracold lithium and cesium atoms in an optical dipole trap. *Appl. Phys. B Lasers Opt.*, 73(8):791–799, 2001.

[67] C. Silber, S. Günther, C. Marzok, B. Deh, Ph W. Courteille, and C. Zimmermann. Quantum-degenerate mixture of fermionic lithium and bosonic rubidium gases. *Phys. Rev. Lett.*, 95(17):1–4, 2005.

[68] B Deh, C Marzok, C Zimmermann, and Ph. W Courteille. Feshbach resonances in mixtures of ultracold ^{6}Li and ^{87}Rb gases. *Phys. Rev. A*, 77(1):4, 2007.

[69] C Marzok, B Deh, Ph. W Courteille, and C Zimmermann. Ultracold Thermalization of ^{7}Li and ^{87}Rb. *Phys. Rev. A*, 76(5):7, 2007.

[70] C. Marzok, B. Deh, C. Zimmermann, Ph W. Courteille, E. Tiemann, Y. V. Vanne, and a. Saenz. Feshbach resonances in an ultracold Li7 and Rb87 mixture. *Phys. Rev. A - At. Mol. Opt. Phys.*, 79(1):1–7, 2009.

[71] C. R. Monroe, E. a. Cornell, C. a. Sackett, C. J. Myatt, and C. E. Wieman. Measurement of Cs-Cs elastic scattering at T=30 μK. *Phys. Rev. Lett.*, 70(4):414–417, 1993.

[72] G Delannoy, S G Murdoch, V Boyer, V Josse, P Bouyer, and A Aspect. Understanding the production of dual Bose-Einstein condensation with sympathetic cooling. *Phys. Rev. A*, 63(5):51602, 2001.

[73] Robert L D Campbell, Robert P Smith, Naaman Tammuz, Scott Beattie, Stuart Moulder, and Zoran Hadzibabic. Efficient production of large ^{39}K Bose-Einstein condensates. *Phys. Rev. A*, 82(6):7, 2010.

[74] J. Goldwin, S. Inouye, M. L. Olsen, B. Newman, B. D. DePaola, and D. S. Jin. Measurement of the interaction strength in a Bose-Fermi mixture with 87Rb and 40K. *Phys. Rev. A - At. Mol. Opt. Phys.*, 70(2):1–4, 2004.

[75] Vladyslav V. Ivanov, Alexander Khramov, Anders H. Hansen, William H. Dowd, Frank Münchow, Alan O. Jamison, and Subhadeep Gupta. Sympathetic cooling in an optically trapped mixture of alkali and spin-singlet atoms. *Phys. Rev. Lett.*, 106(15):1–4, 2011.

[76] G Modugno, G Ferrari, G Roati, R J Brecha, a Simoni, and M Inguscio. Bose-Einstein condensation of potassium atoms by sympathetic cooling. *Science*, 294(5545):1320–1322, 2001.

[77] M. Anderlini, E. Courtade, M. Cristiani, D. Cossart, D. Ciampini, C. Sias, O. Morsch, and E. Arimondo. Sympathetic cooling and collisional properties of a RbCs mixture. *Phys. Rev. A - At. Mol. Opt. Phys.*, 71(6):1–4, 2005.

[78] Immanuel Bloch, Markus Greiner, Olaf Mandel, Theodor W. Hänsch, and Tilman Esslinger. Sympathetic cooling of 85 Rb and . *Phys. Rev. A*, 64(2):85–88, 2001.

[79] Huang Wu Huang Wu and C.J. Foot. Direct Simulation of Evaporative Cooling. *EQEC'96. 1996 Eur. Quantum Electron. Conf.*, 321, 1996.

[80] J. Goldwin, S. Inouye, M. L. Olsen, and D. S. Jin. Cross-dimensional relaxation in Bose-Fermi mixtures. *Phys. Rev. A - At. Mol. Opt. Phys.*, 71(4), 2005.

[81] Dezhi Xiong, Xiaoke Li, F Wang, Dajun Wang, and TF Lam. A ^{23} Na and ^{87} Rb double Bose-Einstein condensate with tunable interactions. *arXiv Prepr. arXiv1305.7091*, page 5, 2013.

[82] A L Fetter and J D Walecka. *Quantum Theory of Many-particle Systems.* Dover Books on Physics. Dover Publications, 2003.

[83] Tin-Lun Ho and V B Shenoy. Local Spin-Gauge Symmetry of the Bose-Einstein Condensates in Atomic Gases. *Phys. Rev. Lett.*, 77(13):2595–2599, 1996.

[84] B. Esry, Chris Greene, James Burke, Jr., and John Bohn. Hartree-Fock Theory for Double Condensates. *Phys. Rev. Lett.*, 78(19):3594–3597, 1997.

[85] E. Timmermans. Phase Separation of Bose-Einstein Condensates. *Phys. Rev. Lett.*, 81(26):5718–5721, 1998.

[86] Christopher J Pethick and Henrik Smith. *Bose-Einstein Condensation in Dilute Gases; 2nd ed.* 2008.

[87] Dan M. Stamper-Kurn and Masahito Ueda. Spinor Bose gases: Symmetries, magnetism, and quantum dynamics. *Rev. Mod. Phys.*, 85(3):1191–1244, 2013.

[88] Bo Yuan Ning, S. Yi, Jun Zhuang, J. Q. You, and Wenxian Zhang. Manipulating dipolar and spin-exchange interactions in spin-1 Bose-Einstein condensates. *Phys. Rev. A - At. Mol. Opt. Phys.*, 85(5):1–5, 2012.

[89] Yuki Kawaguchi, Hiroki Saito, Kazue Kudo, and Masahito Ueda. Spontaneous magnetic ordering in a ferromagnetic spinor dipolar Bose-Einstein condensate. *Phys. Rev. A - At. Mol. Opt. Phys.*, 82(4):1–17, 2010.

[90] B. Pasquiou, E. Maréchal, G. Bismut, P. Pedri, L. Vernac, O. Gorceix, and B. Laburthe-Tolra. Spontaneous demagnetization of a dipolar spinor bose gas in an ultralow magnetic field. *Phys. Rev. Lett.*, 106(25):1–4, 2011.

[91] Wenxian Zhang, Su Yi, and Li You. Mean field ground state of a spin-1 condensate in a magnetic field. *New J. Phys.*, 5, 2003.

[92] W Zhang, D L Zhou, M.-S. Chang, M.-S. Chapman, and L.You. Coherent spin mixing dynamics in a spin-1 atomic condensate. *Phys. Rev. A*, 72(August 2004):13602, 2005.

[93] Erich J. Mueller, Tin Lun Ho, Masahito Ueda, and Gordon Baym. Fragmentation of Bose-Einstein condensates. *Phys. Rev. A - At. Mol. Opt. Phys.*, 74(3):1–17, 2006.

[94] Jasper S. Krauser, Jannes Heinze, Nick Fläschner, Sören Götze, Ole Jürgensen, Dirk-Sören Lühmann, Christoph Becker, and Klaus Sengstock. Coherent multi-flavour spin dynamics in a fermionic quantum gas. *Nat. Phys.*, 8(11):1–10, 2012.

[95] Z. F. Xu, D. J. Wang, and L. You. Quantum spin mixing in a binary mixture of spin-1 atomic condensates. *Phys. Rev. A - At. Mol. Opt. Phys.*, 86(1):1–6, 2012.

[96] Stefan S. Natu and Erich J. Mueller. Spin waves in a spin-1 normal Bose gas. *Phys. Rev. A - At. Mol. Opt. Phys.*, 81(5):1–9, 2010.

[97] Yuki Endo and Tetsuro Nikuni. Spin dynamics of a trapped spin-1 bose

gas above the Bose-Einstein transition temperature. *J. Low Temp. Phys.*, 152(1-2):21–46, 2008.

[98] Carl E. Wieman and Leo Hollberg. Using diode lasers for atomic physics. *Rev. Sci. Instrum.*, 62(January):1–20, 1991.

[99] C. J. Hawthorn, K. P. Weber, and R. E. Scholten. Littrow configuration tunable external cavity diode laser with fixed direction output beam. *Rev. Sci. Instrum.*, 72(12):4477–4479, 2001.

[100] W Demtröder. *Laser Spectroscopy: Basic Concepts and Instrumentation*. Advanced texts in physics. Springer, 2003.

[101] G Reinaudi, T Lahaye, Z Wang, and D Guéry-Odelin. Strong saturation absorption imaging of dense clouds of ultracold atoms. *Opt. Lett.*, 32(21):3143–3145, 2007.

[102] Woo Jin Kwon, Jae-yoon Choi, and Yong-il Shin. Calibration of saturation absorption imaging of ultracold atom clouds. *J. Korean Phys. Soc.*, 61(12):1970–1974, 2012.

[103] K-K Ni, S Ospelkaus, M H G de Miranda, a Pe'er, B Neyenhuis, J J Zirbel, S Kotochigova, P S Julienne, D S Jin, and J Ye. A high phase-space-density gas of polar molecules. *Science*, 322(5899):231–235, 2008.

[104] Peter K. Molony, Philip D. Gregory, Zhonghua Ji, Bo Lu, Michael P. Köppinger, C. Ruth Le Sueur, Caroline L. Blackley, Jeremy M. Hutson, and Simon L. Cornish. Creation of Ultracold Rb87Cs133 Molecules in the Rovibrational Ground State. *Phys. Rev. Lett.*, 113(25):1–5, 2014.

[105] Tetsu Takekoshi, Lukas Reichsöllner, Andreas Schindewolf, Jeremy M. Hutson, C. Ruth Le Sueur, Olivier Dulieu, Francesca Ferlaino, Rudolf Grimm,

Hanns-Christoph Nägerl, C Ruth Le Sueur, Olivier Dulieu, Francesca Ferlaino, Rudolf Grimm, and Hanns-Christoph Nägerl. Ultracold Dense Samples of Dipolar RbCs Molecules in the Rovibrational and Hyperfine Ground State. *Phys. Rev. Lett.*, 113(20):205301, 2014.

[106] Fudong Wang, Dezhi Xiong, Xiaoke Li, Dajun Wang, and Eberhard Tiemann. Observation of Feshbach resonances between ultracold Na and Rb atoms. *Phys. Rev. A - At. Mol. Opt. Phys.*, 87(5):1–5, 2013.

[107] Fudong Wang, Xiaodong He, Xiaoke Li, Bing Zhu, Jun Chen, and Dajun Wang. Formation of ultracold NaRb Feshbach molecules. *New J. Phys.*, 17(3):035003, 2015.

[108] Ma Luo, Zhibing Li, and Chengguang Bao. Bose-Einstein condensate of a mixture of two species of spin-1 atoms. *Phys. Rev. A - At. Mol. Opt. Phys.*, 75(4):1–7, 2007.

[109] Z. F. Xu, Yunbo Zhang, and L. You. Binary mixture of spinor atomic Bose-Einstein condensates. *Phys. Rev. A - At. Mol. Opt. Phys.*, 79(2):1–5, 2009.

[110] Z. F. Xu, Jie Zhang, Yunbo Zhang, and L. You. Quantum states of a binary mixture of spinor Bose-Einstein condensates. *Phys. Rev. A - At. Mol. Opt. Phys.*, 81(3):1–5, 2010.

[111] Yu Shi. Ground states of a mixture of two species of spinor Bose gases with interspecies spin exchange. *Phys. Rev. A - At. Mol. Opt. Phys.*, 82(2), 2010.

[112] Jie Zhang, Xue Hou, Bin Chen, and Yunbo Zhang. Fragmentation of a spin-1 mixture in a magnetic field. *Phys. Rev. A*, 91(1):013628, 2015.

[113] Wenxian Zhang, D. L. Zhou, M. S. Chang, M. S. Chapman, and L. You. Dynamical instability and domain formation in a spin-1 Bose-Einstein condensate. *Phys. Rev. Lett.*, 95(18):1–4, 2005.

[114] L. Zhao, J. Jiang, T. Tang, M. Webb, and Y. Liu. Dynamics in spinor condensates tuned by a microwave dressing field. *Phys. Rev. A - At. Mol. Opt. Phys.*, 89(2):1–5, 2014.

[115] Rudolf Grimm, Matthias Weidemüller, and Yurii B. Ovchinnikov. Optical Dipole Traps for Neutral Atoms. *Adv. At. Mol. Opt. Phys.*, 42(C):95–170, 2000.

[116] L.-M. Duan. Controlling ultracold atoms in multi-band optical lattices for simulation of Kondo physics. *EPL (Europhysics Lett.*, 67(5):721, 2004.

[117] Michael Foss-Feig and Ana Maria Rey. Phase diagram of the bosonic Kondo-Hubbard model. *Phys. Rev. A - At. Mol. Opt. Phys.*, 84(5):1–10, 2011.

[118] a. V. Gorshkov, M. Hermele, V. Gurarie, C. Xu, P. S. Julienne, J. Ye, P. Zoller, E. Demler, M. D. Lukin, and a. M. Rey. Two-orbital SU(N) magnetism with ultracold alkaline-earth atoms. *Nat Phys*, 6(4):289–295, April 2010.

[119] H. Pu and P. Meystre. Creating macroscopic atomic Einstein-Podolsky-Rosen states from Bose-Einstein condensates. *Phys. Rev. Lett.*, 85(19):3987–3990, 2000.

[120] L. M. Duan, a. Sø rensen, J. I. Cirac, and P. Zoller. Squeezing and entanglement of atomic beams. *Phys. Rev. Lett.*, 85(19):3991–3994, 2000.

[121] Yu Shi and Qian Niu. Bose-Einstein condensation with an entangled order parameter. *Phys. Rev. Lett.*, 96(14):1–4, 2006.

[122] Zhi-Fang Xu, Xiaopeng Li, Peter Zoller, and W. Vincent Liu. Spontaneous Quantum Hall Effect in an Atomic Spinor Bose-Fermi Mixture. *Phys. Rev. Lett.*, 114(12):125303, 2015.

[123] J H Pixley, Xiaopeng Li, and S Das Sarma. Damping of Long-Wavelength Collective Modes in Spinor Bose-Fermi Mixtures. *Phys. Rev. Lett.*, 114(22):225303, 2015.

[124] Ming-Shien Chang, Qishu Qin, Wenxian Zhang, Li You, and Michael S Chapman. Coherent spinor dynamics in a spin-1 Bose condensate. *Nat Phys*, 1(2):111–116, November 2005.

[125] J. Kronjäger, C. Becker, P. Navez, K. Bongs, and K. Sengstock. Magnetically tuned spin dynamics resonance. *Phys. Rev. Lett.*, 97(11):1–4, 2006.

[126] a. Black, E. Gomez, L. Turner, S. Jung, and P. Lett. Spinor Dynamics in an Antiferromagnetic Spin-1 Condensate. *Phys. Rev. Lett.*, 99(7):1–4, 2007.

[127] C. Deutsch, F. Ramirez-Martinez, C. Lacroûte, F. Reinhard, T. Schneider, J. N. Fuchs, F. Piéchon, F. Laloë, J. Reichel, and P. Rosenbusch. Spin self-rephasing and very long coherence times in a trapped atomic ensemble. *Phys. Rev. Lett.*, 105(2):1–4, 2010.

[128] G. Kleine Büning, J. Will, W. Ertmer, E. Rasel, J. Arlt, C. Klempt, F. Ramirez-Martinez, F. Piéchon, and P. Rosenbusch. Extended coherence time on the clock transition of optically trapped rubidium. *Phys. Rev. Lett.*, 106(24):1–4, 2011.

[129] H. K. Pechkis, J. P. Wrubel, a. Schwettmann, P. F. Griffin, R. Barnett, E. Tiesinga, and P. D. Lett. Spinor dynamics in an antiferromagnetic spin-1 thermal bose gas. *Phys. Rev. Lett.*, 111(2):1–5, 2013.

[130] J S Krauser, U Ebling, N Fläschner, J Heinze, K Sengstock, M Lewenstein, a Eckardt, and C Becker. Giant spin oscillations in an ultracold Fermi sea. *Science*, 343(6167):157–60, 2014.

[131] Nille N. Klausen, John L. Bohn, and Chris H. Greene. Nature of spinor Bose-Einstein condensates in rubidium. *Phys. Rev. A*, 64(5):53602, 2001.

[132] E G M van Kempen, S J J M F Kokkelmans, D J Heinzen, and B J Verhaar. Interisotope determination of ultracold rubidium interactions from three high-precision experiments. *Phys. Rev. Lett.*, 88(9):093201, 2002.

[133] Masato Koashi and Masahito Ueda. Exact Eigenstates and Magnetic Response of Spin-1 and Spin-2 Bose-Einstein Condensates. *Phys. Rev. Lett.*, 84(6):1066–1069, 2000.

[134] C. V. Ciobanu, S.-K. Yip, and Tin-Lun Ho. Phase diagrams of F=2 spinor Bose-Einstein condensates. *Phys. Rev. A*, 61(3):5–9, 2000.

[135] Y. J. Lin, a. R. Perry, R. L. Compton, I. B. Spielman, and J. V. Porto. Rapid production of R 87 b Bose-Einstein condensates in a combined magnetic and optical potential. *Phys. Rev. A - At. Mol. Opt. Phys.*, 79(6):1–8, 2009.

[136] J. Kronjäger, C. Becker, M. Brinkmann, R. Walser, P. Navez, K. Bongs, and K. Sengstock. Evolution of a spinor condensate: Coherent dynamics, dephasing, and revivals. *Phys. Rev. A - At. Mol. Opt. Phys.*, 72(6):1–5, 2005.

[137] Artur Widera, Fabrice Gerbier, Simon Fölling, Tatjana Gericke, Olaf Mandel, and Immanuel Bloch. Precision measurement of spin-dependent interaction strengths for spin-1 and spin-2 87Rb atoms. *New J. Phys.*, 8, 2006.

[138] H Schmaljohann, M Erhard, J Kronjäger, M Kottke, S van Staa, L Cacciapuoti, J J Arlt, K Bongs, and K Sengstock. Dynamics of F=2 spinor Bose-Einstein condensates. *Phys. Rev. Lett.*, 92(4):040402, 2004.

[139] J. Kronjäger, C. Becker, P. Navez, K. Bongs, and K. Sengstock. Erratum: Magnetically Tuned Spin Dynamics Resonance [Phys. Rev. Lett. 97, 110404 (2006)]. *Phys. Rev. Lett.*, 100(18):189901, 2008.